Annu. Rev. Nucl. Part. Sci. 2000. 50:411–79

ON THE PRODUCTION OF SUPERHEAVY ELEMENTS

P. Armbruster
Gesellschaft fur Schwerionenforschung mbH, Nuclear Physics II Division, Planckstraße 1, D-64291 Darmstadt, Germany

Key Words ground-state stability of superheavy nuclei, recoil separators, decay chain analysis, hindrance in fusion entrance channel, deexcitation of fissile nuclei and collective enhancement of level densities, centrally depleted nuclei, hexadecupole deformation of heavy nuclei

■ **Abstract** In the first century of nuclear physics, 31 radioactive elements were added to the periodic system of elements. In 1996, at GSI, element 112 was synthesized by fusion of ^{70}Zn with ^{208}Pb, and its atomic number was established by a decay chain linked to known isotopes. Relativistic mean field calculations of the ground-state stability of nuclei predict the next spherical proton shell not as previously assumed at $Z = 114$ but at $Z = 120$ for $^{304}_{184}120$. Moreover, a region of spherical nuclei with depleted central density is predicted at $N = 172$ for $^{292}_{172}120$ by mean field calculations. New elements are established today using recoil separators combined with decay-chain analysis. Three new elements, $Z = 110$–112, and 18 transactinide isotopes have been discovered since 1985, all assigned by genetical linkage to known isotopes. The production cross sections decrease exponentially going to higher elements and now have reached the 1-pb limit. Fusion aiming at higher and higher atomic numbers is a self-terminated process because of constantly increasing disruptive Coulomb forces. The limitations in the formation and deexcitation stages are presented. The rapid drop to smaller cross sections ("Coulomb falls") is modified by nuclear structure not only in the ground state of the final product (superheavy element) but also in the collision partners and during the amalgamation process (closed shells and clusters). The prospects to produce higher elements and new isotopes by extrapolating the physics learned from reaching $Z = 112$ are ^{283}114, which might be found in ^{76}Ge/^{208}Pb at a level of 0.1 pb and linked to ^{259}No. At this level, about 30 transactinide isotopes are still in reach. To explain the stabilization of production cross sections in the pb range claimed in 1999 experiments, new physics delaying the descent in the "Coulomb falls" is to appear. For the FLNR experiments claiming $Z = 114$, no explanation is offered. For the LBL experiment claiming $Z = 118$, an explanation from new physics is presented. All experiments need confirmation. Verifying the centrally depleted, spherical nuclei around $^{292}_{172}120$ would be a victory for nuclear structure physics, much more interesting than the trivial case of another doubly closed shell nucleus.

0163-8998/00/1208-0411$14.00

CONTENTS

1. FROM THE DISCOVERY OF POLONIUM TO SUPERHEAVY ELEMENTS

The discovery of radioactivity in U minerals by Henri Becquerel in 1896 (1) started a new field of science: nuclear physics. Thirty-one radioactive elements, including U and Th, were added to the table of elements in the first century of the new science. All these elements decay by various disintegrations into elements with stable isotopes. Figure 1 presents the chemical elements climbing toward element Z = 112 (2), discovered just 100 years after Becquerel had announced his discovery to the French Academy of Science. This review on heavy elements cannot cover a century of research. It discusses the experiments since 1985, the date of my previous review in this journal (3). Figure 1 indicates the different periods we observe in retrospect. A first period (1896–1939) yielded the radioactive elements between Bi and U, all descended from the primordial elements U and Th. The atomic nucleus and the neutron were discovered in this period. A second period (1934–1955) produced the first manmade elements, culminating in the applications

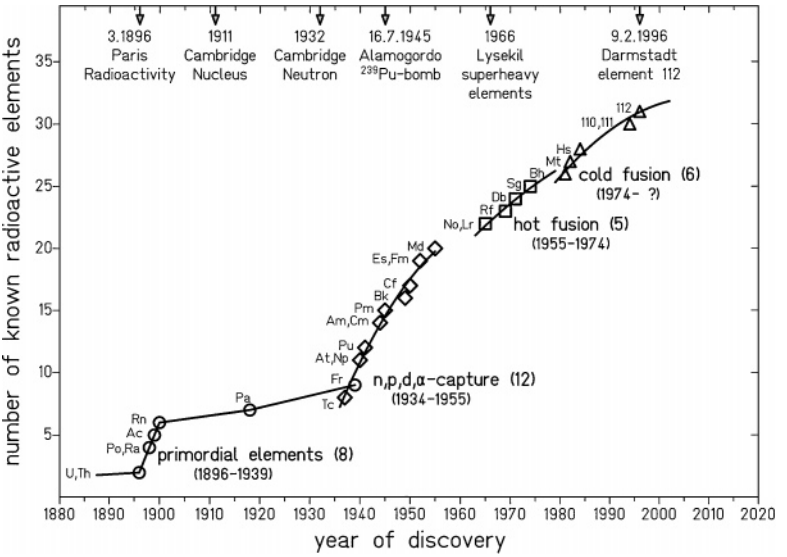

Figure 1 A century of radioactive elements. The number of known radioactive elements as function of time, starting in February 1896 with the discovery of radioactivity in U minerals (1) and ending in February 1996 with the synthesis of element 112 (2).

of fission in the 1940s. Neutron capture of the heaviest isotopes in the high neutron fluxes of nuclear reactors provided large quantities of the new elements. In the third period (1955–1974), the long-lived isotopes of the heaviest actinides produced in nuclear reactors were fused with isotopes of the light elements B to O accelerated in particle accelerators. Because the compound nuclei, after fusion, are heated owing to excitation energies between 40 and 50 MeV, this production method is called "hot fusion" or "actinide-based fusion." The last element so produced was seaborgium (Sg) in 1974. The method, which now uses still heavier projectiles of elements F to S, has given new isotopes and interesting results, which are covered in this review.

The center of interest of this article is the fourth period, which began in 1974 (4). Closed-shell nuclei, ^{208}Pb and ^{209}Bi, are fused with medium-weight neutron-rich isotopes such as ^{54}Cr to ^{70}Zn. At excitation energies of 10–20 MeV the compound systems stay colder than in hot fusion reactions. The method was called "cold fusion," or more appropriately "cluster-based fusion" or the neutral "Pb/Bi-based fusion." It was reviewed in my previous article for this journal (3). The fusion of closed-shell nuclei with neutron-rich partners produced the elements 107 to 112 (5–11). My principal message is that their synthesis is a nuclear structure–dominated process. The article closes with a discussion of the prospects of going beyond $Z = 112$ and of the fireworks of experiments in the last year of the century.

Based on the interplay of Coulomb energy, surface energy, and asymmetry energy in deformed liquid-drop-like nuclei a first theory of fission was presented by Bohr & Wheeler (12). The ratio of Coulomb forces to surface tension, the fissility x,

serves as a scaling parameter to describe fission barriers. With increasing proton number (Z), the Coulomb energy forces the fission barrier to decrease. For fixed Z, the fission barrier increases with the specific isospin $I = (N-Z)/(N+Z) = T_z/A$, passes a maximum, and finally, forced by the asymmetry energy at large values of I, decreases again. Spontaneous fission was predicted to become the dominant decay mode at higher Z-values, reaching half-lives of 10^{-6} s around $Z = 100$. Later, the observation of increased stability of nuclei at certain magic numbers of nucleons was explained by the shell model of the atomic nucleus and by the introduction of a spin-orbit term in the nuclear potential (13, 14). Swiatecki showed that the shell corrections to the binding energies of nuclei explain fission barriers and spontaneous-fission half-lives (15). Explaining the fission isomers (16), Myers & Swiatecki (17) needed deformation dependent shell corrections. Then Strutinsky (18) showed that shell gaps can be interpreted as regions of reduced level density of the excited states of the system. His prescription for calculating microscopic shell corrections was applied to correct the binding energies of the nuclear ground states obtained from a macroscopic model, such as the former liquid-drop model. These corrections can become large enough to stabilize the ground states of nuclei even in the case of vanishing macroscopic fission barriers. The concept of purely shell-stabilized nuclei was born, predicting further new elements, the so-called super-heavies.

The microscopic corrections to the binding energy of heavy nuclei are of the same order as the smoothly varying liquid-drop barriers which are taken as a scaling reference. Shell corrections and the liquid-drop barriers are underlying the chart of heavy nuclides shown in Figure 2 (see color insert). The double-shell closures at ^{208}Pb and at $^{304}_{184}120$ are the centers of regions of spherical nuclei, which are separated by a wide region of deformed nuclei. Subshells at $^{252}_{152}$Fm, $^{270}_{172}$Hs, and $^{292}_{172}120$ are indicated. The outer contour lines of Figure 2 represent estimated fission barriers of 4 MeV, and proton binding energies of -1.5 MeV, corresponding to half-lives of about 10^{-6} s, the detection limit of today's experiments. Numbers indicate different regions, defined by different ratios of shell corrections to liquid-drop barriers. In region 1, the liquid-drop barrier has fallen below the zero-point energy ($B_f = 0.5$ MeV). Shell corrections dominate and give high fission barriers that protect against spontaneous-fission decay. This is the region of superheavy elements (SHEs), where we find the deformed isotopes of the first SHEs, bohrium (Bh, $Z = 107$) to $Z = 112$. Going further down to the region 2, from Sg ($Z = 106$) to Fm ($Z = 100$) the shell correction energies become weaker, but the liquid-drop barriers start to increase. Here, spontaneous fission becomes a dominant decay mode at Rf ($Z = 104$). Region 3 shows shell correction energies and liquid-drop barriers of about equal height, starting with a ratio of 2 and ending with a ratio of 0.5 for these quantities. We find two subregions. First, at $N = 126$ there are strongly shell-stabilized spherical nuclei for elements above radium, which have small liquid drop fission barriers, are observed up until U (19) but are elusive beyond that. These nuclei are the best approximation to the spherical superheavy nuclei at $N = 184$, which are elusive as well. Second, between Es ($Z = 99$) and Pu ($Z = 94$) we find the well-studied region of deformed nuclei and fission

isomers (16) characterized by the interplay of shell correction energies and the increasing liquid-drop barriers. In this region the most complex nuclear structure is expected. Region 4 is dominated by liquid-drop barriers ($Z = 89-93$). Below the line of equal neutron binding energy and liquid-drop barriers ($Z < 88$), in region 5, fission is observed at high excitation energies only, and is not important for the ground state properties of nuclei.

2. THE GROUND-STATE SHELL CORRECTIONS FOR SUPERHEAVY NUCLEI

2.1 Experimental Masses, Shell Corrections, and Fission Barriers

Superheavy nuclei decaying by ground-state to ground-state α-decays yield directly the binding energy difference between the parent and daughter nuclei. The α-decay of e-e nuclei predominantly populates the ground state and the mass excess of the parent nucleus is obtained by summing the measured α-decay energy and the known mass excess of the daughter nucleus. Alpha-decay chains connect nuclei with the same isospin value $T_z = (N - Z)/2$, and a chain of e-e nuclei bridges a region of atomic numbers equal to twice the number of α-decay generations. The mass-excess values of the e-e nuclei in the chain $T_z = 24$ between $Z = 108$ and $Z = 102$ were measured in experiments at GSI using 1n and 2n reactions on ^{208}Pb targets (20, 21, 22).

The difference between the calculated mass excesses of a structureless macroscopic nuclear model (23) and measured values gives the shell correction energies. In the spirit of the early paper of Swiatecki (15), which introduced the concept of microscopic corrections to nuclear binding energies, the shell correction energies of the heaviest nuclei were determined for the known e-e isotopes of transuranic isotopes (24, 25). These are presented in Figure 3*a*.

Neglecting the microscopic correction of the binding energy at the saddle point, the fission barrier height is obtained by summing the fission barrier calculated from a macroscopic model and the experimental ground-state shell correction (Figure 3*b*). The negative shell corrections are strongest for $^{208}_{126}$Pb. They become weaker going to higher masses, and they reach values close to zero near $A = 225$. Increasing A further, approaching the next shell at $^{270}_{162}$Hs they are steadily reinforced again and reach values of $-(5$–$6)$ MeV (Figure 3*a*). The fission barriers between U and Hs are high and stay in the range of (5 ± 0.5) MeV (Figure 3*b*). The decrease of the macroscopic fission barriers, reaching values close to the zero-point vibrational energy of 0.5 MeV at Sg, is compensated by the steadily increasing microscopic shell corrections of the ground-state binding energies.

The fact that these nuclei decay by α-emission shows that the fission barriers are high enough to protect the nuclei against immediate spontaneous fission. It is the internal structure that makes the ground-state shell corrections large. Locally restricted in the deformation space around the ground-state a hole in the potential

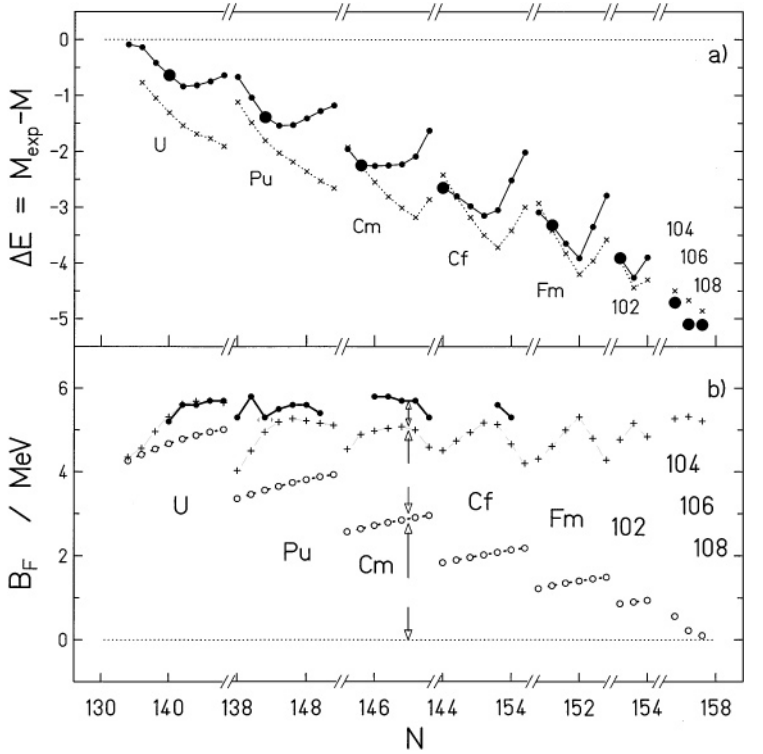

Figure 3 For the known e-e isotopes of elements U to Hs (25): (*a*) the shell-correction energies M_{exp}–M_{macro}/MeV; solid circles denote experimental data (• $T_z = 24$), x's denote calculations (28). (*b*) The fission barriers [B_{macro}–(M_{exp}–M_{macro})]; solid circles denote experimental data, pluses shell-corrected data, open circles macroscopic data (23).

energy surface appears, which is equivalent to raising a fission barrier stabilizing the nuclear system even in the case of macroscopic instability. The α-decay in the $T_z = 24$ chain proves that fission barriers for e-e nuclei are high enough, at least up to $Z = 108$, to guarantee decay times of spontaneous fission that are longer than the α-decay half-lives, which are on the order of 10^{-3} s. ^{264}Hs has all characteristics required to be "superheavy."

Moreover, the analysis of masses and half-lives in the chain $T_z = 24$ gave not only fission barriers but also estimates of the curvature of the barriers (3, 20). Beyond $Z = 102$, the barrier curvature increases by a factor of 2 compared with isotopes of lighter actinides. Here, a decrease of the fission barrier by 1 MeV changes the spontaneous-fission half-life by only 3–4 orders of magnitude, as compared to the 7 orders of magnitude found for the broad barriers of lighter elements. Figure 4 shows the calculated barriers for ^{240}Pu and ^{260}Sg (26, 27). The figure demonstrates that Sg has a single high barrier, whereas lighter actinides have broad double-humped barriers of about equal height. The barrier exit point

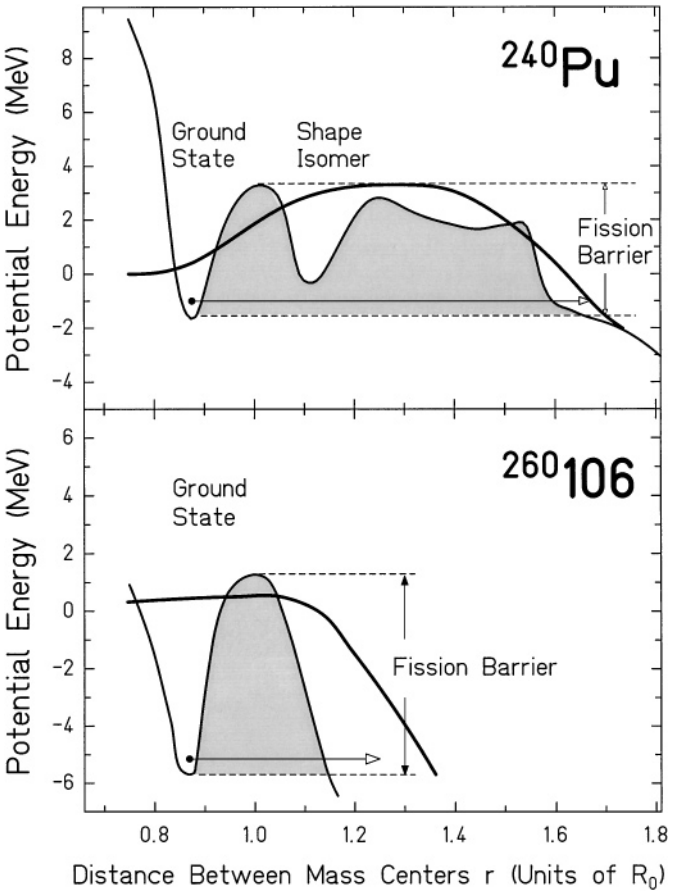

Figure 4 Comparison of the fission barriers of ^{240}Pu and ^{260}Sg. The narrow, single-humped barrier protects the nucleus ^{260}Sg (27) at small deformations that correspond to the first barrier of ^{240}Pu (26).

for ^{260}Sg at 1.15 times the g.s. radius corresponds to an elongation of about 3 fm compared to the diameter of the equivalent sphere of 15.5 fm. It is still a rather compact configuration close to the 2:1 axis ratio of superdeformation. The narrow fission barrier corroborates the analysis of spontaneous-fission half-lives, which indicated large barrier curvature values for the heaviest isotopes.

2.2 Recent Predictions of Shell Corrections and Half-Lives From the Macroscopic-Microscopic Approach

Macroscopic nuclear models combined with a microscopic approach, which takes into account the structure of the nuclear system, reproduce best the binding energies, decay modes, level schemes, and shell closures in the mass regions that

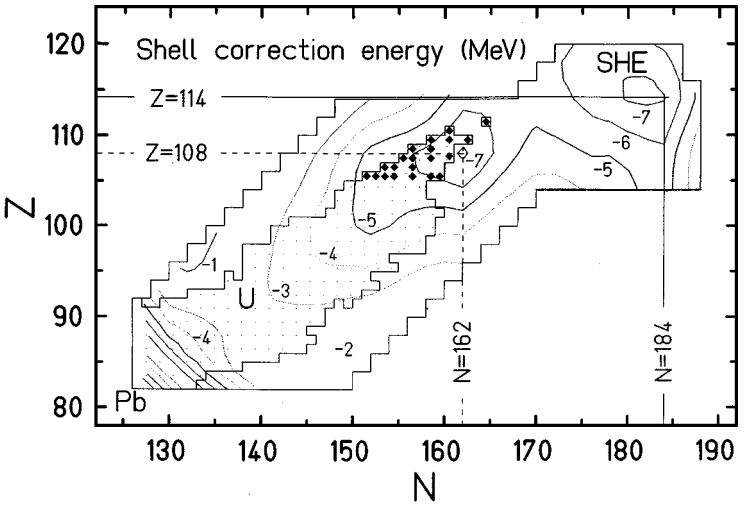

Figure 5 Shell-correction energies for elements between Pb and Z = 118 (29). The black symbols are known nuclei beyond Sg.

have been studied so far. The most reliable calculations stem from the University of Warsaw group (28) for e-e-nuclei of elements Z = 102–112. They reproduce the measured mass excesses and spontaneous-fission half-lives. Figure 5 shows the shell correction energies between Pb and element 120 (29). Extrema of shell corrections are predicted for the deformed nucleus $^{270}_{162}$Hs and the spherical nucleus $^{298}_{184}$114. The landscape between the smallest values near A = 228 and the next doubly closed deformed shell at Z = 108 and N = 162 describes well the trend of the experimental shell corrections, as shown before in Figure 3*a*. A smooth transition to larger negative shell corrections for nuclei approaching ^{270}Hs is predicted, followed by a flat local elevation of 1.5 MeV around ^{282}113 between the deformed and spherical minima.

Ever shorter half-lives end the periodic system of elements at proton number Z = 122 due to α-decay and at neutron number N = 190 due to spontaneous fission. Figure 6 (see color insert) presents the chart of nuclides covered by the calculation in Figure 5 and shows the different decay modes and half-lives as contour lines for odd-mass isotopes (28–30). We may expect about 380 isotopes with half-lives larger than 10^{-6} s between Bh and Z = 120. Following the calculations of the Warsaw group, the number of superheavy isotopes would equal the number of stable ones. The world of SHEs is no island. It is connected to the world of stable isotopes via the corridor of isospin values $T_z = 25 \pm 1.5$. Long chains of α-decays avoid spontaneously fissioning e-e isotopes and find a way from the superheavy elements Z = 107–120 to the lighter, long-lived actinides by passing the swamp of fission around Rf. The lighter actinides finally decay via the primordial α-chains to the stable isotopes of Pb and Bi.

2.3 New Results From Self-Consistent Mean Field Theories

Self-consistent mean field models were developed in parallel to the macrosopic-microscopic shell correction method (31–35). In the last years they reached an accuracy that made them competitive to the shell correction method. The latter is still the more accurate method to extrapolate the bulk properties of nuclei to a nearby neighborhood. This is because, as data accumulated from many experiments, the parameter sets of the macroscopic-microscopic models were improved continuously. The mutual support of shell corrections for neutrons and protons is evident from data on neutron- and proton-binding energies as well as on α-decay Q-values (36, 37). A mass formula that takes these findings into account still has high predictive power for nuclei up to the region of SHEs. It reproduces best the mass-excess data of the chain $T_z = 24$ (22) and meets within 0.7 MeV the mass-excess value of (119.6 $\pm$ 0.2) MeV at ^{264}Hs.

For extrapolations to regions far from nuclear stability, the different self-consistent mean field models are in principle the better approach. An effective nuclear two-body interaction introduced by Skyrme in 1959 (38) made Hartree-Fock calculations tractable. Models using Skyrme forces (SHF) are a first class of nonrelativistic self-consistent mean field theories, which are applied with varying parameters by different schools (39, 40), as discussed in a recent publication (41). Dechargé & Gogny introduced a two-body force of finite range (34), which required large numerical calculational efforts but gave very good agreement with nuclear data and level schemes. A second class of self-consistent mean field models are the relativistic mean field (RMF) models (35, 42). The finite-range interaction is built up from effective mesonic fields, and the spin-orbit interaction in nuclei emerges directly, as was shown back in 1956 (43). To explain the shell closures in nuclei, spin-orbit splitting was introduced into the early shell model, into the macroscopic-microscopic approach, and into other SHF models ad hoc. The RMF models predict shell closures far from the region of known nuclei in a unique and direct way. Spin-orbit splitting follows from the gradient of the effective mesonic interaction, which peaks at the nuclear surface. For a given proton shell, the different isotopes show different neutron densities, radii, and diffusenesses, which change the spin-orbit interaction. The mutual support of shell closures for neutrons and protons becomes an intrinsic feature of RMF models. For SHF models with effective spin-orbit interactions the mutual support is also guaranteed, but the isotopic and isotonic dependences were found to differ from RMF results. Because shell closures are a direct consequence of the mesonic fields, RMF models are best suited to answer the question of where the next spherical shell should be expected. For heavy nuclides with large values of isospin, the radial density dependences may adjust such that neutrons and protons might have different distributions, or that the nucleon density changes radially. Then the gradient of the potential changes, the spin-orbit interaction adjusts, and the shells are modified. Neutron-rich heavy nuclides far from the known isotopes may have shell closures that escape description by a macroscopic-microscopic model.

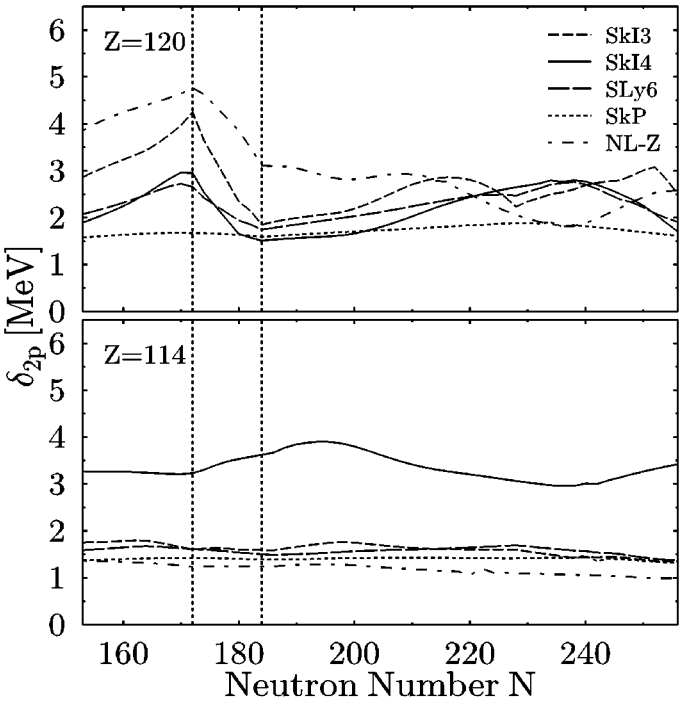

Figure 7 The two-proton gap in the chains of isotones calculated with the indicated forces (41) for Z = 114 and Z = 120.

Recent publications reporting results from self-consistent mean field models (39, 41, 42, 44) made predictions of the nuclear structure of superheavy isotopes and of shell closures beyond ^{208}Pb. Most of the predictions of the macroscopic-microscopic approaches were confirmed. Among them, the deformed shell at ^{270}Hs, a transition from deformed to spherical nuclei for N = 170 ± 2, and a spherical shell at N = 184 were found in all calculations. The spherical shell at Z = 114 was not confirmed. It moved to Z = 120, and at N = 172 a new subshell was found. A new spherical shell closure for $^{292}_{172}$120 is predicted (41, 44). This nucleus is a new nuclear species with a density that is depleted in the central region. $^{304}_{184}$120 replaces $^{298}_{184}$114 as the next doubly closed spherical nucleus beyond ^{208}Pb. Figure 7 demonstrates the shell strength for Z = 114 and Z = 120. For various self-consistent mean field models, the figure compares the two-proton shell gaps calculated from differences of two-proton binding energies (41).

The shell at Z = 114 disappears in the self-consistent model using the Gogny force (44), in RMF models, and in all but one of the SHF models. The disappearance of the shell at Z = 114 is related to the size of the spin-orbit splitting of the proton 2f orbitals. In former non–self-consistent models, the spin-orbit interaction was fitted to the $p_{3/2}/p_{1/2}$ splitting in ^{16}O. This condition is necessary but not

sufficient. The high spin-orbit doublets also must be reproduced by an interaction that is used to extrapolate beyond known nuclei. The fits reproducing the spin-orbit splitting in ^{16}O overestimated the splittings of the higher 2d and 2f orbitals in ^{208}Pb by 50% compared to the experimental values. By far the smallest deviations from the experimental splittings in ^{208}Pb are obtained by the RMF models. Here, the fit to ^{16}O also reproduces the higher orbits within 20%. Large spin-orbit splittings of the proton 3p and 2f orbits favor a shell closure at $Z = 114$, whereas a reduced splitting favors $Z = 120$, as calculated from RMF models. The good description of the spin-orbit splittings in ^{208}Pb provides a strong argument to switch the search to $Z = 120$, as recommended in Reference 41, and to abandon hope for a shell at $Z = 114$, on which experimentalists have been fixed since 1966. Predictions of the macroscopic-microscopic model, such as those shown in Figures 5 and 6, rely on a $Z = 114$ shell. Thus, beyond $Z = 112$ they may have to be revised.

A shell closure at $Z = 126$ is predicted by some of the SHF models with large spin-orbit splittings of the 3p and 2f orbits and a high-lying $i_{11/2}$ orbit (39), but none of the RMF models predicts such a shell. Moreover, the α-half-lives of isotopes of element 126 are predicted to be much shorter than the limits set by experimental techniques. The search for a SHE at $^{310}_{184}126$ is no task for today's experimental equipment.

The RMF models (41), the self-consistent mean field model using the Gogny force (44), and some of the SHF models predict a central depletion of the radial density distribution of up to 30%. This central depletion affects the low ℓ-orbits (3p and 2d), which are concentrated in the center of the nucleus, more than the higher ℓ-orbits (2f and 2g) concentrated at the surface. As the gradients of the density distribution at the outer surface and the inner surface change sign, so does the spin-orbit interaction proportional to the gradient. The spin-orbit interaction of the 3p and 2d orbits defined by the radial interaction integral is strongly decreased, whereas the integral is changed only a little for the 2f and 2g orbits. The central depletion is largest when the action of the $N = 172$ and the $Z = 120$ shells support each other, and the shell gap becomes largest for $^{292}_{172}120$. The RMF models predict not only a decrease of the spin-orbit splitting but even a change of the level ordering. $d_{5/2}$ neutrons and $p_{3/2}$ protons should have lower binding energies than their low-spin counterparts. The mesonic fields, an essential ingredient of the RMF model, and the finite-range character of the effective potential explain the shift of the shell closure to $Z = 120$, as well as the central depletion. The finite-range Gogny force (44) combined with a spin-orbit interaction added ad hoc, treated in a self-consistent calculation, also predicts the central depletion for exactly the same nucleus $^{292}_{172}120$. This cross check of two theories gives additional weight to the prediction.

Between the two spherical nuclei ^{208}Pb and $^{304}120$ with doubly closed shells, two new shell-stabilized entities, ^{270}Hs and $^{292}120$, are located. Neither the experimentally confirmed deformed shell, stabilized by large hexadecupole moments, nor the predicted spherical shell stabilized by a central depletion find a counterpart in other regions of the chart of nuclides. These shell closures are unexpected

nuclear structure phenomena, the explanation of which demands an understanding far beyond the evident prediction of a next spherical closed shell at N = 184, which follows by direct extrapolation from the very first shell model with spin-orbit interaction.

3. RECOIL SEPARATION AND DECAY CHAIN ANALYSIS

3.1 General Requirements

To fuse two nuclei at the Coulomb barrier and thereby produce the heaviest elements, specific bombarding energies between 4.5 MeV/u and 5.5 MeV/u must be available. These correspond to energies of 80–350 MeV for projectiles in the mass range A = 16–80. Experimental equipment has to be specifically designed in order to detect isotopes heavier than A = 250 of elements of atomic numbers larger than Z = 104, whose decay modes are mainly α-decay and fission. Electron capture (EC) branches are expected to be small and rare. Half-lives will be shorter than a few hours. A lower limit on decay times is given by the shortest separation times possible with today's experimental equipment.

All elements are assumed to be made by fusion of heavy nuclei, that is, by a reaction with excitation functions with a window not wider than 10 MeV FWHM (10^{18} atoms/cm^2). Accelerators must deliver beams with an energy definition better than 2 MeV. Production cross sections are below 10 nb, the largest production cross sections found for isotopes of Rf. The cross section limit should be pushed to as small a value as possible. The beam intensities should be as high as target technology allows. A thin target of 10^{18} atoms/cm^2 ($\sim$0.4 mg/cm^2) at intensities $6 \cdot 10^{12}$/s (1p μA) is heated by about 10 W. The rotating targets are cooled either by radiation cooling or by gas-flow cooling at low pressures (45). Beam intensities on-target of one particle μA are upper limits reached in the best cases with modern ECR sources and rotating Pb and Bi targets heated nearly to their melting points (46). Luminosities of 10^{31}/cm^2 s equivalent to about 1/pb·d may be within reach of future target technology.

To detect primary isotopes of the heaviest elements, the separation time must be as short as possible. To detect the longer-lived members of an α-decay chain, the separation time can be adjusted to the half-lives (which may be days long). Chemistry and cluster-loaded gas-jet transport systems have separation times of the order of seconds and are applied as long as isotopes in this time range are observed. The few-microsecond range of half-lives is accessible by recoil separation, which has transit times of this order.

For a given separation method the efficiency ε_0 to transport a separated isotope to a detector system and to identify the species is another important quantity. Recoil separators equipped with implantation detectors reach total efficiencies $\varepsilon_0 = 0.4$. Moreover, the selectivity of a separation method against primary beam particles, target recoil atoms, and transfer products is important. Gas-jet transport systems

do not differentiate between radioactive transfer products at all. Chemistry has a high selectivity against unwanted elements. Recoil separators reduce transfer products up to three or four orders of magnitude. Further reductions are possible by detector systems behind the separator.

Table 1 lists the main specifications and values of luminosities, total efficiencies, and selectivities for recoil separator systems dedicated to present heavy element research.

3.2 Recoil Separators

Today, laboratories active in heavy-element synthesis either use fast-chemistry methods (47–49) or recoil separators combined with implantation techniques (2, 50–53). For the discovery of the new elements, chemical methods no longer played the role they once had. The chemistry of the heaviest elements is a field of its own and certainly deserves a review of its own (54). In the present review neither chemistry methods nor the chemistry of the heaviest elements will be covered adequately. The recoil separators in their two appearances, as combinations of deflections in magnetic and electric fields and as gas-filled magnetic separators, are discussed in the following. Two GSI-Darmstadt separators have pioneered high-efficiency separation: The velocity filter SHIP (separator for heavy ion reaction products) succeeded with Pb/Bi-based reactions in 1979 (50), the gas-filled magnetic separator HECK (helium charge exchange kaleidoscope) with actinide-based reactions in 1990 (55).

Velocity Separators The conservation of mass and momentum in a fusion reaction demands that the fused product of mass $A = A_1 + A_2$ be emitted in the beam direction with a well-defined velocity v, given by $v = A_1 v_1/(A_1 + A_2)$. A_1 and A_2 are the masses of the projectile and the target; v_1 is the velocity of the projectile hitting the target nucleus at rest. Particles of velocity v emitted in the beam direction must be fusion products. A velocity filter selecting these particles is a kinematic mass separator. Since the projectiles and fusion products are both flying in the beam direction with different velocities, the separation problem is characterized by the suppression factor of primary projectiles in the velocity window of the fusion products. The ratio of projectiles to reaction products at the entrance to the filter is larger than 10^8. Suppression factors of at least this magnitude must be demanded. Already acceptances of 2–3 msr guarantee a transport through the velocity filter of up to 40% for evaporation residues (EVRs) produced at small excitation energy in Pb/Bi-based reactions.

Three filters are presently used to search for heavy elements. SHIP, a velocity filter at GSI-Darmstadt, has been operating since 1976 at the UNILAC (56–58). VASSILISSA, an E/q filter at FLNR-Dubna, has been active in heavy element research since 1989 (51). The Fragment Mass Analyser (FMS), installed at ANL in 1992 (59), is a high-resolution A/q separator, which pays for high resolution with a reduced efficiency.

TABLE 1 Recoil separators in heavy element research active in 1999

Separator	**SHIP 94 (GSI) (2, 80)**	**Vassilissa (FLNR) (51)**	**FMS (ANL) (59)**	**GFS (FLNR) (52)**	**GARIS (RIKEN) (70)**	**RITU Jyväskylä (71)**	**BGS (LBL) (53)**
Start	1976	1990	1992	1992	1987	1994	1999
Configuration	Q_2EDEQ_2D	$Q_3E_3Q_3D$	Q_2EDEQ_2	DQ_hQ_v	DQ_hQ_v	$Q_vDQ_hQ_v$	Q_vD_hD
Solid angle (msr)	4	15	8	9	22	10	45
Bending angle (deg.)	—	—	—	22	45	25	70
Length (m)	11	19	8.2	4.3	4.8	4.7	~4
Luminosity (pb^{-1} d^{-1})	0.1	0.1	—	0.15	—	—	0.18
Transmission	0.45(1n)	0.3(3n)	—	0.4(3n)	—	0.25	0.75(1n)
Suppression of target recoils	5.10^3	2.10^4	—	5.10^4	—	—	$>5.10^4$
Detector pixels	700	600	—	240	—	700	700
Q^{pulse}-factor for randoms (relative)	1	2	—	1.2	—	—	>0.3

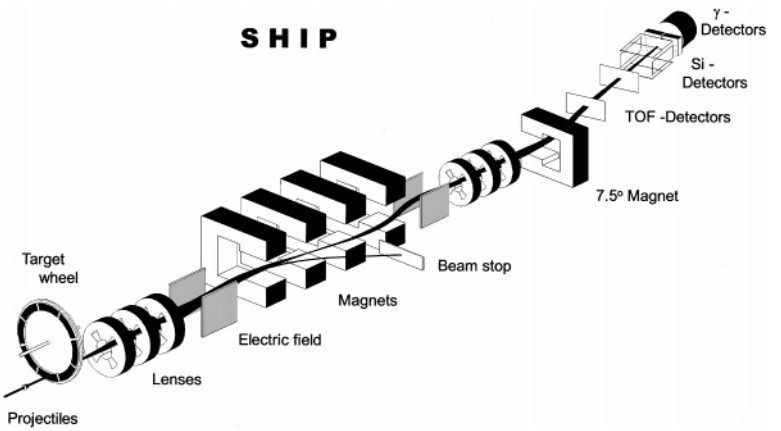

Figure 8 SHIP94 (Separator for Heavy Ion reaction Products), a two-stage velocity filter to separate fusion products, shown with its detector system (2).

Figure 8 shows the velocity separator SHIP94. The combination of two electric and four magnetic dipole fields, along with two quadrupole triplets, focuses all ionic charges within an ionic charge window of 20%. The velocity dispersion necessary to separate projectiles and EVRs is maximal in the medium plane of the system. Here, the beams are separated. The velocity dispersion is then compensated in the second half of the filter, which is ion-optically antisymmetric to the first half. Suppression of the primary beam depends on the velocity difference between projectiles and EVRs. Ar, Kr, and Xe beams producing $A = 180$ EVRs have been suppressed by factors of 10^{12}, 10^{10}, and 10^{8}, respectively. The number of scattered background particles is further reduced by a 7°-deflection magnet behind the main velocity filter. Detector systems are installed directly at the focus position behind the 7° magnet, which introduces a dispersion of 20 cm. A time-of-flight (TOF) system behind SHIP allows a redundant velocity measurement (60). Implantation into surface barrier detectors allows an energy measurement of the EVRs at their original velocity. Along with the TOF measurement, a rough value of the mass can be obtained ($A/\Delta A \approx 10$). These detector systems act as additional stages of beam purification with possible background suppression factors up to 10^3. In sub-barrier fusion studies, cross sections were followed over six orders of magnitude and fusion cross sections in the microbarn region could still be measured without exploiting the radioactive decay properties of the EVRs (61). SHIP separates the reaction products spatially, and nuclei produced with submicrobarn cross sections are detected by their radioactive decay properties. Thus, it is not only a tool for reaction studies but also a powerful on-line isotope separator. The subsequent α-decays and spontaneous-fission decays of the implanted nuclei are correlated with each other and to the signals obtained at the time of implantation into the surface barrier detector (62). Half-lives are determined from even just a few events

by the maximum likelihood method. As the recoil energy from α-decay is small, an implanted nucleus does not change position. Position-sensitive detectors thus allow another large reduction of accidental correlations (63). The detection system used at SHIP consists of 7 identical 16-strip Si wafers (2). These wafers are position-sensitive in the vertical direction with a FWHM resolution of 0.15 mm between subsequent α-decays in a chain. The position resolution between an implanted EVR and an α-particle in the chain is 0.5 mm FWHM. The active area of the implantation detector is $35 \cdot 80$ mm^2 and each of its 16 strips is 5 mm wide. The EVRs are dispersed on about half of the strips. Six 16-strip wafers operating at 263 K are mounted in the backward hemisphere facing the stop detector. They measure the escaping α-particles and fission products with a solid angle of 80% of 2π. An energy resolution of 15 keV FWHM was measured for α-particles in the chain. For α-particles the energy was obtained by summing the energy loss signals from the implantation detector and one of the backward detectors. In this case, the resolution was not better than 40 keV FWHM, depending on the position hit in the backward detector. With a 90% probability, all signals from a single decay chain are found within 0.8 mm, giving about 700 detector pixels for the implantation detector. This value, given in Table 1, is much smaller than the value 3700 following from the FWHM value of 0.15 mm measured for α-α correlations alone. To estimate random correlation rates, the numbers of detector pixels given in the table should be used.

Gas-Filled Magnetic Separators Since my previous review in this journal in 1985 (3), gas-filled magnetic separators have become a serious alternative to velocity filters. They cost less, their technology is simple, and they are faster and more efficient than velocity filters. Whether their selectivity is adequate remains to be shown in the coming years. Gas-filled magnetic separators were applied early to separate fission products (64, 65) and to produce the first secondary radioactive beams (66) used for studies in atomic physics in the 1 MeV/u range. The technique is also used in accelerator-based mass spectroscopy (67). It was applied first to fusion EVRs at Dubna (68). SASSY-LBL, the first instrument of this type working in the field of heavy element research, demonstrated that the separation of ^{254}No in the reaction ^{48}Ca on ^{208}Pb (3.2 μb) was possible (69). Also for actinide-based reactions a high separation efficiency was obtained, as was demonstrated by the production of ^{254}No in the reaction ^{20}Ne on ^{238}U ($<$20 nb) using HECK (55). Most of the instruments used helium as filling gas. In the early 1990s, a H_2-filled magnetic separator was installed at FLNR (52). At RIKEN (70), at Jyväskylä (71), and at LBL (53), He-filled systems were built and are presently in use.

The deflection in a magnetic field depends on the average charge of an ion $\overline{q}$ during its passage through the magnetic field, with $B\rho/\mathrm{Tm} = 0.027(v/v_0)A/\overline{q}$ and $v_o = \alpha c$, the Bohr velocity. The ratio $v/\overline{q}$ depends only weakly on the velocity, and $B\rho/A$ becomes a function depending mainly on the atomic number. A large velocity window and the full ionic charge distribution can be accepted, which accounts for the high efficiency of the method. The deflection in a gas-filled

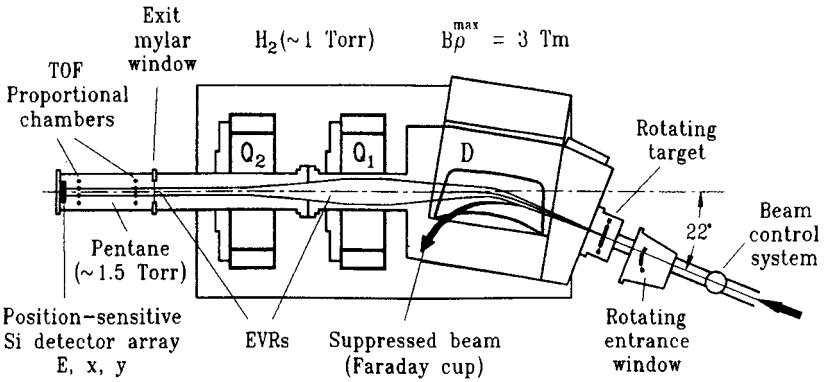

Figure 9 The FLNR H_2-filled separator (DQ_h,Q_v) with its detector system (52, 95).

magnetic field, where the gas provides the averaging over all possible ionic charges, depends on the mass and atomic number. The resolution is governed by two properties of the ion: the dispersion between neighboring atomic numbers and the fluctuations of the average ionic charges. A gas-filled separator has to be calibrated either with well-defined beams of heavy ions or with reaction products that are known and can be identified by their radioactivity. For two velocity ranges, $v/v_0 = 2.2$ and $v/v_0 = 4$, the $B\rho/A$ values for different ions in He have been determined (68, 69). They follow a $Z^{1/3}$ dependence, superimposed with an oscillating function determined by the electronic shell structure of the ions. These oscillations are most pronounced at low velocity. They govern the resolving power. In regions of atomic numbers for which $B\rho/A$ decreases with Z ($Z < 90$), the difference in $B\rho$ for neighboring elements is reduced and separation is difficult, whereas for increasing $B\rho/A$ ($Z > 90$), the dispersion between elements is larger, and moderate mass resolution can be achieved. The specifications of the four gas-filled separators active today in heavy element research are given in Table 1. The separator prototypes installed at FLNR (52) and at LBL (53) are shown in Figures 9 and 10.

3.3 Actinide-Based Reactions and Selectivity

The unresolved question of the gas-filled separator technique is the selectivity it can achieve. Excellent suppression of full energy projectiles was found for mass asymmetric collision systems. For projectile masses $A < 48$ the primary beam is suppressed sufficiently to detect EVRs in the picobarn range (52, 55). Whether the suppression of target recoils and transfer products is adequate for actinide-based reactions remains an open question, as transfer products may be α-active or fission spontaneously. Since the production cross sections for transfer products in the mb to μb range are high and the mass resolution of the separation technique is poor, it is not surprising that gas-filled magnetic separators, despite their high

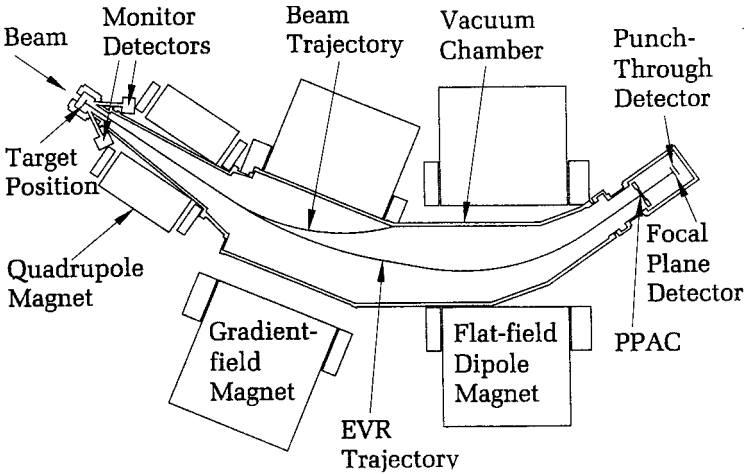

Figure 10 The LBL gas-filled separator BGS (Q_v,D_h,D) with its detector systems (53).

separation efficiencies, still have problems with actinide targets where production cross sections of EVRs are in the pb range (72, 73). A background specific to gas-filled separators is elastic recoils produced in collisions of projectiles and gas atoms of the filling, which are forward-emitted with about twice the projectile velocity and registered in the implantation detector. The penetrating α-particles (80 MeV) and protons (20 MeV) must be discriminated out by a second Si detector behind the implantation detector. This veto detector is needed in support of the TOF detectors, which are not triggered reliably by the fast, light particles. Neither the study of transfer reactions on actinides at the Coulomb barrier nor the investigations of the atomic physics involved in the ion-gas interaction has kept up with the speed of the installation of new systems. Both should complement the studies on production of heavy elements.

Early experiments with ^{48}Ca/^{248}Cm aiming at element 116 (74) made important findings concerning actinide-based reactions at recoil separators (75, 76). Transfer reactions at the Coulomb barrier produce with a total cross section $>$30 mb, in addition to the $>$50 long-lived isotopes near the target nucleus, about 45 short-lived α-emitters in the mass range A = 210–230. Of this cross section, 13 mb goes into α-particles from isotopes stemming about equally from the elements 83 to 92 and having half-lives less than a typical irradiation time of one month. For ^{48}Ca on ^{244}Pu and ^{238}U, the cross section was not measured but is assumed to be similar. In the regime of disappearance of complete fusion and the onset of quasi-fission, experiments on binary reactions (77, 78) confirmed the large cross sections toward mass symmetry for multinucleon transfer reactions at the fusion barrier. For ^{48}Ca-induced reactions on ^{238}U at the barrier, quasi-fission rather than complete fusion becomes the dominant reaction channel, whereas for ^{40}Ca-induced reactions, complete fusion can still be a remnant reaction channel. These

reaction studies demonstrated that the additional neutrons of ^{48}Ca do *not* reduce the hindrance of fusion in the entrance channel. Radiochemical studies comparing transfer reactions of ^{40}Ca, ^{44}Ca, and ^{48}Ca on ^{248}Cm corroborated the dramatic change in reaction mechanism in the mass range A = (40–48), away from complete fusion and toward quasi-fission (75, 79).

The successful discrimination of random correlations involving α-particles emitted by transfer products was demonstrated for the ^{48}Ca-on-^{248}Cm experiment at SHIP. The experimenters segmented the detector into position-sensitive pixels, counted α-particles and fission products during two thirds of the total measuring time in the pauses between beam pulses, and used a detector system that identified fusion events after they were separated once more by their kinematics. Because accidentals obey a rate equation, the limits of the correlation method could be studied even at the lower luminosity, and the findings are also valid for the more sensitive experiments done today. Figure 11 summarizes the results of the 10-day ^{48}Ca/^{248}Cm experiment (76). It shows a mass–versus–α-energy correlation plot. The mass values determined by the systems of detectors behind the separator stage were correlated to following α-particles, with the α-energies registered in the implantation detector. Short correlation times of 7 ms were chosen for particles registered when the beam was on. For particles detected in the pauses between

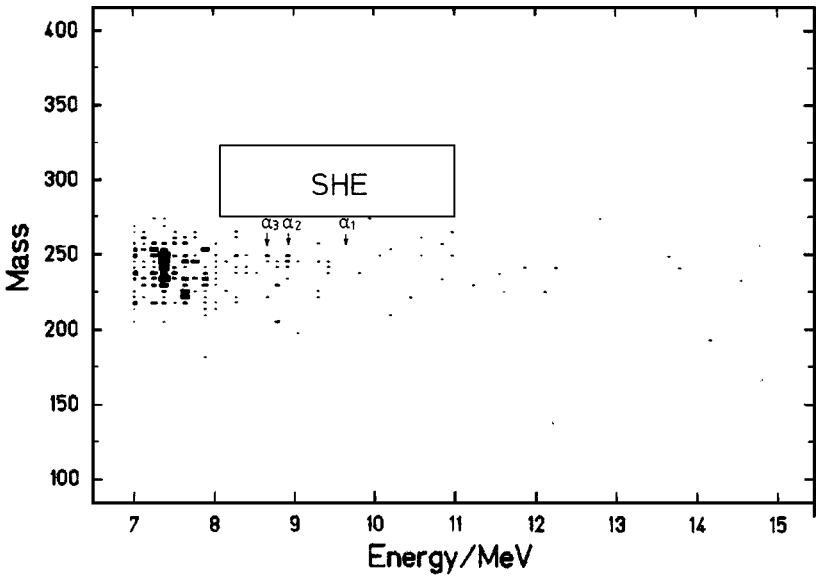

Figure 11 Correlation plot for time and position correlated implanted ions and α-decays from the ^{48}Ca/^{248}Cm reaction (74, 76). Position window $\pm$0.8 mm, time windows from 13 μs to 40 ms for decays during UNILAC beam-bursts, and to 312 s for decays in the beam pause. Arrows indicate the three α-energies observed experimentally (73), and a label indicates the region where superheavy elements were expected.

pulses (14 ms), the maximum correlation time was set to 310 s. The mass resolution is low, but sufficient to purify the α-spectra in the energy range where EVRs of SHEs could be expected. Figure 11 shows that a suppression of background activity in the energy range in which the α-spectrum of SHEs is mixed with transfer products (73) can reach a value of $>10^2$. Superheavy isotopes will have α-energies and half-lives, decay genetics, and spontaneous-fission properties that differ from transfer products and their daughters. On these nuclear physics markers any final assignment must be built. But Figure 11 demonstrates that besides the separator, a system of detectors can help to separate EVRs, target recoils, and transfer products. Such discrimination is obligatory for gas-filled magnetic separators, which have inherently poor resolutions in mass and velocity. For actinide-based reactions with their high cross sections for the production of α-particles and spontaneously fissioning isotopes, all measures of discrimination must be applied. For the Pb/Bi-based reactions, mass separation by a detector system was part of all experiments that discovered SHEs at SHIP (2, 80). Another strictly observed rule was that correlation time analysis in the high background of the irradiation pulse was restricted to times below the 0.1-s range and long correlation times of known daughter isotopes were measured in the low background between the beam pulses. The decay event that gave the first evidence for meitnerium (Mt) in 1982 showed all decay signals between beam pulses. It was this fact which gave confidence that one atom could prove the discovery of a new element (7).

3.4 The "One Atom/One New Element" Method

Single atoms of a new element separated by a recoil separator and implanted in a position-sensitive Si detector can be identified from an analysis of the decay event relating the new isotope to a known isotope. The decays in a sequence of generations are time-correlated to each other. As for all correlation techniques, the method is finally restricted by a maximum possible correlation time, beyond which accidental correlations dominate, and no further correlation analysis of signals is allowed. In the following, the basic limitation of the "one atom/one new element" method due to random correlations is discussed (81). Here, the basic equations are given to define a "figure of merit" for suppression of accidentals, to calculate the maximum possible correlation time t_{max} for an experiment, and to estimate probabilities of finding true events by the correlation method. In the limit of one event, three conditions must be fulfilled in order to identify a new element from the observation of a single nucleus and its decay chain.

The luminosity, L, of the experimental set-up separating the wanted species with an efficiency ε_0 should allow synthesis of at least one event in a chosen measuring time T and at an assumed cross section σ_0. This defines the first condition:

$$n = L \cdot \varepsilon_0 \cdot \sigma_0 T \geq 1. \qquad 1.$$

As limiting case in single-event analysis, we assume that the probabilities of the event to be true or accidental should be equal, and the probability that a particular

registered event is accidental should be <50%. This is the second condition.

$$n_{true} \geq 0.5 \geq n_b. \qquad 2a.$$

As long as all background is produced by the beam in the target, the number of events n registered by the detector and the corresponding rates R in the detector are proportional to each other: $n_i = T \cdot N_d \cdot R_i$, where T is the measuring time and N_d the number of subdivisions (pixels) of the total detector area. We divide Equation 2 by $N_d T$ and obtain an equation between rates.

$$R_{true} \geq (2TN_d)^{-1} \geq R_b \qquad 2b.$$

The rate of random events R_b of a sequence of K subsequent signals in fixed order simulating a decay chain of (K–1) generations is given by the product of the rates in the K classes of signals and the (K–1) correlation times Δt between the decay events (82). This rate equation is the third condition.

$$R_{bi} = \prod_{i=1}^{K} R_i \cdot \prod_{i=1}^{K-1} \Delta t_{i,i+1} \qquad 3.$$

Equation 3 holds for events that start with an implanted nucleus of the first generation, followed by a fixed-order sequence of (K–1) generations of subsequent signals. Because random sequences are time-reversible, in the case of chains that end with a rare and unambiguous spontaneous-fission signal, counting in reversed order of time is possible and equivalent. Equation 3 is a rate equation, which does not depend on the measuring time T. Only smaller rates and smaller correlation times in the (K–1) generations reduce the random rate. Underlying R_b are the cross sections σ_i and decay times τ_i of the beam-induced processes that make up the rates R_i, along with the efficiencies ε_i of the experimental facility to suppress the different species, indexed i.

The number of random events (Equation 4) follows from applying $n_b = R_b \cdot N_d \cdot T$ to Equation 3. For single-decay-chain analysis, the number of random events n_b reduces to the probability P_{err} that the "true" event is not true. nb = 1 means the event is accidental. Down at $n_b \leq 0.1$, one can seriously start to speculate on an eventual new nonrandom phenomenon indicated by the correlation with a >90% probability to be true.

$$P_{err} = n_K \prod_{i=1}^{K-1} R_i \cdot \Delta t_{i,i+1}, \qquad 4.$$

for fixed order in single chains. Like Equation 3, Equation 4 does not depend on the time direction chosen for the analysis. Whether seen from the recoil or from the spontaneous-fission signal ending a chain, n_{bi} is the same.

Besides determining the number of random events, the above equations determine the maximum possible correlation time t_{max} of a given experiment. Combining Equations 2*b* and 3 gives a maximum value of t_{max} that satisfies the limiting

case of Equation 2*b*. This largest possible correlation time to find the event to be true (with a 50% probability) is given by the rates (R_i) in the (K–1) generations and the number (n_j) of starters of sequences. But the condition that one chain is detected and that the decision on this chain, whether true or accidental, can be made on the basis of a 50% probability is unrealistic. The times t_{max} derived with this assumption are too large. True events should be true within a 1σ probability. The 1σ margin of safety reduces t_{max} by a factor of 10.5, the 2σ margin by a factor of 30.2.

$$t_{max}^{1\sigma} = \frac{1}{10.5} \cdot \frac{1}{\left(2n_K \prod_{i=1}^{K-1} R_i\right)^{(K-1)^{-1}}}. \qquad 5.$$

Separating the parameters concerning the experimental devices and the reaction cross sections, a "figure of merit" Q for suppressing accidentals characteristic for each instrument is defined:

$$Q = \frac{N_d}{L \cdot \varepsilon \cdot d\Omega} = \frac{S/d\Omega}{L/N_d}. \qquad 6.$$

Q is the ratio of the suppression of target-like recoils and transfer products emitted into a unit of solid angle over the luminosity per pixel-detector. Measuring with pauses between the irradiation pulses increases the Q-values by factors of 10–30, given by the ratio of target recoils to α-emitting transfer products. Note that Q cannot be improved by longer measuring times.

The minimum accessible cross section σ_0 and the figure of merit Q to suppress accidentals are the decisive quantities to be compared for the different separating facilities and experiments. To optimize an experiment means to maximize the product $Q \cdot L$ for the given experimental conditions, a procedure well known to all coincidence experiments. Luminosities and correlation times cannot both be increased simultaneously unless essential improvements have been made to reduce background rates. Table 1 shows that the facilities that are applied to heavy element research have comparable values of Q and L (within a factor of 2). The main difference is whether they operate in continuous or discontinuous mode, that is, a choice between L and Q. Which option to choose depends on the experiment to be performed.

4. NEW ISOTOPES AND NEW ELEMENTS

The discoveries of the 15 years since my previous review (3) are discussed in this section. Starting with Rf and ending with the highest element reached, new isotopes are presented first for actinide-based reactions and then for Pb/Bi-based reactions. Finally, the discovery of the new elements $Z = 110$–112 is discussed.

4.1 Six New Isotopes From Actinide-Based Reactions: ^{262}Rf, ^{263}Db, ^{265,266}Sg, ^{267}Bh, ^{267}Hs

The last undisputed discovery of an element using an actinide-based reaction dates back to 1974. In the reaction ^{249}Cf(^{18}O,4n), the isotope ^{263}Sg was synthesized and identified (83). A He-jet transport system coupled to a rotating wheel moved the produced activity including the unknown isotope in front of a detector system, which identified the species by a correlation to the known daughter product ^{259}Rf. The experiment, which reached its limit with a cross section of 0.3 nb and a half-life of 0.9 s, could not suppress the copious transfer products. To continue studies on still heavier fusion products without any knowledge of the dominant reaction channels for transfer products was considered prohibitively difficult. The LBL group decided to exploit multinucleon transfer reactions for production of new isotopes. The cross sections in the range of 0.1 μb to 1 mb are large. The heaviest targets of actinides, ^{238}U, ^{248}Cm, ^{249}Cf, and ^{254}Es, were irradiated by heavy ions from O to U with energies close to the Coulomb barrier. The long-lived activities were investigated using the whole arsenal of nuclear chemistry methods. Many new actinide isotopes for elements up to Lr were discovered, but these interesting results are not the subject of this article. The 10 years of research are documented in comprehensive papers (84, 85). Early attempts to irradiate ^{249}Cf and ^{249}Bk targets with ^{20,22}Ne beams, with the intent to produce isotopes of the next higher elements Z = 107, 108, failed at LBL and FLNR (86, 87). The large background of transfer products could not be suppressed sufficiently. It became evident that only methods with very high discrimination powers had a chance to proceed toward higher elements using actinide-based reactions. An increased suppression of transfer products by at least a factor of 10^3 would be necessary to synthesize elements with production cross sections in the sub-nb range. As half-lives were expected to be short, the high selectivity of chemistry methods could not help. All groups decided not to give up actinide-based research, but to adapt to the new needs the techniques that had been successfully applied by the GSI-Darmstadt group. The instruments were discussed in the Section 3. Their results follow below.

But first, the discovery of the new isotope ^{263}Db in the reaction ^{249}Bk(^{18}O,4n) by an LBL-GSI collaboration should be reported (88). Automated fast chemistry was used in continuation of the LBL-GSI tradition of nuclear chemistry, and the (27^{+10}_{-7})s α-emitter ^{263}Db with a spontaneous-fission branch of 57% was identified. The genetic link to the daughter nucleus ^{259}Lr was established, whereas an EC branch to ^{263}Rf could not be found. In the fall of 1999, the Paul Scherrer Institute (PSI) in collaboration with GSI and LBL announced that they had synthesized another new isotope, ^{267}Bh, in the reaction ^{249}Bk(^{22}Ne,4n), with an α-half-life of about 17 s (89, 90). Again, fast chemistry methods succeeded not only in producing the isotope with about 60 pb, but also in attacking the chemistry of element 107, as was done before for Sg (91).

The gas-filled separator HECK at GSI was operated in the years 1989–1991 (55). The most asymmetric reactions ever investigated with gas-filled separators,

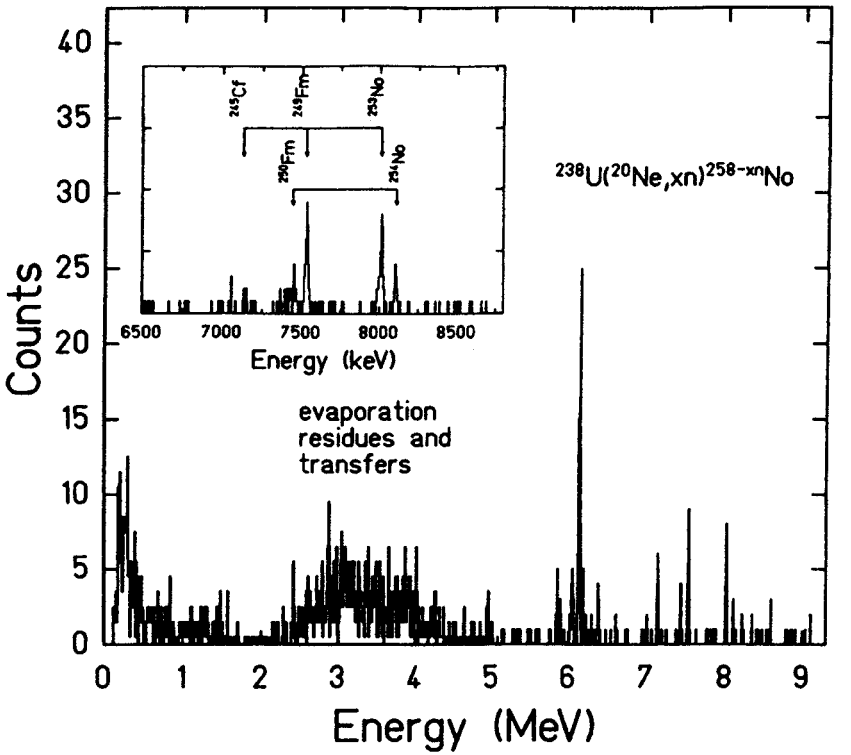

Figure 12 Energy spectrum from ^{238}U(^{20}Ne,xn)$^{258-x}$No measured with the gas-filled separator (HECK) (55). *Inset*: the spectrum outside the beam pulses.

^{16}O and ^{20}Ne on ^{238}U, were explored to prove the high efficiency of the method. Values of ε_0 of 10 to 20% were obtained for mass asymmetries $(A_T - A_P)/(A_T + A_P)$ between 0.83 and 0.87. The spectrum obtained in the ^{20}Ne experiment is shown in Figure 12. The isotopes ^{254,253}No are clearly identified in the pause spectrum along with their daughters and a granddaughter, ^{245}Cf. In 1990, a dose of $1.3 \cdot 10^{17}$ ions was sufficient to identify unambiguously the element No, which had been claimed 30 years earlier but had remained controversial ever since. For the light projectiles on ^{238}U, the suppression of transfer products was high and the 5n-cross section of (13 ± 6) nb in the reaction of ^{20}Ne/^{238}U could be measured without difficulties.

The separator VASSILISSA started in 1990 using the targets ^{232}Th and ^{236}U irradiated by beams of ^{22}Ne, ^{26}Mg, ^{27}Al, and ^{31}P (92, 93). The known isotopes $^{252–254}$No, ^{254}Lr, and ^{258}Db were synthesized as fusion EVRs from xn-channels with x = 4–6. All isotopes are α-emitters and chains of correlated events could be used for isotope identification. The 5n-channel product ^{253}No was produced in three reactions, ^{20}Ne/^{238}U (55), ^{22}Ne/^{236}U, and ^{26}Mg/^{232}Th (92), with the cross

sections of (13 ± 6) nb, (25 ± 4) nb, and (9 ± 4) nb, respectively. These cross sections are much smaller than the 100 nb reported in 1966 for ^{22}Ne/^{238}U (94). A new measurement of the 5n cross sections in ^{22}Ne/^{238}U is urgently needed, as reduced fusion probabilities in the entrance channel of actinide-based reactions start to set in. Comparing ^{26}Mg/^{232}Th and ^{22}Ne/^{236}U, which both lead to the same compound nucleus, showed that the more asymmetric collision system had a larger production cross section for all xn-channels observed. The same was found for the pair of reactions ^{27}Al/^{236}U and ^{31}P/^{232}Th when the 5n-channel leading to ^{258}Db was observed. The cross section for the more asymmetric system using ^{27}Al beams was 0.45 ± 0.2 nb; for ^{31}P/^{232}Th, a cross section of 0.12 nb was reported (93). These early VASSILISSA experiments are an important contribution to the understanding of reactions using actinide targets in the domain where hindrance in the entrance channel is observed. A continuation of this kind of experiment could yield excitation functions at least for the elements Z = 102–106. So far, this prerequisite for heavy element synthesis by actinide-based reactions has been badly neglected.

To have opened the sub-nb range of production cross sections for actinide-based reactions is the merit of the FLNR gas-filled separator that has been operating since 1992 (52). The experiments that used the targets ^{238}U, ^{244}Pu, and ^{248}Cm with beams of ^{22}Ne, ^{26}Mg, and ^{34}S were aimed at elements beyond Rf in the range of production cross sections down to 1 pb. They were performed by a Dubna-Livermore collaboration and are tied to the name of the late Yuri Lazarev (95).

In 1993, the heavy isotopes ^{265}Sg and ^{266}Sg were synthesized by the reaction ^{22}Ne/^{248}Cm as 4n- and 5n-channel products (96). Both isotopes are α-emitters and were correlated to their Rf and No daughters. Because the implanted EVRs could not be detected in this experiment, their half-lives could not be measured but were estimated from α-energies. The experiment was confirmed recently in a series of experiments at GSI and LBL, which finally aimed at the chemistry of Sg (91, 97, 98) and became possible only because of the longer half-lives of the new isotopes. ^{265}Sg is an α-emitter with a half-life of 7.4 s and α-energies between 8.69 MeV and 8.94 MeV. ^{266}Sg has a half-life of 21 s and emits α-particles of 8.58–8.72 MeV. A fission half-life of 11 s is estimated as a lower limit (98). The half-life of the daughter of ^{266}Sg, the isotope ^{262}Rf, was measured by α–spontaneous-fission correlation. Its value, 2.0 ± 0.5 s, is much larger than the 47 ms given in the earlier LBL experiments (99). An increased half-life for spontaneous fission of isotopes of Sg, concluded first by Demin et al (100) and then found in the 1n reactions ^{207,208}Pb/^{54}Cr (21, 22), is now established for ^{266}Sg also. The increase of spontaneous-fission half-lives for an increase of four atomic numbers is a factor of $5 \cdot 10^3$ for the N = 158 pair ^{262}Rf(2 s)/^{258}Fm (0.38 ms) and a factor of $2 \cdot 10^3$ for the N = 160 pair ^{266}Sg(11 s)/^{262}No (5 ms). Only four nucleons separate ^{266}Sg from ^{270}Hs, the center of the deformed shell at Z = 108/N = 162. Its increased stability toward spontaneous fission follows the prediction of the Warsaw group (28).

In a further experiment of ^{22}Ne/^{244}Pu, the correlation between the daughter ^{261}Rf and the granddaughter ^{257}No of ^{265}Sg was investigated carefully. The overlapping

α-energies and half-lives of the two isotopes were determined by analyzing their α-α correlation (95). No α-branch could be detected for ^{262}Rf, the 4n-channel product, i.e. the chain $T_z = 27$ cannot be connected to the known mass-excess values of its lower members, and there is no access to the mass excess of ^{266}Sg by α-transitions between e-e isotopes. The reaction ^{26}Mg/^{238}U, producing ^{259,260}Rf in analogy to ^{22}Ne/^{244}Pu, was investigated as well (95). The cross section of the 5n-channel isotope ^{259}Rf was determined by the correlation to ^{255}No. The fission branch of ^{259}Rf was not confirmed. This spontaneous-fission branch, so important in the discussion of the discovery of Rf, converges to smaller and smaller values over time. A missing experiment is ^{20}Ne/^{248}Cm. Discovering ^{264}Sg and an α-bridge at ^{260}Rf would be highly rewarding. The e-e isotopes of the chain $T_z = 26$ are also accessible by ^{207}Pb(^{70}Zn,n)^{276}112 and their α-energies would link the region of SHEs over the bridge at ^{260}Rf to the mass of ^{256}No.

In 1994, the reaction ^{34}S on ^{238}U was investigated (101), and via the 5n-channel the isotope ^{267}Hs was discovered. FLNR succeeded in detecting a new isotope by a full EVR-α-α-α chain analysis. Three chains were presented, starting with EVR implantation followed by the decays of the new isotope ^{267}Hs and two more α-particles each, which agree with the known properties of ^{259}Rf and ^{255}No. ^{267}Hs decays with α-energies between 9.75 and 9.88 MeV, and a half-life of (19^{+29}_{-10}) ms was reported. The 5n-production cross section is about 2.5 pb. ^{267}Hs is the daughter of ^{271}110, which was synthesized by ^{208}Pb(^{64}Ni,n) with 15 pb. It was observed in seven chains of ^{271}110 (102). The α-energies of ^{267}Hs were confirmed and the half-life was modified to 59 ms. The FLNR experiment showed that an effective fissility of 0.80 was reached in an actinide-based reaction.

Parallel to the search for element 110 at GSI, in 1994, the reaction ^{34}S/^{244}Pu was investigated at FLNR (72). The aim was to produce isotope ^{273}110 in a 5n-channel. This experiment is discussed in Section 4.3 along with the decay chains of ^{277}112, which populate ^{273}110 as a daughter. The last section of this review comments on the announcement in 1999 of the discovery of three isotopes of the new element $Z = 114$ and new isotopes of elements 112, 110, and Hs in ^{48}Ca-induced reactions (73, 103–104a).

The actinide-based reactions and their cross sections are compiled in Table 2. Figure 13 gives the cross section of the largest channel as a function of the atomic number for elements beyond No. The cross sections strongly decrease as the atomic numbers increases. This was observed as well for Pb/Bi-based reactions (see Section 4.3) and symmetric collision systems (see Section 5.2). The lines connect cross sections obtained with the different neutron-rich targets, such as ^{232}Th, ^{238}U, ^{244}Pu, ^{248}Cm, and ^{249}Bk/^{249}Cf. The highest cross sections for synthesizing a specific element are obtained for the most asymmetric reactions possible, that is, for the most neutron-rich isotope of the heaviest element that can be used as a target. This line was followed at LBL since Seaborg decided to build the High-Flux Isotope Reactor at Oak Ridge in the late 1960s in order to produce these targets. The lighter elements Th, U, and Pu cannot compete with Cm, Bk, and Cf, as was demonstrated convincingly again by the recent experiments at FLNR (92, 93). The question whether neutron-rich projectiles help to increase the cross section for

TABLE 2 Actinide-based reactions Z = 104–108 (1985–1999)

Atomic number	Reaction	Isotope	Decay mode	Half-life	Dose (10^{18})	α/nb	Method	Reference
	^{248}Cm(^{18}O,4n)	^{262}Rf	sf	53 ms		5 ± 1	wheel, sf	99
	^{244}Pu(^{22}Ne,4n)	^{262}Rf	sf	50 ms		1 ± 1	wheel, sf	99
	^{248}Cm(^{22}Ne,4n)	^{262}Rf	sf new	1.9 s		—	gasfilled sep. α-chain,	96
							chemistry α-chain	162
							gas-jet, α-chain	98
104	^{248}Cm(^{18}O,5n)	^{261}Rf	α			5	gas-jet, α-chain	163
	^{244}Pu(^{22}Ne,5n)	^{261}Rf	α			$3.5^{+7}_{-2.3}$	gasfilled sep., α-chain	95
	^{244}Pu(^{22}Ne,5n)	^{261}Rf	α			$1.5^{+2.6}_{-0.8}$	chemistry, α-chain	98
	^{249}Bk(^{15}N,4n)	^{260}Rf	sf			14 ± 2	wheel, sf	99
	^{248}Cm(^{16}O,4n)	^{260}Rf	sf			6 ± 1	wheel, sf	99
	^{238}U(^{26}Mg,5n)	^{259}Rf	α		2	1.1	gasfilled sep., α-chain	95
	^{246}Cm(^{16}O,4n)	^{258}Rf	sf			10^{+10}_{-3}	wheel, sf	99
105	^{249}Bk(^{18}O,4n)	^{263}Db	α, sf (50%) new	27 s		10 ± 6	chemistry α-chain, sf	88
	^{249}Bk(^{18}O,5n)	^{262}Db	α, sf			6 ± 3	chemistry α-chain, sf	88
	^{248}Cm(^{19}F,5n)	^{262}Db	α, sf			2	chemistry α-chain	164
	^{248}Cm(^{19}F,5n)	^{262}Db	α, sf			$0.26^{+0.15}_{-0.09}$	gas-jet, α-chain	165
	^{236}U(^{27}Al,5n)	^{258}Db	α, EC		2.7	0.45 ± 0.2	Vassilissa α-chain	93
	^{232}Th(^{31}P,5n)	^{258}Db	α, EC			0.12 ± 0.1	Vassilissa α-chain	92
106	^{248}Cm(^{22}Ne,4n)	^{266}Sg	α, sf new		10	(60 ± 20) 10^{-3}	gasfilled sep., α-chain	96
	^{248}Cm(^{22}Ne,4n)	^{266}Sg		21 s		(25 ± 12) 10^{-3}	chemistry α-chain	98
	^{248}Cm(^{22}Ne,4n)	^{266}Sg				(54^{+26}_{-29}) 10^{-3}	gas-jet, α-chain	166
	^{248}Cm(^{22}Ne,5n)	^{265}Sg	α new		60	$0.26^{+0.08}_{-0.0.2}$	gas-filled sep., α-chain	96
	^{248}Cm(^{22}Ne,5n)	^{265}Sg	α	7.4 s		0.24 ± 0.12	chemistry α-chain	98
107	^{249}Bk(^{22}Ne,4n)	^{267}Bh	α new	17 s		0.06	chemistry α-chain	89, 90
108	^{238}U(^{34}S,5n)	^{267}Hs	α new	90 ms	17	(2.5^{+5}_{-2}) 10^{-3}	gas-filled sep., α-chain	101

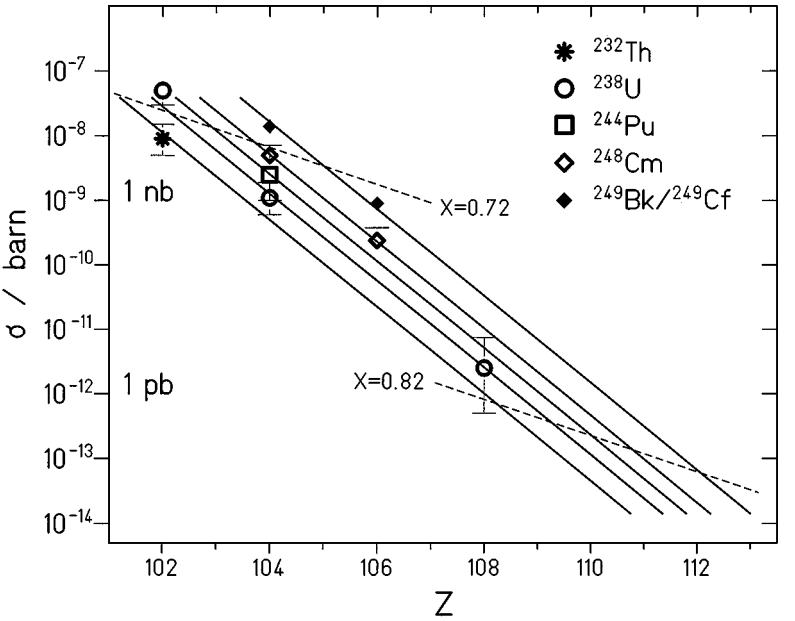

Figure 13 Cross sections for actinide-based reactions using the most neutron-rich targets, ^{232}Th, ^{238}U, ^{244}Pu, ^{248}Cm, and ^{249}Bk/^{209}Cf, for elements Z = 102–108. The lines indicate σ-values for a given target. For each of the reaction systems the channel with the highest cross section is presented. The effective fissilities x = 0.72 and x = 0.82 are indicated as hatched lines.

systems that are hindered in the entrance channel is still open. The 4n-cross sections of the nuclei $^{16}_{8}$O (closed shell) and ^{18}O on ^{248}Cm producing Rf isotopes are equal (99). A comparison of ^{20}Ne and ^{22}Ne on ^{248}Cm is still missing, as is any comparative study using projectiles beyond Ne. In continuation of the ^{232}Th and ^{238}U experiments at FLNR, projectiles such as ^{32}S, ^{34}S, and ^{36}S could be used to measure the production cross sections of the isotopes $^{261–266}$Sg and $^{265–270}$Hs. These experiments would help to disentangle the importance of the isospin of the projectile and its nuclear structure, relative to the fission barrier of the compound system. All these parameters vary in the proposed reactions: The isospin of the projectiles changes from 0 to 2, their neutron numbers change from 16 to the closed shell 20, and the neutron number of the compound nuclei changes from 155 to 166 passing the shell N = 162.

4.2 Seven New Isotopes From Pb/Bi-Based Reactions: ^{253,254}Rf, ^{256}Db, ^{258}Sg, ^{264}Bh, ^{269}Hs, ^{268}Mt

Seven new isotopes of the transactinide elements Rf to Mt were discovered since my previous review (3), using Pb/Bi-based reactions in the range of cross sections

between 2.4 nb and 1 pb. These reactions are compiled in Table 3. All experiments were done at GSI using SHIP94 and its detector system (Figure 8).

The isotope ^{253}Rf was produced by the reaction ^{204}Pb (^{50}Ti,n) (105) with a cross section of 0.19 nb. In the comparable reaction with ^{208}Pb as reaction partner, a cross section of 10 nb was observed. An increase of a factor of 2.7 is observed going from ^{204}Pb to ^{208}Pb for each additional neutron in the target. ^{253}Rf decays by spontaneous fission with a half-life of 48 μs. Compared to ^{255}Rf, the spontaneous-fission half-life decreased by the large factor of $7 \cdot 10^4$, indicating a drop of the fission barrier of about 1.4 MeV between N = 151 and N = 149. Such a rapid decrease was observed earlier between ^{252}No and ^{250}No when the neutron number changed from N = 150 to N = 148.

The isotope ^{256}Db produced by ^{209}Bi(^{50}Ti,3n) was shown to be an α-emitter with a strong EC branch to ^{256}Rf (106) and a half-life of 1.9 s. No direct spontaneous-fission branch is confirmed for the o-o isotope. Alpha energies are in the range of 9.02–9.2 MeV. The new isotope ^{252}Lr was identified by the correlation to its mother, ^{256}Db. It has a half-life of 0.36 s and α-energies of 8.97–9.02 MeV.

The e-e isotope ^{254}Rf was synthesized in the 2n-channel of the reaction ^{50}Ti on ^{206}Pb with a cross section of 2.4 $\pm$ 0.2 nb (105). The gain in cross section replacing ^{206}Pb by ^{208}Pb is a factor of 2.2 for each neutron added. ^{254}Rf decays by spontaneous fission with a half-life of (23 $\pm$ 3) μs, in good agreement with a predicted value of 60 μs published by the Warsaw group (28). The spontaneous-fission half-lives of e-e isotopes show a large decrease going at constant neutron numbers from No to Rf. This change is explained by the disappearance of the outer fission barrier for the Rf isotopes. For the N = 150 pair ^{252}No/^{254}Rf, the half-life changes by the large factor of $4 \cdot 10^5$, as was observed earlier at N = 152 and N = 154. The decrease of the half-life by a factor of 270 compared to ^{256}Rf shows again that fission barriers decrease for N < 152. The next e-e isotope, ^{252}Rf, will already be below the detection limit of recoil spectrometers. It will decay in the target area with a half-life shorter than 1 μs.

Another spontaneous-fission emitter, the e-e isotope ^{258}Sg, was discovered in the reaction ^{209}Bi(^{51}V,2n) with a production cross section of 38 $\pm$ 13 pb (105). This type of reaction was used before to search for ^{267}110 in the 1n-channel of the reaction ^{49}Co/^{209}Bi at LBL (108). Extrapolating from ^{51}V projectiles to ^{59}Co projectiles gives a cross section for the production of ^{267}110, which is smaller than 0.3 pb. ^{258}Sg has a half-life of $(2.9^{+1.3}_{-0.7})$ ms, in good agreement with the calculation giving 1.8 ms (28). This half-life is only a factor of 2 smaller than that of the preceding e-e isotone ^{256}Rf. For the neighboring e-e istotones ^{258}Rf and ^{260}Sg, a similar factor had been observed (21). The small decrease of spontaneous-fission half-lives going from Rf to Sg for the N = 152 and N = 154 isotones is a first indication of increasing stability toward spontaneous fission for elements beyond Z = 104. The deformed shell at Z = 108 manifests its presence.

The scarce information from the 1986 experiment on the e-e isotope ^{264}Hs (22) was complemented in 1994 by three more events (9). ^{264}Hs is an α-emitter of 10.43 MeV and has a spontaneous-fission branch of 0.5. With a half-life of

0.45 s, an spontaneous-fission half-life of about 1 ms follows, which is significantly smaller than the calculated value of 21 ms (28). The mass excess of ^{264}Hs is 119.6 MeV (107).

The new isotopes ^{264}Bh and ^{268}Mt were discovered in the three decay chains of ^{272}111 (10), which were produced in ^{209}Bi(^{64}Ni,n). They are both α-emitters with half-lives of $(0.44\,^{0.6}_{0.16})$ s and (70^{+100}_{-30}) ms, and α-energies of (9.48;9.62) MeV and (10.10;10.24) MeV, respectively. From ^{262}Bh and ^{266}Mt to the more neutron-rich isotopes ^{264}Bh and ^{268}Mt, the α-half-lives increase by a factor of about 50, in agreement with the known trend. The isotope ^{269}Hs was discovered in the decay chains, which led to the discovery of element 112 (11, 2). It is discussed along with the discovery of element 112 in the next section.

4.3 The Discovery of Elements Z = 110 to Z = 112

The synthesis of elements Z = 110–112 became possible because of the improved velocity filter SHIP94 and its new detector system (2). The upgrade was done in 1989–1993. A luminosity of 0.1 $pb^{-1} \cdot d^{-1}$ was reached for Ni and Zn projectiles irradiating Pb/Bi targets of 0.45 mg/cm^2. The detector system allowed reconstruction of full α-energies from two signals, one in the implantation detector and another one in any of the backward detectors. The probability of losing part of the α-energy was reduced to 10%. Working with irradiation pulses of half the length of the pause intervals guaranteed a small background in two thirds of the measuring time for all half-lives larger than 7 ms. The 1n-reaction products show a very narrow angular distribution, which is accepted fully by the 4-msr opening angle of of the spectrometer. The transmission ε_0 through the spectrometer is 0.4. The segmentation of the implantation detector with a number of non-overlapping pixel-detectors of 700 is a factor of 6 larger than in the experiments before 1988. The luminosity increase by a factor of 2.6, along with larger measuring times, gave access to production cross sections in the pb range.

Excitation Functions The choice of the optimal bombarding energy is crucial for the production of the heaviest nuclei. It is determined empirically by extrapolating optimal energies from measured excitation functions of preceding lighter elements. The 1n excitation functions using irradiations of ^{208}Pb and ^{209}Bi targets by ^{50}Ti, ^{58}Fe, and ^{64}Ni projectiles are presented in Figure 14. Excitation energies for the nuclei in the center of the target were calculated using experimental mass excesses published by Audi & Wapstra (109) or values predicted by Myers & Swiatecki (110). The optimal energies of the 1n-channels, which have the highest production cross sections, show a shift to smaller values going from Rf to Z = 111. E^{x}_{max} for ^{50}Ti/^{208}Pb is observed at 15.6 $\pm$ 0.1 MeV, whereas for ^{64}Ni/^{208}Pb, a value of 12.4 $\pm$ 0.5 MeV is found. The widths of the distributions show surprisingly small values of 4 $\pm$ 1 MeV FWHM, including the contributions from energy straggling in the 0.45 mg/cm^2 thick targets. Thus, the real width of the 1n-excitation function is much smaller than the measured FWHM values of 7 MeV

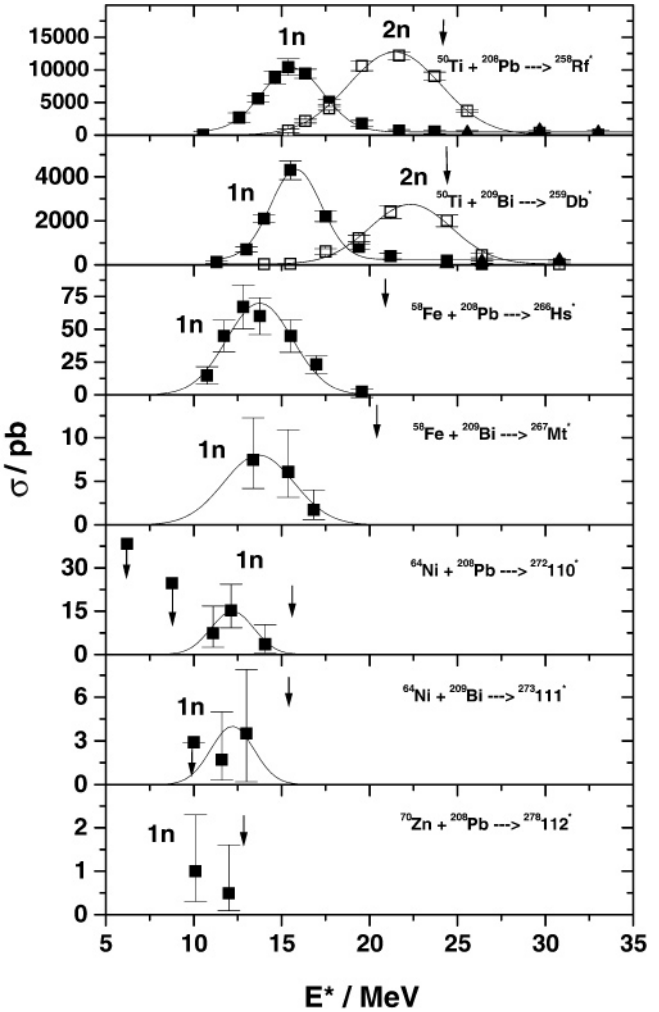

Figure 14 The 1n excitation functions for production of pairs of elements 104/105 (9, 106), 108/109 (9, 114), and 110/111 (10, 102) for Pb/Bi-based reactions. The Bass barriers (111) are indicated by arrows. The solid lines are Gaussian fits to the data.

for the 2n-reaction. For the four heaviest elements, Z = 109–112, only the 1n-channel is established, whereas for lighter elements the 2n-channel up to Hs and the 3n-channel up to Db were also observed. Most important, all 1n-excitation functions peak at energies below the fusion barrier (111). No events were ever observed below $E^x = 10$ MeV. The window where events were seen is 12 MeV wide for Rf and decreases to 5 MeV for Z = 110. For Z = 112, a window between 10 and 13 MeV can be extrapolated. The best excitation energy to produce elements

$Z = 112$ and $Z = 113$ should be between 11 and 12 MeV. For a given projectile bombarding ^{208}Pb and ^{209}Bi, the E^* dependences of the excitation functions are, within experimental accuracy, equal. As observed in the range of projectiles ^{50}Ti to ^{64}Ni, increasing the atomic number of the projectile by two units decreases the optimal energy by about 1 MeV. $E^x = 11.5$ MeV is extrapolated for ^{70}Zn projectiles, leading to $Z = 112$ and $Z = 113$, which is in good agreement with the above estimate using the width of the energy window for 1n-events. Having measured the excitation function of $Z = 112$, one could extrapolate to the next higher projectile ^{76}Ge, a prerequisite to proceeding to $Z = 114$.

Complementing the compilations in Reference 3, Table 3 gives the irradiation conditions for experiments on Pb/Bi-based reactions performed since 1985. The table displays the excitation energies chosen and the total doses applied. A total dose of $6.5 \cdot 10^{18}$ Ni ions on target over a period of 42 days in November–December 1994, corresponding to an average current of $2 \cdot 10^{12}$ ions/s, was used to synthesize ^{269}110, ^{271}110, and ^{272}111. A dose of 3.4 10^{18} ions of ^{70}Zn on target was collected during a period of 41 days in February 1996, corresponding to 10^{12} ions/s, in order to synthesize ^{277}112. The experiment was repeated during a period of 26 days in May 2000, collecting a dose of 4.7 10^{18} ions corresponding to $2 \cdot 10^{12}$ ions/s. The excitation energies covered in the two experiments were in the window of 9–13 MeV (2).

Discovery of Element 110 The isotope ^{269}110, produced in the reaction ^{62}Ni on ^{208}Pb, was identified by the daughter isotopes ^{265}Hs, ^{261}Sg, ^{257}Rf, and ^{253}No, all of which were known before (9). The new isotope is an α-emitter of $E_\alpha = 11.11 \pm 0.02$ MeV and has a half-life of (170^{+160}_{-60}) μs. The production cross section is $3.5^{+2.7}_{-1.8}$ pb. Figure 15 shows two of the four observed decay chains. Both chains are complete. The figure provides full information on the implanted nucleus, its energy and position, along with the α-energies, correlation times, and positions of five generations of α-decay. Whether the signals were observed in the pulse or the pause is indicated. Moreover, α-energies reconstructed from signals in two detectors or observed as full energy signals are indicated. The α-energies and correlation times in the five-generation decay agree well with the decay data of the four known isotopes. There is no doubt an isotope of element 110 was synthesized. At LBL, in the reaction ^{59}Co on ^{209}Bi, a single sequence of signals was found, which was assigned to ^{267}110 (108). The sequence is incomplete, ^{263}Hs is missing, and the known isotopes that one would expect, ^{259}Sg, ^{255}Rf, and ^{251}No, were not seen in the sequence. In judging the priority of discovery of element 110, the reader should compare the LBL sequence to the chains in Figure 15.

The isotope ^{271}110 was produced in the reaction ^{64}Ni on ^{208}Pb (2, 102). It could be identified by the known daughter isotopes ^{267}Hs, ^{263}Sg, ^{259}Rf, and ^{255}No. Nine chains were observed; three of them were complete and showed five generations of α-decay. Five chains showed only four generations of α-decay, as ^{255}No has a strong EC branch to the long-lived ^{255}Md (27 min). None of the chains was broken by spontaneous fission in ^{263}Sg or ^{259}Rf, thus reducing the spontaneous-fission branch of these isotopes to $\approx$10%. Figure 15 shows a complete chain of ^{271}110.

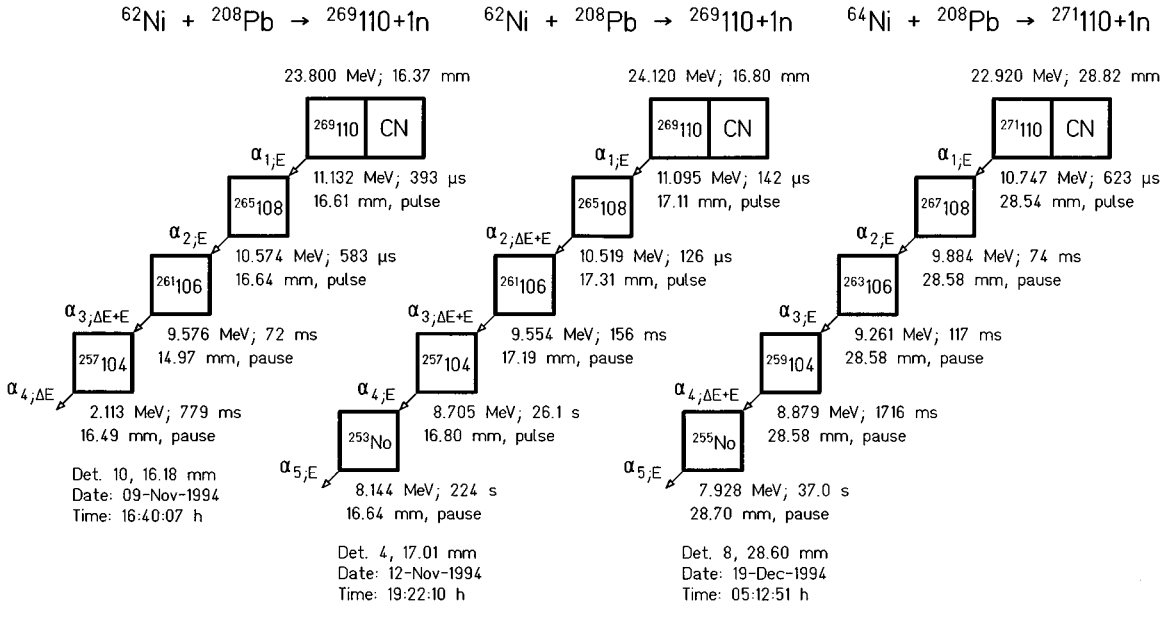

Figure 15 Two decay chains of ^{269}110 observed in ^{208}Pb(^{62}Ni,n) (9) and one decay chain of ^{271}110 from ^{208}Pb(^{64}Ni,n) (102). Measured α-energies, correlation times, and vertical positions are given. Reconstructed total α-energies from a pulse in the implantation detector, E, and a pulse in one of the backward detectors, ΔE, are indicated. It is indicated whether a decay was observed in the beam pulse or the pause.

TABLE 3 Pb/Bi-based reactions, Z = 104–112 at SHIP (1985–1999)

Atomic number	Reaction	Isotope (channel)	Decay mode	Half-life	E^x/MeV	Dose (10^{18})	σ/nb	Number of chains	Reference
104	^{208}Pb(^{50}Ti,xn)	^{257}Rf(1n)	α		10–33	1.4	10 ± 0.5		
		^{256}Rf(2n)	sf, α				12 ± 0.5		9
		^{255}Rf(3n)	sf, α				0.7 ± 0.5		
	^{207}Pb(^{50}Ti,2n)	^{255}Rf	α, sf (52%)	1.6 s	21–24	0.22·	∼10		105
	^{206}Pb(^{50}Ti,2n)	^{254}Rf	sf new	23 μs	22	0.27	2.4 ± 0.2		105
	^{204}Pb(^{50}Ti,1n)	^{253}Rf	sf new	48 μs	16	0.22	0.19 ± 0.04		105
105	^{209}Bi(^{50}Ti,xn)	^{258}Db(1n)	α, EC		16	1.0	4.3 ± 0.4		106
		^{257}Db(2n)	α		22		2.4 ± 0.3		
	^{208}Pb(^{51}V,xn)	^{258}Db (1n)					0.25		
		^{257}Db (2n)			19–25	0.35	0.31		105
	^{209}Bi(^{50}Ti,xn)	^{256}Db(3n)	α, EC	1.9 s	29		0.19 ± 0.04		106
		^{252}Lr	(35%) new						
			α new	0.36 s					
106	^{209}Bi(^{51}V,2n)	^{258}Sg	sf new	2.9 ms	16–25	1.4	(38 ± 13) 10^{-3}		105
107	^{209}Bi(^{54}Cr,xn)	^{262}Bh (1n)	α		19–28	1.0	(163 ± 34) 10^{-3}	38	
		^{261}Bh (2n)	α				$\left(36^{+22}_{-14}\right)$ 10^{-3}		80

108	^{208}Pb(^{58}Fe,xn)	^{265}Hs(1n)	α		11–20	5.5	$(70 \pm 10)\ 10^{-3}$	111	9
		^{264}Hs(2n)	α, sf (50%)		19		$<10^{-2}$	3	
	^{207}Pb(^{58}Fe,1n)	^{264}Hs			19	1.2·	$\left(3^{+5}_{-2}\right)\ 10^{-3}$	1	22
109	^{209}Bi(^{58}Fe,1n)	^{266}Mt	α		23	0.9	$\left(9^{+11}_{-6}\right)\ 10^{-3}$	2	80
					13–17	4.8·	$\left(7.4^{+4.8}_{-3.3}\right)\ 10^{-3}$	12	114
110	^{208}Pb(^{62}Ni,1n)	^{269}110	α new	0.17 ms	12	2.2	$\left(3.3^{+6.2}_{-2.7}\right)\ 10^{-3}$	4	9
	^{208}Pb(^{64}Ni,1n)	^{271}110	α new	56 ms	9–12	2.1·	$\left(15^{+9}_{-6}\right)\ 10^{-3}$	9	102
111	^{209}Bi(^{64}Ni,1n)	^{272}111	α new	1.5 ms	9.4-	2.2	$\left(3.5^{+4.6}_{-2.3}\right)\ 10^{-3}$	3	10
		^{268}Mt	α new	70 ms	12.5				
		^{264}Bh	α new	0.44 s					
112	^{208}Pb(^{70}Zn,1n)	^{277}112	α new	0.24 ms	10	3.4	$\left(1^{+1.3}_{-0.7}\right)\ 10^{-3}$	2	11
		^{273}110	α new	0.12 ms					
		^{269}Hs	α new	9.3 s					

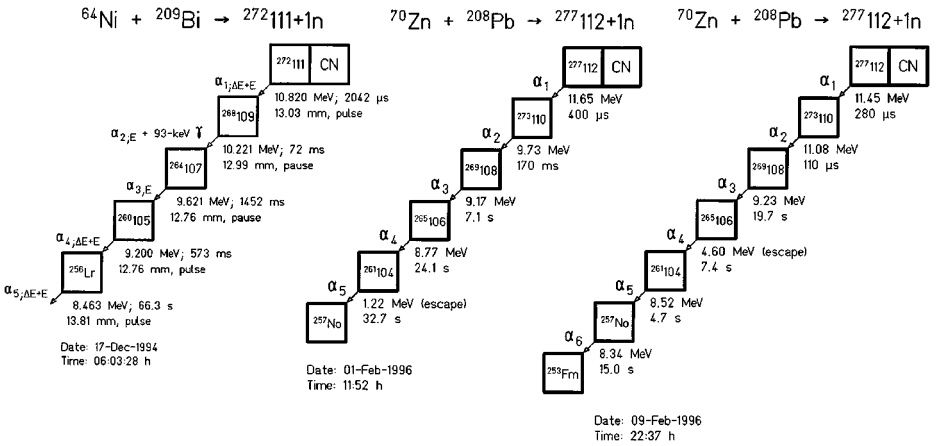

Figure 16 One decay chain of ^{272}111 from ^{209}Bi(^{64}Ni,n) (10) and two decay chains of ^{277}112 from ^{208}Pb(^{70}Zn,n) (11). Measured α-energies and correlation times are indicated.

Three different excitation energies in the range of 11–14 MeV were chosen, giving the excitation function shown in Figure 14. A maximum cross section of 15^{+9}_{-6} pb was measured at $E^x = 12$ MeV. The isotope showed three α-energies: 10.74 MeV, 10.68 MeV, and 10.71 MeV. The half-life of ^{271}110 is $1.1^{+0.6}_{-0.3}$ ms. The correlation time found for the one 10.71-MeV event was much longer than for the other energies, giving a half-life of 56 ms assigned to an isomeric state in ^{271}110. The discovery of ^{267}Hs (101) was confirmed. Alpha energies and the half-life agreed within the error bars, but the 1n-cross section of the ^{208}Pb-based reaction producing ^{267}Hs as a daughter isotope was six times larger than the direct actinide-based 5n-cross section of 2.5 pb.

Discovery of Element 111 The isotope ^{272}111 produced in the reaction ^{64}Ni on ^{209}Bi decayed into the unknown isotopes ^{268}Mt and ^{264}Bh, followed by the known isotopes ^{260}Db and ^{256}Lr (10). Three chains (Figure 16) were found at excitation energies of 11.6 MeV and 13 MeV, resulting in an optimum production energy of 12.5 MeV, the same as was found for ^{271}110 (see Figure 14). One of the three chains was complete. It is shown in Figure 16. Comparing the two known last generations, the correlation times of ^{260}Db and ^{256}Lr are compatible with the published half-lives. The same holds for the α-energy measured for ^{256}Lr, whereas the α-energies found for ^{260}Db are slightly larger than the energies published in 1970 (112). The isotope ^{272}111 is an α-emitter with an α-energy of 10.82 MeV. The full α-energy was observed only once in one of the three chains. Isotope ^{272}111 has a half-life of $1.5^{+2.0}_{-0.5}$ ms. Its production cross section is $3.5^{+4.6}_{-2.3}$ pb. The intermediate new isotopes ^{268}Mt and ^{264}Bh, both α-emitters, were discussed already in Section 4.2. More complete decay chains are desirable to confirm the genetics ending in ^{260}Db and ^{256}Lr, but there is no doubt element 111 was discovered.

Discovery of Element 112 The isotope $^{277}112$ was produced in the reaction ^{70}Zn on ^{208}Pb (11). It decayed by a chain of six α-particles via the unknown isotopes $^{273}110$ and ^{269}Hs to the known isotopes ^{265}Sg, ^{261}Rf, and ^{257}No. The two chains shown in Figure 16 were observed at the excitation energy of 10.1 MeV, an energy chosen by extrapolation from the preceding lighter elements. A third chain was found in the May 2000 experiment at 12 MeV of excitation energy (2). The production cross section of $^{277}112$ is $0.7^{+0.9}_{-0.5}$ pb. Of the two decay chains shown in Figure 16, one presents six generations and the other presents five generations of α-decay. The first chain was the longest chain ever registered, covering a gap of 12 atomic numbers. Correlation times and α-energies observed for ^{265}Sg correspond to the published values (96–98). In chain 1, the half-life of ^{261}Rf is compatible with the published value, but the α-energy of 8.52 MeV found in chain 2 for ^{261}Rf and the short correlation time of 4.7 s are new findings. It has been pointed out in the table of measured mass excesses (109) that the published α-energy of 8.29 MeV cannot be the ground-state transition. The new value meets the expectation for the ground-state α-transition. The α-energy of 8.28 MeV should be assigned to an isomer with a half-life of 78 s; the ground-state transition is proposed to have an energy of 8.52 MeV and a half-life of 6.6 s. The decay chains observed ended twice in ^{261}Rf and once in ^{257}No. In the best case, two times seven data for decay-energies and correlation times of known isotopes would have led back to the isotope $^{277}112$. The correlation times observed for ^{265}Sg, ^{261}Rf, and ^{257}No are compatible with published values and the isomer discussed for ^{261}Rf. The full α-energy of ^{265}Sg was observed only once. ^{261}Rf once showed the α-energy assigned to the ground state, a correct energy release in spontaneous fission, and once an incomplete α-energy. The α-energy measured for ^{257}No agreed with the published decay data. Element 112 is consolidated by 11 numbers concerning known decays reached in three decay chains starting with the isotope $^{277}112$. This, combined with the fact that three α-particles were observed for each of the chains preceding the decay of known isotopes, gives convincing evidence that element 112 was discovered.

The α-energies observed from the isotope $^{277}112$ were 11.45 MeV, 11.65 MeV, and 11.17 MeV. A half-life of $0.48^{+0.35}_{-0.07}$ ms follows from the three correlation times. For the daughter isotope $^{273}110$, the lifetimes and α-energies observed for the three chains vary strongly. $E_\alpha = 9.73$ MeV with a correlation time of 170 ms and $E_\alpha = 11.08$ MeV, 11.20 MeV with $\Delta t = 110\ \mu$s and 310 μs point to distinctly different levels. Two half-lives, 146 μs and 118 ms, are assigned to $^{273}110$ for the α-energies 11.08 MeV, 11.20 MeV, and 9.73 MeV, respectively. The energies and the correlation times are compatible with two $\Delta\ell = 0$ transitions between $^{273}110$ and ^{269}Hs. High-spin isomers and low-spin ground states in the two isotopes could be bridged by the α-decays observed. Starting from different levels in $^{277}112$, chain 1 may connect high-spin states and chain 2 the corresponding low-spin states. In this case, chain 2 connects the ground states of the first three isotopes and the chain continues populating the low-spin ground states of ^{265}Sg, ^{261}Rf, and ^{257}No. This would explain the higher α-energy of 8.52 MeV that was observed for

^{251}Rf. The correlation time of 14.5 s observed in the spontaneous-fission decay is compatible with a ground-state transition. The low-spin ground state of ^{261}Rf would have a spontaneous-fission branch populated by α-decay of ^{265}Sg, not seen in the abundant decay events observed for the isomer of ^{261}Rf. The transition from high to low spin states occurs in ^{269}Hs via a high-spin isomer at 1.35–1.55 MeV excitation energy, populated by the 9.73-MeV α-decay observed in chain 1. The interpretation of chain 2 and the third chain found in the May 2000 experiment as connecting ground states gives two high-energy α-rays (11.45 MeV and 11.08 MeV) followed by a 9.23-MeV α-particle. Such a pattern is characteristic of a chain passing the N = 162 closed shell between ^{273}110 and ^{269}Hs. It is seen in the sequence ^{217}Ra-^{213}Rn-^{209}Po at N = 126 and in ^{261}Sg-^{257}Rf-^{253}No at N = 152 as well. The 1-n shell gap deduced from the two-neutron binding energies at the shell crossing is 0.9 MeV for N = 162, 0.40 MeV at N = 152, and 1.2 MeV at N = 126. The shell strength of N = 162 falls between the weak shell N = 152 and the strong shell N = 126.

The new isotope, ^{269}Hs, discovered in the third generation of the ^{277}112 chains, is an α-emitter with an α-energy of 9.19 MeV and a half-life of 11.3 s. This half-life is longer than that of ^{267}Hs by a factor of 200. Compared with its isotone ^{271}110, the half-life increased by a factor of 10^4. The most long-lived isotopes for a shell at N = 162 are nuclei with N = 161. Up to ^{270}Mt, these isotopes should live long enough for chemistry studies. In the reactions of ^{26}Mg on ^{248}Cm and ^{249}Bk, they are accessible in 5n-reactions. In 1n-reactions they are produced as the third member of the ^{277}112 and the elusive ^{278}113 chains.

The ^{34}S/^{238}U experiment at FLNR (72), aiming at the discovery of element 110, led to the conclusion that a closed shell exists at N = 162. Five chains were published, which were selected from criteria described in the text. The energy of the implanted ^{273}110 should fall within reasonable margins, at least one daughter isotope should be found within a pause interval between beam pulses, and the known decay data of the four daughter isotopes should match published values. Three out of the five sequences showed in the pauses the α-energy of ^{265}Sg. The sum correlation time from ^{269}Hs and ^{265}Sg was 27 s. Sequences 2 and 3 had correlation times as required for ^{265}Sg, whereas sequence 1 had a very long correlation time of 158 s, occurring on a few-percent probability level. In this sequence, 6.5 min after the first decay, a second α-decay with an energy compatible with ^{257}No followed. Since it was observed in the beam pulse, it was probably a random event. None of the sequences showed any decay of ^{269}Hs, ^{261}Rf, and ^{257}No in the pause intervals. To have found ^{265}Sg three times out of 3×4 possible decays is worrisome, as there exists another isotope with the same decay data as ^{265}Sg, the 25-s isomer of ^{211m}Po. From the findings presented it is impossible to claim discovery of ^{273}110, let alone the shell closure of N = 162. Yet the discussion went on. The measured α-energies for the three sequences for the decay of ^{273}110 are 11.35 MeV, 11.72 MeV, and 10.57 MeV. The one-neutron shell gaps that follow are 1.01 MeV, 1.38 MeV, and 0.23 MeV, respectively. The shell gap for sequence 2 is larger than the gap at N = 126; the gap of sequence 3 is close to no shell

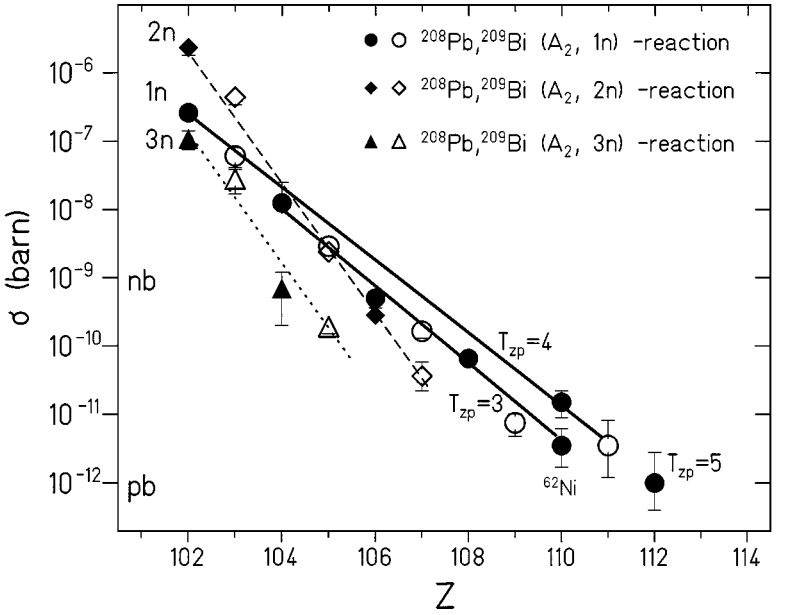

Figure 17 The xn production cross sections of Pb/Bi-based reactions for elements Z = 102–112 (for x = 1,2,3). Solid symbols represent ^{208}Pb and open symbols ^{209}Bi.

at all. It is only sequence 1, with its intermediate α-energy of 11.35 MeV, which allows any discussion of the theoretically expected shell gap at N = 162, and this chain was selected. It was not the data that determined the final selection of one of the three sequences but the maximum resemblance of the sequence to a picture based on information outside the experiment.

Production Cross Sections The 1n production cross sections for ^{208}Pb/^{209}Bi-based reactions starting with ^{48}Ca/^{208}Pb (0.26 μb) (113) and ending with ^{70}Zn/^{208}Pb (0.7 pb) are presented in Figure 17 along with 2n and 3n cross sections. As a function of the atomic number of the element produced, all cross sections decrease rapidly. 2n and 3n cross sections break down faster than 1n cross sections. The latter decrease regularly for e-e projectiles of constant isospin between ^{50}Ti and ^{62}Ni, with a small advantage for the Pb-based reactions leading to even-Z elements. This finding is corroborated by a recent experiment in which ^{58}Fe (^{209}Bi,n) gave $\sigma = (7.4^{+4.8}_{-3.3})$ pb for ^{266}Mt (114). This experiment showed that the cross section to synthesize ^{266}Mt is a factor of two smaller than that interpolated between ^{265}Hs and ^{269}110 (9). The isospin value of projectiles ^{48}Ca and ^{64}Ni is larger by one unit than the heaviest projectiles in between. The cross section for the ^{64}Ni-induced reaction was larger than that for the ^{62}Ni-induced reaction by about a factor of five, an increase attributed to the larger isospin. This interpretation seemed to be confirmed by the cross section for ^{64}Ni/^{209}Bi, which decreased as expected for

the production of ^{272}111 by a factor of about four. Proceeding to the projectile ^{70}Zn, once more increasing the isospin by one unit, the cross section going to Z = 112 still decreased, despite the expectation of a compensating effect from the larger isospin value. The production cross section of ^{277}112 fell to 0.7 pb. The larger cross sections for production of ^{271}110 and ^{272}111 could be due not to the larger isospin of the projectiles but to larger shell corrections in the compound systems, which both fall on the N = 162 shell. Larger fission barriers due to larger microscopic corrections could have boosted the cross sections. The compound system ^{278}112 at N = 166 has smaller shell corrections than ^{276}112, which is accessible by ^{68}Zn projectiles; that is, there might be a larger cross section for ^{68}Zn/^{208}Pb than for ^{70}Zn/^{208}Pb. However, a ^{68}Zn experiment applying a larger dose than that used in the ^{70}Zn experiment gave an upper limit of 1.2 pb for the cross section, which was smaller than the upper limit of 2.3 pb obtained in the ^{70}Zn experiment (107). Another important parameter concerns closed shells in the projectiles. The projectiles $^{48}_{28}$Ca, $^{50}_{28}$Ti, ^{62,64}Ni$_{28}$, and $^{70}_{40}$Zn show shell closures at Z = 20,28 and N = 28,40. A smaller hindrance in the entrance channel for the more rigid closed-shell nuclei was also observed for nearly symmetric collision systems (see Section 5.3). The neutron shell at N = 40 is known from ^{68}Ni (115). It could help to raise the cross section for ^{70}Zn.

More experiments are needed to disentangle the interplay of manifold parameters, each of which might change the cross sections by factors of up to 3. Although small, such factors are important at the experimental limits in the 1 pb-range. They cannot change the continuous decrease of cross sections, which reflects the increasing disruptive macroscopic Coulomb forces in the system, but they may decide whether we can reach element 113 or not. The extrapolated cross section for ^{70}Zn/^{209}Bi is 0.3 pb. An experiment applying a dose of $7.5 \cdot 10^{18}$ ions, which was larger by a factor of 2.2 than that of the experiment producing two chains of ^{277}112, gave no trace of Z = 113 (116), with a 2σ upper limit of 0.6 pb for the production cross section. The chosen excitation energy of 10 MeV might have been smaller than optimal. The May 2000 experiment at a slightly higher energy of 12 MeV, intended to repeat the successful Z = 112 experiment, gave another chain, but the cross section did not increase (2). A new search for Z = 113 is planned at an improved luminosity of SHIP in the near future at GSI.

Complete capture of a medium-weight projectile by the heavy target nucleus without any neutron emission, observed in the γ-channel, could be an alternative in the range of E^x = (4–10) MeV. For thermal neutron capture reactions, the cross sections for capture and fission are of the same order of magnitude when the compound nucleus lives long enough to profit from γ-deexcitation, which needs times of the order of (10^{-14}–10^{-18}) s. We have investigated heavy-ion capture reactions for $E^x < Bn$ in ^{208}Pb(^{82}Se, γ)^{290}116 (107). Close to the fusion barrier (111) for the chosen reaction, the γ-channel is the only deexcitation mechanism. A cross section upper limit of 5–6 pb was reached in the range E^* = (4–10) MeV. An analogue to thermal neutron capture in heavy-ion reactions can be excluded. The life-time of the compound system is much shorter than the time for cooling by γ-emission.

TABLE 4 Reactions with upper 2σ cross section limits at SHIP (1985–1999)

Atomic number	Reaction	Isotope	E^x/MeV	Dose (10^{18})	σ/pb	Reference
110	^{208}Pb(^{64}Ni,1n)	^{271}110	15–21	1	<12	81
110	^{235}U (^{40}Ar,4n)	^{271}110		1.7	<8	81
112	^{208}Pb(^{68}Zn,1n)	^{275}112	10–14	5	<1.2	107
113	^{209}Bi(^{70}Zn,1n)	^{278}113	10	7.5	<0.6	116
116	^{208}Pb(^{82}Se,γ)	^{290}116	0–8	2.6	<8	107
	^{208}Pb(^{82}Se,1n)	^{289}116	11		<10	
118	^{208}Pb(^{86}Kr,1n)	^{293}118	13–15	2.9	<1.0	161

Table 4 summarizes the unsuccessful experiments performed at GSI since 1985. More than 40% of the total dose of $5 \cdot 10^{19}$ ions applied to targets during that time gave only upper cross section limits, and did not result in the production of any new isotopes or elements. These studies are the price of finally finding a successful path and are as necessary as the winning experiments. They assure that the best way for the successful synthesis reactions has been chosen.

The recent LBL experiment irradiating ^{208}Pb by ^{86}Kr aiming at $^{293}_{175}$118 is discussed in the last section of this article (117).

5. THE PRODUCTION MECHANISM OF FUSION EVAPORATION RESIDUES

The production cross section of SHEs in a two-stage formation model, with a first short formation stage of a compound nucleus and a second longer stage of its deexcitation, is written as a formula with three factors:

$$\sigma_{\mathrm{EVR}} = \pi\lambda^2\ell^2_{\mathrm{lim}} \cdot \mathrm{W}\left[\prod_{\mathrm{i}=1}^{\mathrm{i_{max}}}(\Gamma_{\mathrm{n}}/\Gamma_{\mathrm{f}})_i, E^*\right] \cdot \mathrm{p}(\mathrm{B_B}, \mathrm{E_{c.m.}}). \qquad 7.$$

The formation probability of a compound system and the survival probability in deexcitation are governed by very different physics. Formation depends mainly on the growing Coulomb forces in the process, which are very different for mass-symmetric and mass-asymmetric collision systems, whereas the deexcitation losses are governed by the height of the fission barrier in the compound nucleus. In both stages of fusion, nuclear structure is important.

The first factor in Equation 7 is the compound nucleus formation cross section for an unhindered fusion process producing a nonfissioning EVR in a reaction limited by an upper value ℓ_{lim} for the angular momentum. The fission barrier of highly fissionable nuclei is reduced (19) to $1/e$ of its $\ell = 0$ barrier height at

$\ell_{lim} = 15\hbar$. At this value, the formation cross section $\pi\lambda^2\ell_{lim}^2$ of the fissionable compound nucleus has values at the fusion barrier of 5–50 mb. In contrast, the formation cross sections of SHEs are as small as 1 pb, the value reached for the production of element 112. Thus, the loss during formation of the compound nucleus p (B_B) and its deexcitation is a factor of 10^{-10}. Understanding the different processes contributing to this miniscule survival branch is a challenge to experimentation and theory.

The second factor in Equation 7 describes the deexcitation of the compound system (see Section 5.1). Of interest here is deexcitation of a fissionable nucleus by a cascade of i neutrons from an excitation energy E^*. To calculate this factor, assuming that the system has reached equilibrium, we use the evaporation code HIVAP (118). The deexcitation losses are well understood for the deformed isotopes of elements Z = 96–102 and were intensively studied using actinide targets with Z = 94–98. They were discussed by Reisdorf & Schädel (119) in their recent survey of our understanding of this part of EVR formation. The deexcitation of spherical isotopes gave a surprise, as the large shell-correction energies of isotopes close to N = 126 did not increase the survival probabilities against fission (19). To understand the large fission losses, the concept of collective enhancement of level densities and the rapid disappearance of shell corrections with increasing excitation energy is invoked.

The third factor in Equation 7 describes, at a chosen bombarding energy E, the formation process characterized by a fusion barrier of the compound nucleus (see Section 5.2). We use the barrier description of Reference 111, which gives a simple formula for the fusion barrier B_B that is in good agreement with experiments. At $E_{c.m.} = B_B$, the fusion probability $p(E_{c.m.},B_B)$ has a value of 0.5 for unhindered fusion, but for the systems we are interested in, $p(B_B)$ may take very small values. The hindrance in the entrance channel was well established by investigating symmetric collision systems giving EVRs for elements in the range Z = 82–92. The work was reviewed by Schmidt & Morawek (120) and presented in one of my Varenna lectures (121).

The basic assumption of the analysis of two well-separated stages, formation and deexcitation, might not be fulfilled for steadily increasing disruptive Coulomb forces between the partners. Evidence is accumulating for a possible one-step direct reaction mechanism in case of the 1n-production reactions for SHEs (see Section 5.3). Precompound deexcitation may be essential to produce EVRs; otherwise the collision complex would immediately reseparate.

5.1 The Deexcitation of Fissile Compound Nuclei

The deexcitation by neutron emission of an excited highly fissile nucleus is governed by its excitation energy E^x and by the i-fold product of the Γ_n/Γ_f ratios of the i single steps in the neutron evaporation cascade, with Γ_n and Γ_f the corresponding decay widths for neutron emission and fission in the i^{th} step. Given an excitation energy $E^* > B_n > B_f > T$, a simple expression for Γ_n/Γ_f is valid, as

used in the following (122):

$$(\Gamma_n/\Gamma_f)_{\text{intrinsic}} = 0.14/\text{MeV} \cdot T \cdot A^{2/3} \exp[-(B_n - B_f)/T]. \quad 8.$$

The difference between B_n and B_f predominantly determines the survival probability against fission of the compound nucleus. For small values of E^*, Γ_n/Γ_f becomes rapidly smaller as the compound nucleus temperature T decreases. The last step in the cascade shows the smallest survival probability against fission. At energies of the 1n channel ($E^x \geq 10$ MeV) and with $(B_n - B_f) \geq 4$ MeV, Γ_n/Γ_f reaches its smallest values for the last neutron of the cascade, close to $2 \cdot 10^{-3}$. At 50 MeV excitation energy, corresponding to 5n reactions, the first neutron in the cascade has a Γ_n/Γ_f value close to 0.4. This estimate follows from an analysis of measurements of the deexcitation of No isotopes (123). For 1n reactions the total loss due to neutron-fission competition is about 10^{-2}, whereas for a 5n reaction the value is close to 10^{-5}. 1n production cross sections of about 100 μb and 5n cross sections of the order of 100 nb are estimates based on the losses discussed. The cross sections that are observed for isotopes produced by actinide-based reactions such as ^{238}U (^{22}Ne, 5n) ^{255}No, $\sigma = 60$ nb, indeed are of the order of the estimate, whereas all observed 1n reactions in Pb/Bi-based sections never reach the above estimated value. The largest σ value observed in ^{48}Ca(^{208}Pb,n)^{255}No (113) is 0.26 μb, which points to additional Γ_n/Γ_f losses that are larger by two to three orders of magnitude. In Section 5.3, this additional loss is connected to precompound emission.

The fission barrier B_f is the sum of the barrier calculated from a macroscopic model B_{LD} and the shell corrections δU_{eff} for the ground-state and saddle-point configurations, as discussed in Section 2.1 and shown in Figure 3*b*.

$$B_f = B_{LD} + \delta U_{\text{eff}}. \quad 9.$$

Shell corrections at saddle-point configurations are smaller than ground-state shell corrections. The actual barrier will be smaller by 1–2 MeV than the estimate from the ground-state shell correction. The static fission barriers that govern the losses for an equilibrated compound system have been calculated for elements between Rf and $Z = 116$ (29). Inserting Equation 9 into Equation 8 shows that shell corrections increase Γ_n/Γ_f by a factor of exp ($\delta U_{\text{eff}}/T$). Heating the nucleus destroys the microscopic order, giving stability against fission, which was the necessary condition for the existence of SHEs. Thus, the microscopic corrections disappear with increasing excitation energy. Shell effects (124) are damped exponentially (124, 125): $\delta U = \delta U_0 \exp(-\gamma E^*)$ with $\gamma^{-1} = 5.48\ A^{1/3}/(1 + 1.3\ A^{-1/3})$. The analysis of actinide-based reactions using the HIVAP code showed that δU contributes to stabilization as expected. The produced isotopes of elements $Z =$ 96–105 are prolate in their ground state ($ß \sim 0.2$). These deformed nuclei were produced in hot fusion reactions mainly by 4n and 5n reactions at compound nucleus excitation energies of up to 50 MeV, equivalent to a temperature of $T =$ 1.4 MeV. For the shell corrections of these deformed EVRs, a 1/e damping

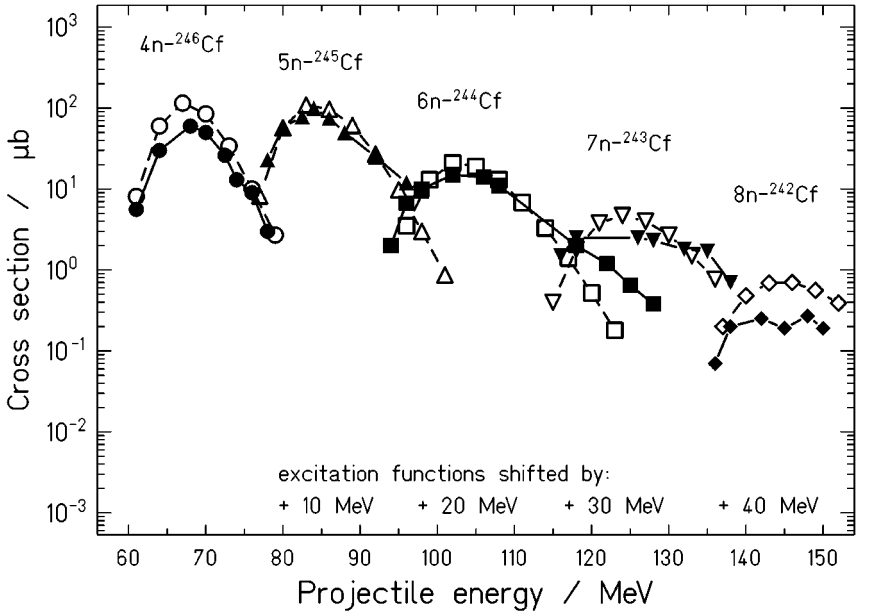

Figure 18 Excitation functions for $^{238}U(^{12}C,xn)^{250-xn}$ with x = 4–8. Open symbols, experimental data (126); solid symbols, HIVAP calculations (119).

energy of about 27 MeV reproduces the cross sections for the hot xn reactions. Figure 18 presents a recent analysis of production cross sections in the reaction $^{249}Cf(^{12}C, xn)^{261\text{-}nx}$ Rf (119, 126). It demonstrates the excellent agreement with the description by the HIVAP code.

A very different temperature dependence is observed for heavy systems when spherical closed-shell nuclei are involved. For the N = 126 spherical nuclei in region 3 of Figure 2 (see color insert), which have about equal values for the shell-correction energies and liquid-drop barriers, reactions of different entrance-channel asymmetry leading to Th compound nuclei were investigated. Via 4n reactions at $E^x \approx 40$ MeV, Th isotopes were synthesized using targets of Pb, Hf, and Yb isotopes and the corresponding projectiles ^{18}O, ^{40}Ar, and ^{48}Ca (120, 127, 128). Figure 19*a* shows the survival probability for 4n reactions leading to spherical Th isotopes around the N = 126 shell. Analysis of the data showed that the large shell corrections to the fission barriers do not lead to increased production cross sections. EVR cross sections of less than 10^{-2} of the calculated values are observed.

The early experiments were corroborated in further recent experiments at GSI. At relativistic energies, the production of fragmentation products along N = 126 becomes possible using collisions of ^{238}U projectiles with lighter target atoms (125). At the end of a long cascade of evaporated nucleons at $E^* = 20$–30 MeV, the strong increase of the fission barrier due to the ground-state shell-correction energy should give the EVRs a higher survival probability (see Figure 19*b*). This

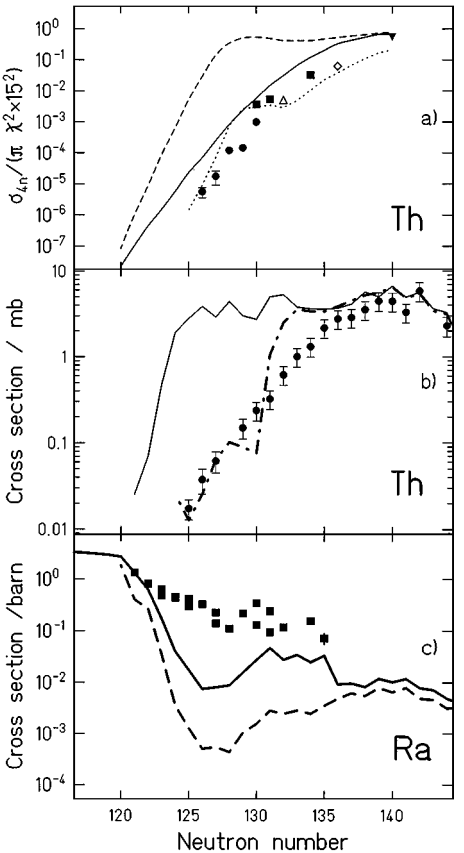

Figure 19 (*a*) 4n cross sections for the production of Th isotopes ($E^x = 40$ MeV) as a function of the neutron number of the residue ^{48}Ca+Yb (solid squares), ^{40}Ar+Hf (solid circles), ^{16}O+^{206}Pb (open triangle), ^{18}O+^{208}Pb (diamond), α+^{226}Ra (solid triangle). The factor $1/(\pi\lambda^2\ 15^2)$ removes entrance-channel effects for different target-projectile combinations. It makes the ordinate scale equal to the survival probability $\Pi(\Gamma_n/\Gamma_{tot})$, calculated for zero angular momentum using the HIVAP code for liquid-drop barriers (solid line), for microscopically corrected barriers (dashed line), and with collective enhancement included (dotted line) (120). (*b*) Production cross sections of Th isotopes from relativistic ^{238}U-fragmentation reactions ($E^* \sim 20$ MeV) compared to calculations that take into account the level densities of intrinsic levels with (dashed-dotted line) and without (dashed line) collective enhancement (125). (*c*) Cross sections for electromagnetic fission ($E^* = 11$ MeV of Ra isotopes) in 450 MeV/A collisions on Pb of fragmentation products from relativistic ^{238}U-fragmentation reactions compared to calculations that take into account the level densities of intrinsic levels with collective enhancement (dashed line). Collective enhancement and damping of shell corrections with $\gamma = 5.4$ MeV produces the solid line (129).

was not observed. The cross sections of Th isotopes were 100-fold smaller than expected.

In a further experiment, isotopically pure beams of ^{238}U fragmentation products of elements Z = 84–90 passed through a Pb target. In secondary collisions with Pb atoms, the fragmentation products experienced the strong virtual electromagnetic field between the collision partners (129). The electromagnetic response function of the fissile fragments showed a maximum near the energy of the giant dipole resonance. The expected decrease of the fission cross section at N = 126 was not found (see Figure 19*c*). Even when the excitation energy of the fissioning nuclei in the secondary-beam fission experiment was as low as 11 MeV (T = 0.7 MeV), most of the cross section went into fission.

The ground-state shell corrections for N = 126 nuclei are determined from α-decay data and there is no doubt that these nuclei are shell-stabilized. The lack of observation of the stabilization even at small excitation energy tells us that there must exist a mechanism reducing the Γ_n/Γ_f values by several orders of magnitude for the spherical nuclei, which is not present for the deformed ones. A mechanism called collective enhancement of level densities was proposed by Ericson (130) and further developed by Bjornholm et al (131) to modify Γ_n/Γ_f. Shell corrections δU_{eff} (Equation 9) and collective enhancement $K_{coll.enh.}$ are introduced into Equation 8. For (Γ_n/Γ_f) coll.enh. we obtain

$$(\Gamma_n/\Gamma_f)_{coll.enh.} = 0.14/\mathrm{MeV} \cdot T \cdot A^{2/3} \cdot \exp[-(B_n - B_{LD})/T] \cdot \exp(\delta U_{eff}/T)/K_{coll.enh.} f(E^*/E_{crit}), \quad 10.$$

with $K_{coll.enh.} = K_{rot}^{saddle}/K_{vib}^{grst}$.

Collective excitations, such as rotation and vibration, enhance the level density up to excitation energies characterized by a critical energy, E_{crit}, defined as the cutoff energy of a Fermi function, $f(E^*/E_{crit}) = [1 + \exp(E\text{-}E_{crit})/d_{crit})]^{-1}$, above which the notion of collectivity and collective states loses justification. Values of E_{crit} = 40 MeV and $d_{crit} = (1/4)\ E_{crit}$ were determined from the data (125). Because the shell stabilization is damped to 0.2 of its full value at about the same excitation energy, the notion of collective enhancement and the concept of SHEs both break down in the energy domain of 40–50 MeV. Collective enhancement of the level density should not be neglected when calculating the fission losses in SHE production. Yet it has not become part of the analysis in heavy-element synthesis reactions. The level density enhancement depends on the nuclear structure of the nucleus. It is different for the ground-state level densities, which determine the value of Γ_n, and the saddle-point level densities, which govern Γ_f. The difference in level densities between the two configurations will be large in the case of changing nuclear structure. For axially deformed nuclei ($ß_2 \sim 0{,}2$) and for their saddle-point configuration, again assumed to be axially deformed, rotational levels will be observed in both of the configurations with about the same level density. For axially deformed nuclei, collective enhancement corrections of Γ_n/Γ_f are lost in the uncertainties of the calculations, which explains why all actinide-based fusion

reactions to date are described so well by standard evaporation theories, as shown in Reference 119. As one approaches fissile spherical closed-shell nuclei, nuclear structure changes rapidly. The saddle-point configuration stays with its axial deformation and high values of the enhancement factor K_{rot}, but the spherical nucleus has few levels and shows only a small increase of its level density, by vibrational levels, which are energetically spread over much larger energies than the rotational levels at the saddle point. K_{rot} was defined in Reference 131 and this definition was retained in later publications (119, 124). For axially symmetric prolate nuclei,

$$K_{rot} = \sigma^2_{\perp} = 1.4\ 10^{-2} \cdot A^{5/3} \cdot T \cdot (1 + \beta_2/3), \qquad 11.$$

with $\sigma^2_{\perp}$ the spin cutoff factor for the deformed nucleus. The enhancement factor $K^{gr.st.}_{vib}$ was parameterized by a fit to the experimental data of Reference 125 and is negligible compared with K^{saddle}_{rot} for the saddle-point configuration. Shell corrections and collective enhancement compensate each other, as seen from Equation 10.

The concept explained the fusion data and is now applied to the new experiments (120, 125, 129). Full compensation could not be achieved for the data shown in Figure 19*c* (129). The high fission cross section for Ra isotopes is reproduced only if, for the deexcitation of these spherical nuclei, the damping energy γ is drastically reduced to 5–6 MeV. This result corroborates the interpretation of the very first experiments on fusion cross sections in the $N = 126$ range (19, 127).

All the different independent experiments showed that the increase of the fission barrier of the shell-stabilized nuclei with $N = 126$ does not, as had been expected, increase the survival probability against fission even at temperatures as low as $T = 0.7$ MeV. At excitation energies of a 1n channel (12 MeV), spherical EVRs hardly profit from the shell stabilization of their ground states. The purely shell-stabilized spherical SHEs predicted around $^{292}_{172}120$ and $^{304}_{184}120$ should behave like their shell-stabilized spherical counterparts at $N = 126$. Actinide-based fusion reactions using ^{48}Ca beams (73), or the reactions proposed in Reference 132 using two deformed rare earth nuclei, do reach spherical nuclei. They lead to excitation energies of the compound systems in the range of $E^* = 30$ MeV, which should show reduced stability against fission in each step in their decay cascades. ^{208}Pb-based reactions using ^{86}Kr beams (117) reach smaller excitation energies (12 MeV) and are certainly less affected. To synthesize SHEs with spherical nuclei, reactions with an excitation energy as close to the fission barrier as possible should be chosen, such as radiative capture and 1n reactions.

5.2 The Entrance Channel Limitation of Fusion Reactions

All large-scale rearrangement processes at low temperature, such as fusion and fission, are ruled by the same laws: a combined base of macroscopic forces, modified by the microscopic structure of the nuclear system (133). In the dynamics of such a system at low temperatures, not only conservative forces and inertia parameters

but also velocity-dependent dissipative forces are important. Moreover, the high density of excited states of the evolving system plays an important role. Small branches in the space- and time-dependent dynamical development occurring with a probability of the order 10^{-10} to 10^{-12} produce an EVR in fusion with a cross section of 1 pb.

However, the theory of nuclear reactions between two heavy nuclei at energies close to the fusion and fission barriers successfully describes the rearrangement down to branches occurring with a probability of 10^{-3}. Examples are cold fission, fission channels, the o-e staggering of element distributions in fission, and the partition of reaction flux between inelastic, deep-inelastic, quasi-fission, and complete fusion. The small branches of 10^{-10} to 10^{-12} that are accessible to experiments in fusion and fission demand a new comprehensive nuclear theory that describes quantitatively the rearrangement reactions between a few hundred nucleons. Even if the physics of such a theory is already correct, it is still far from making predictions about the very rare branches of the process. Careful observation of trends in the experimental data cannot replace theory, but when theory is lacking, it serves as a guideline for the experiments. The analysis presented in the following connects data on cross sections, barrier shifts, and fluctuations to macroscopic models of dissipative dynamics (134).

The experiments on fusion and deep-inelastic reactions of colliding heavy ions at the Coulomb barrier performed at GSI between 1976 and 1988 (77, 78) have shown that, in agreement with theoretical predictions (135), the formation of an equilibrated compound system breaks down for very heavy systems as a consequence of the increasing ratio of electrostatic Coulomb and nuclear surface forces in the amalgamating collision system. For high values of this ratio, the cross section for production of EVRs in xn channels at the fusion barrier decreases exponentially with the atomic number of the fused system, as shown for symmetric collision systems ($Z > 84$) (Figure 20), for Pb/BI-based fusion ($Z > 102$) (Figure 17), and for actinide-based fusion reactions ($Z > 102$–104) (Figure 13). The exponential disappearance of fusion over a small range of atomic numbers has been expressed by a generalized effective fissility, and the postulated onset of dissipative losses in the entrance channel (135) has been related to the observation of an increasing width of the distribution of fusion barriers (120, 128, 136). The small probability of fusing at the Coulomb barrier and reaching a compound system without losing collision energy by dissipative processes in the entrance channel, i.e. the fusion probability at the Coulomb barrier, has been shown to depend exponentially on the atomic number (121).

The Effective Fissility A measure of the ratio of the macroscopic Coulomb and surface forces for an amalgamated nuclear system (the monosystem) is the fissility $x_0 = (Z \cdot f(I)/101.8)$. It is proportional to Z, the atomic number of the nucleus, and to a function $f(I) = (1 - I)/(1–1.78\, I^2)$, where $I = (N - Z)/(N + Z)$. For the heaviest nuclei accessible by fusion, this function is nearly constant with a value of 0.86, and the fissility can be written as $x_0 = Z/117.8$. For a binary system

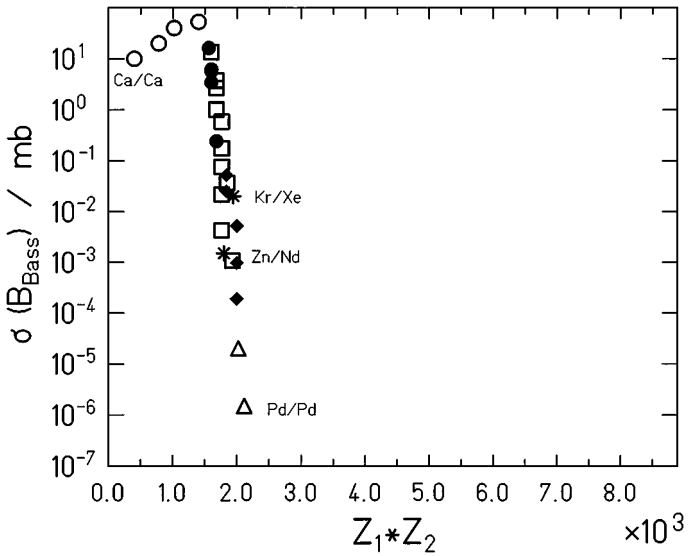

Figure 20 Evaporation residue production cross sections at the Bass barrier for nearly symmetric collision systems. Circles indicate data from Reference 153; diamonds, from Reference 128; squares, from Reference 136; triangles, from Reference 120; asterisks, from Reference 152.

of two touching nuclei with equilibrated charge densities, Bass (137) derived the expression $x_\infty = x_0 \cdot f(\kappa)$ with $f(\kappa) = 4/(\kappa^2 + \kappa + \kappa^{-1} + \kappa^2)$ and $\kappa = (A_1/A_2)^{1/3}$. The term $f(\kappa)$ takes into account the decreasing Coulomb energy between mass-asymmetric collision partners. The effective fissility x of a fusing system is a weighed mean of the fissilities of the mono- and binary system,

$$x = [Z \cdot f(I)/101.8] \cdot [(1-\alpha) + \alpha f(\kappa)]. \qquad 12.$$

The weight of the binary system α is taken as $1/3$ in Reference 135. Differentiating Equation 12 according to Z gives the number of protons, ΔZ, needed to compensate the addition of one neutron in the effective fissility. Figure 21 shows that adding neutrons to the heavy partner helps to reduce x, as expected. Adding neutrons to the light partner may do the contrary. A very asymmetric collision system has, at constant mass of the compound system, a lower x value than a more symmetric one, and this fact neutralizes the decrease of x expected for a higher number of neutrons in the light partner.

The Extra-Push Concept To compensate the mean dissipative losses on the path toward the equilibrated compound system, Swiatecki (134) introduced the concept of an extra-push energy, E_X. The system cannot fuse at the Coulomb barrier E_B, but at a higher barrier $E_F = (E_B + E_X)$. E_X is proportional to $(x - x_{thr})^2$, where

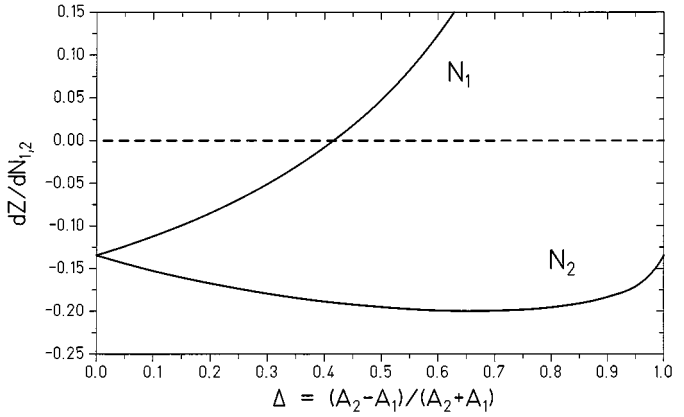

Figure 21 Number of protons ΔZ needed to compensate in the effective fissility the addition of ΔN neutrons calculated for neutrons in the heavy (N_2) and in the light (N_1) collision partner, calculated using Equation 12 for $Z = 110$, as a function of the asymmetry Δ.

$x_{thr} = 0.72$ is the fissility indicating the onset of dissipative losses. This threshold value had been predicted by Sierk & Nix (138) in 1973. The same group later published a slightly higher threshold value (139) of $x_{thr} = 0.74$. Fröbrich & Gontchar predict an earlier onset of $x_{thr} \sim 0.69$ (140). The extra-push energy is given by

$$E_X = a(x - 0.72)^2 \qquad 13.$$

with a slope constant a. The value of a is the same for References 134 and 139, but Reference 140 predicts a smaller value. Experimental values of E_x for nearly symmetric systems (120, 128, 136) and for the Pb- and Bi-based systems on ^{48}Ca and ^{50}Ti (106, 113) are collected in Figure 22*a*.

Distribution of Fusion Barriers The probability to find a barrier at E_B and to fuse at this barrier is

$$p(E_B) = 0.5 \exp - \left[(E_F - E_B)^2/2\sigma_B{}^2\right] = 0.5 \exp - \left(E_x{}^2/2\sigma_B{}^2\right). \qquad 14.$$

This assumes not a single barrier, as in the extra-push model (134), but a Gaussian distribution of barriers with σ_B the variance of the distribution. Experiments showed (128, 136) that σ_B^2 increases with E_X linearly or slightly more strongly, but certainly not quadratically (see Figure 22*b*). Taking

$$\sigma_B{}^2 = c_1 E x^{3/2} \qquad 15.$$

with $c_1 = 0.52$ from a fit to the data gives $p(E_B) = 0.5$ exp[–const $(x - x_{thr})$]. Interpreting microscopically the passage of the level crossings on the path toward the compound system as a random walk process, the square of the variance $\sigma_B{}^2$ should be proportional to the number n of passed level crossings. Assuming equal

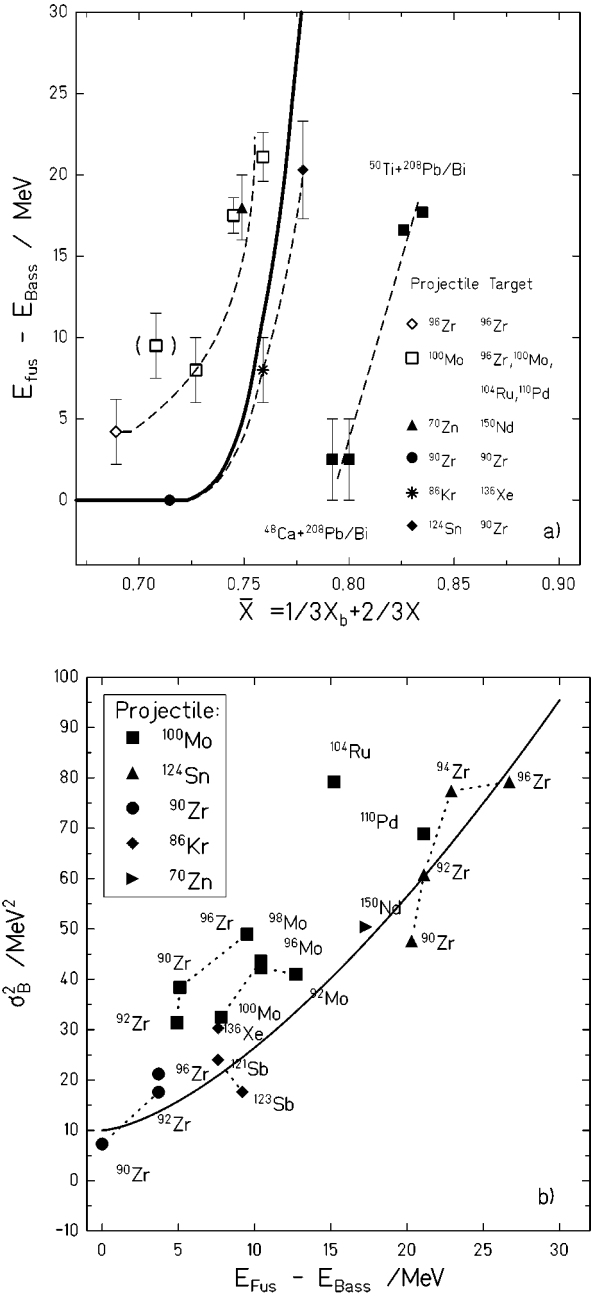

Figure 22 (*a*) Measured barrier shifts (extra-push) for the collision systems, as shown in Figure 20, ^{48}Ca/^{208}Pb or ^{209}Bi (113), and ^{50}Ti/^{208}Pb or ^{209}Bi (9, 106). (*b*) The variance σ_B^2 of the barrier distribution versus the barrier-shifts (extra-push) for the collision systems, as shown in Figure 20. The line is a fit to Equation 15 with $c_1 = 0.52$.

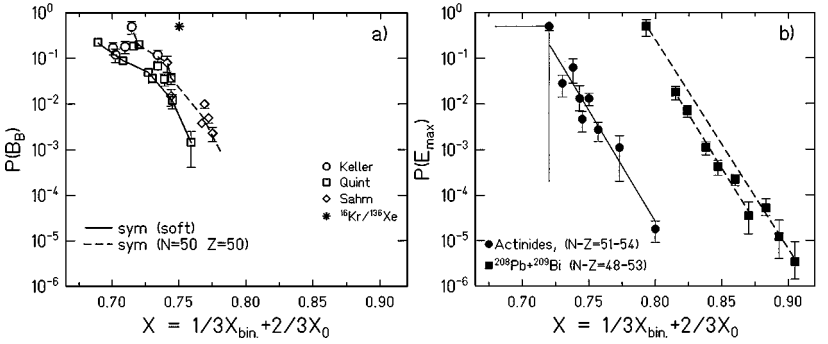

Figure 23 $p(B_B)$ as a function of the effective fissility (*a*) for nearly symmetric collisions and (*b*) for Pb/Bi-based and actinide-based systems.

dissipative losses and distances between two adjacent crossings, n should become proportional to E_X. For higher densities of crossing levels at increasing E_X values, n could increase faster; thus, the experimental $E_x^{3/2}$ dependence may have a plausible explanation (121).

Attempts to include fluctuations in the framework of macroscopic approaches to fusion have been made by Fröbrich & Gontchar (140) and by Aguiar et al (141), who applied them successfully to symmetric collision systems. Recently, Blocki et al (142) introduced the concept of barrier distributions and fluctuations of the fusion probability.

The Fusion Probability at The Fusion Barrier For spherical closed-shell nuclei (N = 50,82 and Z = 50), the onset of decreasing $p(E_B)$ values is found at $x_{thr} = 0.72$, as predicted by theory (134), whereas the fusion of soft nuclei with $56 < N < 64$ between Zr and Pd shows decreasing $p(E_B)$ values earlier, at $x_{thr} = 0.70$ (Figures 22 and 23*a*). A linear or even slightly stronger decrease with $x\text{-}x_{thr}$ is compatible with the data. For the heavier systems leading to transactinide elements, $p(E_B)$ values are deduced, assuming, since fission barriers beyond Rf are high, a constant or only slowly varying loss in the evaporation cascade (see Figures 23*b*). The onset of decreasing values of the fusion probability for actinide-based fusion starts for the reaction $^{22}Ne/^{238}U$ or $^{18}O/^{248}Cm$ at $x_{thr} = 0.71$, whereas the fusion using the closed-shell nuclei ^{208}Pb and ^{209}Bi in Pb/Bi-based fusion (as shown in Figures 22 and Figures 23) shows the onset at the larger value $x_{thr} = 0.79$ for the reaction $^{208}Pb/^{48}Ca$. The slope of the fusion probability as a function of x is found to be the same for all systems investigated. From the relation between effective fissility and atomic number, we obtain the slope constant of the Z-dependence of $p(E_B)$. We write

$$p(E_B) = 0.5 \exp[-\text{const}(Z - Z_{thr})], \qquad 16.$$

where the constant depends only on known macroscopicnuclear parameters. These

are parameters of the liquid-drop model, the specific isospin I of the compound system, the mass asymmetry of the collision system $\kappa = (A_1/A_2)1/3$, the weighting factor α for the effective fissility, the extra-push slope constant a, and the parameter c_1 from the experimentally established extra-push dependence of the barrier fluctuation. These parameters yield $p(E_B, Z + 1)/p(E_B, Z) = 3$–4, as observed experimentally.

The "Coulomb Falls" Figure 24 shows the mass asymmetry $\Delta = (A_2 - A_1)/(A_2 + A_1)$ of the collision system as a function of the atomic number Z of the fused element. An underlying grid of differences of $\Delta Z_{1,2} = 8$ of the

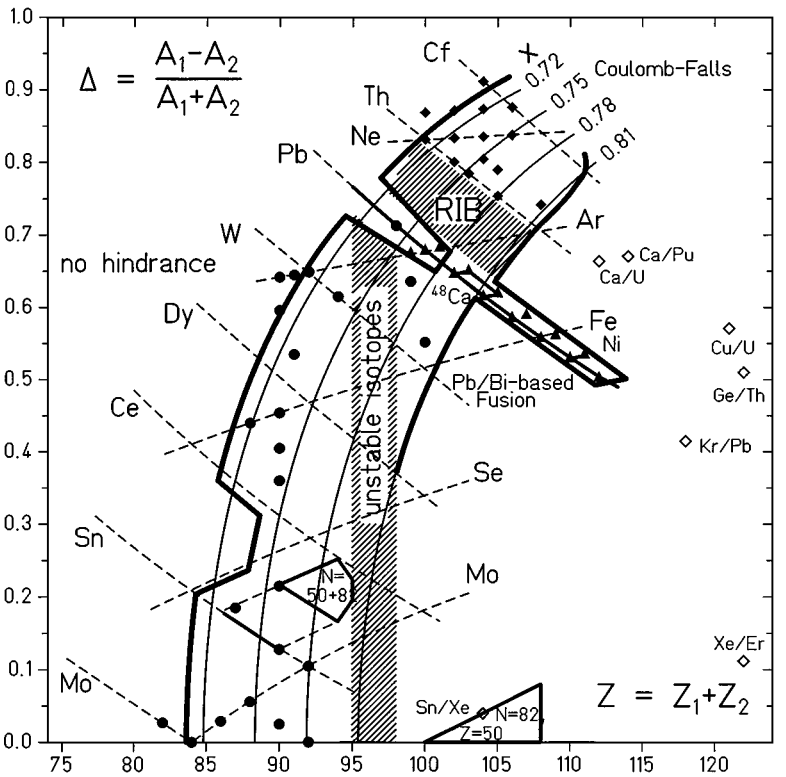

Figure 24 Asymmetry is plotted versus atomic number. Plot lines of constant effective fissility between x = 0.72 and x = 0.81 (solid lines) are shown on a grid of fusing elements represented by their most neutron-rich isotopes (hatched lines). The two heavy lines of starting entrance element limitation and of the 1-pb level of σ-values define the x-values of cross section breakdown ("Coulomb falls"). Between them the fusion probability at the Coulomb barrier decreases by a factor of 10^5. The solid symbols indicate successful fusion. The collision systems used in the 1999 experiments (73, 103–104a, 117) and early GSI experiments (157) are indicated by open symbols.

atomic numbers of the collision partners is indicated. The heaviest isotopes for each element are chosen to construct the grid. The effective fissility x with $\alpha = 1/3$ (Equation 12) fixed depends in good approximation on only two variables, the asymmetry (Δ) and the atomic number (Z), chosen for representation in Figure 24. The lines corresponding to $x = x_{thr}$ and $x = x_{thr} + 0.1$ are indicated. Within a range $\Delta x = 0.1$, the production cross section for a fixed heavy collision partner decreases by a factor of 10^5, and for heavy elements it reaches the 1-pb level. The macroscopic parameters, as discussed, impose on the amalgamating system the exponential decrease of the production cross section, which we call the "Coulomb falls." The goal of reaching a high atomic number is intrinsically frustrated by the increasing Coulomb repulsion introduced into the system by its production. Beyond $x = x_{thr}$, the decrease of the production cross section is universal. For symmetric and Pb/Bi-based fusion reactions this is well-confirmed; for actinide-based fusion there is good experimental evidence. For the production of transactinide elements ($Z \geq 104$), a decrease by a factor of 3.5 between element Z and element $(Z + 1)$ is established, as had been found before for symmetric systems (Figure 20). The ground-state properties of the fused system manifest themselves strongly in the deexcitation of the compound system. However, for the formation of the compound system, they seem to be irrelevant in the region of the Coulomb falls. The macroscopic nuclear surface and Coulomb forces rule the formation.

Theorists have made highly valuable advances in reaction models, but their predictive power is still far from that of nuclear structure calculations of the ground-state properties (presented in Section 2).

Nörenberg introduced the assumption of "dissipative diabatic dynamics" in order to include nuclear structure (143). It is based on the fact that in a collision, the barrier transit time (2.10^{-22} s) is small compared with the redistribution time of the paired nucleons in partly filled orbits ($2 \cdot 10^{-21}$ s). As levels are promoted in the collision to higher energies, energy provided from radial energy is dissipated. The model has been applied successfully to symmetric fusion (144).

In 1985, Volkov introduced the concept of a dinuclear system (DNS) (145). A dinuclear complex is formed in deep-inelastic reactions after dissipation of the kinetic collisional energy. Multiple transfers of nucleons between the collision partners at large distances drive toward an increasingly asymmetric system and produce a compound nucleus. This formation is discussed as a competition between quasi-fission and complete fusion. The concept was applied to symmetric collision systems in Reference 146. In recent years the model has been consolidated, and in the latest version of the DNS concept, cross sections for the production of SHEs are calculated including nuclear structure effects (147). The model does not predict formation of element 118 in the reaction $^{86}Kr/^{208}Pb$, whereas cross sections in the 1–10-pb range are predicted to produce elements 110 to 114 in the reactions of ^{232}Th, ^{238}U, ^{244}Pu with ^{48}Ca projectiles (148). Wada et al developed a dynamical model of fusion. A three-dimensional Langevin equation must be solved to treat dissipation and fluctuations in the entrance channel (149).

A one-dimensional model gives cross sections for the production of element 114 in the reaction ^{48}Ca/^{244}Pu of 10 pb (150). Denisov & Hofmann presented a first calculation of cross sections along similar lines (151).

5.3 Closed Shell Nuclei as Collision Partners—Nuclear Structure in the Entrance Channel

The only parameter found in our experiments that drastically changes the fusion probability at energies near the Coulomb barrier is the nuclear structure of the collision partners. When closed-shell nuclei such as ^{136}Xe or ^{208}Pb are used as partners, the onset of decreasing fusion probabilities is delayed. We discuss here the most prominent examples: the systems ^{86}Kr/^{136}Xe ($\Delta x = 0.03$) and ^{48}Ca/^{208}Pb ($\Delta x = 0.07$). For the ^{86}Kr/^{136}Xe system fusing to ^{222}Th, excitation functions were measured in 1996 at GSI in a collaboration with FLNR (152). The xn channels are shown in Figure 25. The 1n channel peaked, similar to the ^{208}Pb/Bi-based systems, at 15 MeV, an energy below the fusion barrier. It is not shifted by the fusion barrier to higher energies, as was observed in other symmetric systems for radiative capture (153) and 1n channels (128). The extracted extra-push values and the barrier fluctuation parameter are presented in Figure 22*a*,*b*.

For ^{208}Pb/Bi-based fusion reactions, the delay is equivalent to a shift by six elements. Entrance-channel hindrance starts not at $Z = 96$ but at $Z = 102$ for the ^{48}Ca/^{208}Pb reaction (see Figure 24). The values of the fusion probability presented in Figure 23*b* are lower limits. Γ_n/Γ_f is assumed to stay constant (see Figure 3*b*) and to contribute comparatively little to the falling cross sections. For the

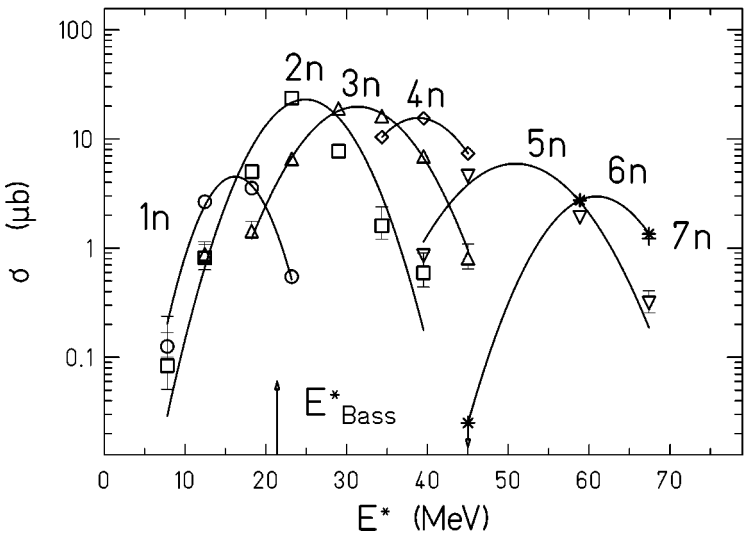

Figure 25 Cross sections observed for xn channels in the collision system ^{86}Kr/^{136}Xe (152) as a function of excitation energy.

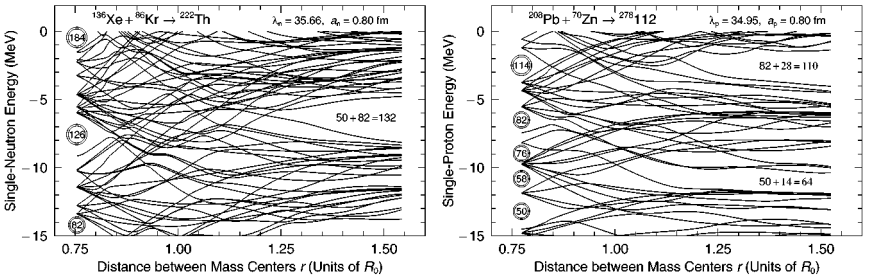

Figure 26 Single-particle levels for the two-center systems (*a*) $^{86}Kr/^{136}Xe$ and (*b*) $^{70}Zn/^{200}Pb$ as a function of R/R_0 where R_0 is the radius of the compound system (154). Gaps at $N = 50 + 82$ (*a*) and $Z = 28 + 82$ (*b*) are very prominent and disappear near the fission barrier exit points.

production of $^{277}112$, the value of the fusion probability derived from the 1n cross section is $3 \cdot 10^{-6}$ (see Table 5).

In the two-center level diagrams calculated by Möller et al (154), gaps in the level density are found at $N = 50 + 82$ (Figure 26*a*) and at $Z = 28 + 82$ (Figure 26*b*). Even after deep penetration, the closed-shell clusters ^{132}Sn and ^{208}Pb keep their identity and dissipative losses are avoided during a large part of the amalgamation process. In both level diagrams, the cluster configurations are maintained until the deformation is reduced to $R/R_0 = 1.15$, with R_0 the radius of the compound system. The 1n channels show their maximal cross sections at excitation energies of 12–15 MeV. These energies indicate temperatures of the intermediate systems of 0.7 MeV, well below the limit of 1.5 MeV, where shell corrections disappear. In the final stage, when $R = 0.75$–$1.15\ R_0$ and the gaps in the level diagrams for closed-shell nuclei have disappeared, dissipative dynamics of the macroscopic models and level crossings may be important. As is indicated by the steep decrease of cross sections and of the fusion probability, the increasing macroscopic forces, which govern the fissility, increasingly hinder the formation of EVRs in the cluster-supported reactions as well. The cluster velocities in this last stage of fusion are small and the excitation energy is restricted; both these conditions reduce dissipation. The underlying cluster may be excited but not destroyed. Nucleons of the open shells carry most of excitation energy and the clusters only a minor part. The available excitation energy of 12 MeV allows the nucleons of the light partner to occupy the empty orbits outside the cluster core and finally to achieve transmutation into an excited state of the nascent heavy nucleus.

In order to be protected against immediate reseparation, the system with 12 MeV excitation energy and a configuration close to the deformation of the protecting fission barrier has to cool down, by emission of a neutron, to an energy below the fission barrier. Since the macroscopic forces defined by the liquid-drop potential energy surface (PES) are repulsive in all stages of the collision, the system stays

TABLE 5 Cross section estimates for different fusion reactions giving access to superheavy elements. Estimates for the different contributions in Equation 7 as discussed in Section 5 are given

Reaction	X	$\pi\ell^2\lambda^2$	$p(E_{max})$	$\left(\frac{\Gamma_n}{\Gamma_f}\right)_{intr}$	$(K_{coll.enh.})^{-1}$	$\left(\frac{\Gamma_n}{\Gamma_f}\right)_{precomp}$	σ_{EVR}	Reference
$^{208}Pb(^{48}Ca,n)^{255}_{153}No$	0.79_3	12 mb	0.3	5×10^{-2}	—	1.5×10^{-3}	260 nb	113
$^{238}U(^{22}Ne,5n)^{255}_{153}No$	0.72	45 mb	0.2	7×10^{-6}	—	—	60 nb	best estimate
$^{208}Pb(^{70}Zn,n)^{277}_{167}112$	0.90_5	7 mb	3×10^{-6}	10^{-2}		5×10^{-3}	1 pb	11
$^{238}U(^{34}S,5n)^{267}_{159}Hs$	0.80	21 mb	1.5×10^{-5}	10^{-5}	—	—	2.5 pb	101
$^{208}Pb(^{76}Ge,n)^{283}_{169}114$	0.92_5	6 mb	6×10^{-7}	10^{-2}	—	5×10^{-3}	0.2 pb	very hard, perhaps
$^{244}Pu(^{36}S,5n)^{275}_{165}110$	0.81_3	12 mb	3×10^{-6}	10^{-5}	—	—	0.4 pb	hard, but possible
$^{232}Th(^{44}Ca,5n)^{271}_{161}110$	0.83_8	10 mb	10^{-6}	10^{-5}	—	—	0.1 pb	very hard, perhaps
$^{244}Pu(^{48}Ca,3n)^{289}_{175}114$	0.86_5	13 mb	5×10^{-8}	8×10^{-5}	$<10^{-2}$	—	<0.5 fb	beyond the limit
$^{208}Pb(^{86}Kr,n)^{293}_{175}118$	0.96_7	5 mb	2×10^{-8} 6×10^{-6}	10^{-2} (3×10^{-2})	0.2	5×10^{-3}	1 fb (1 pb)	beyond the limit 159a

between the ground state (0.85 R_0) and the saddle-point deformation (1.0 R_0) only for a short time, $\sim 2 \cdot 10^{-20}$ s. The neutron has to be emitted during this time. Mean neutron emission times at $E^* = 12$ MeV are estimated to be a few times 10^{-17} s (155). The emission probability in the time interval of $2 \cdot 10^{-20}$ s is $3 \cdot 10^{-3}$. With this factor the value of $\Gamma_n/\Gamma_f = 10^{-2}$ is reduced to $3 \cdot 10^{-5}$. This result gives for ^{48}Ca(^{208}Pb,n)^{255}No a cross section close to the experimentally observed value of 0.26 μb (see Section 5.1). It is this reduction of Γ_n/Γ_f by precompound emission that destroys the large advantage ($\sim 10^3$) in survival probability for 1n reactions as compared to actinide-based 4n and 5n reactions. The remaining advantage is small, about a factor of four. The two-stage formation process presented in Equation 7 breaks down at $x \geq 0.8$, and no equilibrated compound system can be formed. For the actinide-based reactions with up to five neutrons emitted, successful so far for $x < 0.8$, the two-stage picture is probably still valid. The same holds for the symmetric systems that have been investigated. The exception is the Pd/Pd system, in which precompound emission was discussed (120). In analogy to the one-step scenario described above, there may be a surprise for the $N = (50 + 82)$ systems. When combining heavier $N = 82$ targets, such as ^{138}Ba and ^{139}La, with heavier $N = 50$ projectiles, ^{87}Rb and ^{88}Sr, new light isotopes of the elements Np to Am with neutron numbers 129–131 might become accessible in the fissility range $x < 0.84$. If 1n channels prevail at $N = 131$ for these systems, this would be a strong indication that again a one-step process with precompound neutron emission takes over at the highest fissilities.

Support for the one-step scenario comes from the lack of observation of the capture channel in ^{208}Pb/Bi-based reactions. Deexcitation by high-energy γ-rays takes longer than the emission of a single fast neutron. In the short interval of $2 \cdot 10^{-20}$ s, γ-emission has no chance to stabilize the precompound system. There is a narrow window between the fission barrier and the one-neutron separation energy S_n, well investigated in n-capture reactions of fissionable nuclei as first-chance fission, where the competition between fission and γ-deexcitation is the dominant reaction mechanism. This mechanism was not found in the heavy-ion fusion reactions that have been used to synthesize transuranic elements. Its absence corroborates that the 1n reactions in fusion are not an analogue of a second-chance fission channel.

Figure 27 presents the sequence of stages for a collision system leading to element 112 at different distances of approach within the proposed scenario. The structure of the ^{208}Pb cluster is presumed to be preserved until a stage of deep penetration at $R = 1.15\ R_0$. In the following stage of closest approach, the nucleons of the ^{70}Zn projectile are transferred to empty states of the ^{208}Pb cluster. The combined precompound system at an excitation energy of 12 MeV then cools down by emission of a neutron, which carries away about 8–9 MeV and is emitted during the time span of closest approach. At the remaining excitation energy of about 3–4 MeV, the excited superheavy nucleus ^{277}112 is protected against prompt fission behind the fission barrier of the microscopically stabilized superheavy nucleus. It finally deexcites by a slow cascade of γ-rays and conversion electrons.

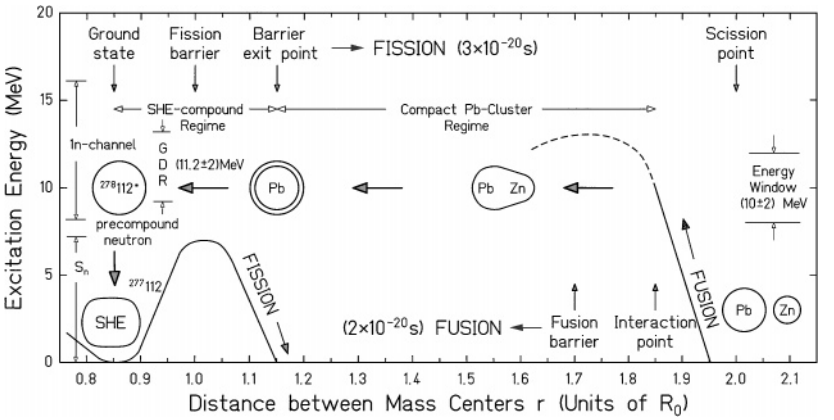

Figure 27 Stages corresponding to the fusion path toward element 112 for the ^{70}Zn/^{208}Pb collision system. The system moves from right to left.

The proposed fusion process is a one-step rearrangement process observed for 1n reactions, with a miniscule probability for central encounters.

6. PROSPECTS AND DREAMS

6.1 Fusion at Its Limits

The production of fusion EVRs has its limitations, as presented in Section 5. The dramatic breakdown of complete fusion, the Coulomb falls, is a general macroscopic phenomenon and its onset should be determined for all possible asymmetries of the collision systems. The heaviest combinations for the different heavy collision partners between Pd and Cf reaching the 1-pb limit of cross sections should be determined. The important question of the role of deformation of the heavy partner for the onset of entrance-channel hindrance can be investigated with actinide targets and also with lanthanide targets in the range Z = 64–72. The second region of cluster-based fusion at N = 50 + 82 = 132 should be consolidated and extended to EVRs of elements beyond Th.

Other limitations concern the deexcitation mechanisms of the compound system. More data on heavy-ion capture are needed to corroborate that the width for the γ-deexcitation channel, Γ_γ, is of no relevance for heavy-element synthesis. The energy spectrum of the neutrons emitted in 1n channels compared to higher-xn channels may support the existence of a one-step fusion mechanism that might profit from higher neutron energies. The fission width Γ_f is very different for deformed and spherical nuclei. Collective enhancement of level densities in the shell N = 126 disappears as one goes away from the shell. The behavior at neutron numbers N < 126 is not known at all, since all available data concern N > 126. In the region 170 < N < 184, increased fission losses are expected in the

production of SHEs. Shell corrections of the fission barrier vanish at a much smaller energy for spherical nuclei than is predicted by theory. Thus, more data on the temperature dependence of the fission losses are needed.

In the Coulomb falls, the reaction flux moves from fusion toward quasi-fission and transfer reactions. Binary reactions at the Coulomb barrier in and beyond the Coulomb falls may give access to new channels in the reaction flux. Whether there is still a chance to find fusion-like reactions beyond the limit of the Coulomb falls depends on exactly such new reaction physics, which might initially be revealed in binary reactions. Without new efforts in reaction physics at the Coulomb barrier preparing the ground, heavy-element synthesis efforts will slowly suffocate.

6.2 New Elements and Isotopes in the "Coulomb Falls"

Accepting the dramatic loss of cross section in the Coulomb falls, we can exploit cross sections within this limit and the limits set by the experimental methods of $\sigma > 0.1$ pb to search for new isotopes and elements. Figure 28 shows a chart of nuclides of the known nuclei for Z = 106–113, and the still unknown isotopes with the collision partners proposed for their production. Out of 58 isotopes shown, only 22 have been synthesized to date. Of the isotopes still to be synthesized, 14 are proposed to be made by Pb/Bi-based reactions and 22 by actinide-based reactions. More than 60% of the accessible isotopes are work for the future.

The heavy actinide targets ^{254}Es, ^{249}Cf, ^{249}Bk, ^{248}Cm, and ^{244}Pu combined with ^{18}O, ^{22}Ne, ^{26}Mg, ^{27}Al, and ^{36}S projectiles promise the best production rates for actinide-based reactions. The highest element accessible within $\sigma > 0.1$ pb is element 111, produced by ^{24,26}Mg on ^{254}Es. N = 166 is reached with the isotope ^{276}110 synthesized by ^{36}S on ^{244}Pu. This reaction will also give the heaviest isotopes of Hs and Sg. For example, ^{268}Sg is a chain member on the N = 162-shell. The N = 162 shell is accessible directly from Hs to Z = 111. The long-lived isotopes at N = 160–162 open the field for chemistry experiments up to Mt.

The Pb/Bi-based reactions, besides ^{208}Pb and ^{209}Bi, need the target ^{207}Pb bombarded with the neutron-rich projectiles between ^{62}Ni and ^{76}Ge. With ^{207}Pb-targets, the challenge is to find eight e-e isotopes in chains starting from e-e isotopes of elements 110 and 112 and covering the isospin values T_z = 24, 25, 26. The T_z = 26 chain starting with ^{276}112 passes the N = 162 shell. The chances of finding all the necessary α-bridges at ^{256,258,260}Rf are good but require a special effort. The α-energies connect the region of superheavy deformed isotopes around ^{270}Hs to the masses of known isotopes. There is no better way to determine a closed shell than by the measurement of mass excesses. The existence of deformed barrel-like ($\varepsilon_4 > 0$) SHEs was until now the most rewarding discovery for experiments and theory, and the measured shell strength would be a stringent test of the microscopic theory.

In-beam γ-spectroscopy of transactinide isotopes is within reach. In the reaction ^{208}Pb (^{48}Ca,2n), the isotope ^{254}No is produced with $\sigma = 2.2$ μb. Two experiments combining recoil spectrometers and large γ-detector arrays succeeded

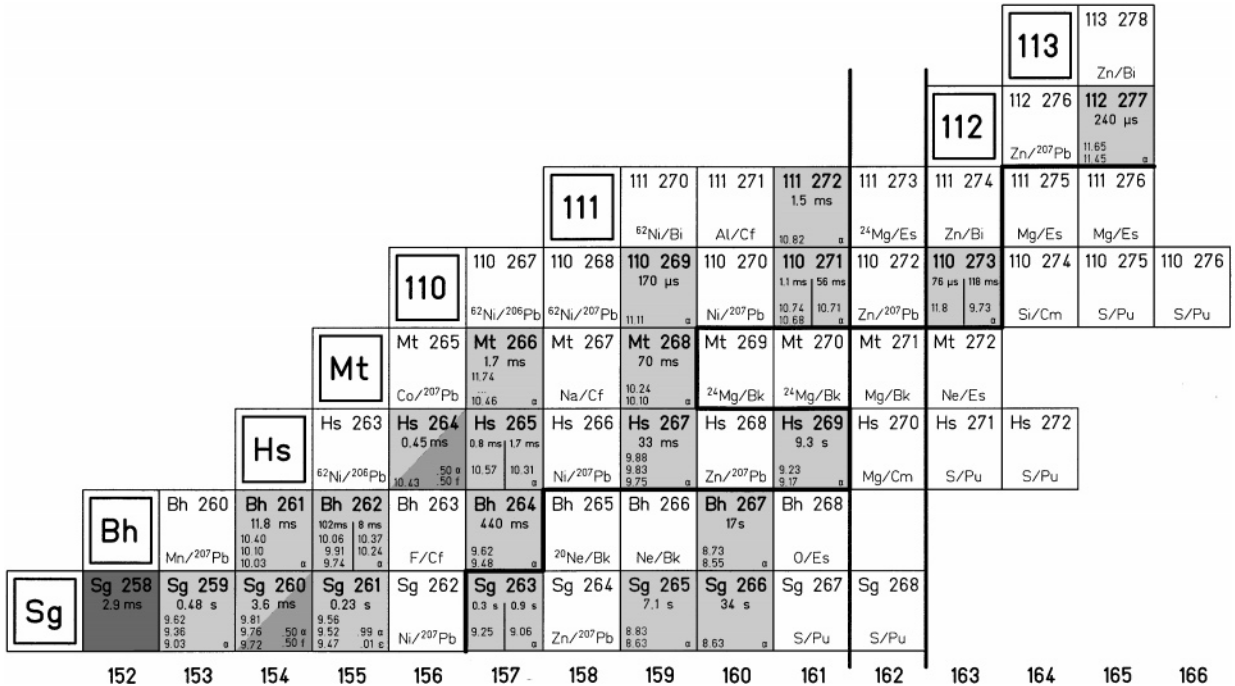

Figure 28 The isotopes of elements 106 to 113 accessible above the α-level of 0.1 pb. The known isotopes are listed. Shading indicates spontaneous fission and half-shading indicates α-decay. The recommended collision systems for the elements and isotopes not yet synthesized are indicated in the blank boxes.

in observing the ground-state band of ^{254}No up to spins I = 14 (156) and I = 16 (157). ^{254}No is found to be a good rotor, with a β_2-value of 0.27 ± 0.02. Its first 2^+ state at 44 keV is in good agreement with a predicted value of 42.4 keV. Up to I = 16 and E^x = 6.2 MeV the nucleus ^{254}No is still not destroyed by fission. The production of transactinides certainly has smaller cross sections, but the new technique is still full of possible improvements. It will open the field of nuclear structure studies of the heaviest elements, and we will learn how high spin values and excitation energies reduce the fission barrier and increase the Γ_f values.

With ^{76}Ge beams on ^{208}Pb targets, there is a good chance to synthesize $^{283}_{169}$114, which is a deformed nucleus that decays via longer-lived unknown isotopes to the known ^{259}No isotope. The correlation over a range of 12 elements to the region of known isotopes requires major improvements to SHIP. Via the connection to the known isotope ^{259}No, element 114 can be identified unambiguously for light isotopes ($T_z < 28$) produced by Pb/Bi-based reactions. With the actinide-based reaction ^{36}S/^{244}Pu, the same decay chain, but starting with ^{275}110, can be populated. Both experiments are equally difficult, but it would be a pleasure to unite the so-called hot- and cold-fusion efforts on an isotope of element 114 that is connected to the known world of nuclides.

Table 5 gives cross section estimates and the different contributions to Equation 7 for some of the reactions of interest.

6.3 Search Beyond All Limits

In the first enthusiasm about the possible production of SHEs in 1966, a limit on fusion was not foreseen. All nuclei amalgamated with each other, and the periodic system of elements was open up to Z = 188, an element which was hoped to be made by fusion of ^{238}U and ^{248}Cm, and which was expected to emit positrons. The promised land was in front of us, and atomic weight 500 was within reach.

It took 20 years to understand that production by fusion was the limiting factor, rather than the stability of nuclei in the ground state. The question to be answered was why the number of elements is limited, and it was accepted that the atomic number of the final highest element is of minor importance. Step by step we found our way to element 112 by fusing shell-stabilized collision partners, the N = 40 nucleus ^{70}Zn with the doubly closed-shell nucleus ^{208}Pb, to produce a superheavy nucleus stabilized by an unforeseen nuclear structure of its own. The bombarding energy had to be fixed within 2 MeV, and the energy was just enough to emit a neutron at a well-defined time in order to stabilize the formed nucleus behind its fission barrier. Each new element was a masterpiece of creation.

Since 1999 times have changed again. For part of the community, jumping beyond the limits directly to the promised land is the new dream. Fantastic reports were given: Z = 114 with three isotopes and six new isotopes of lighter elements synthesized at FLNR (73, 103–104a), Z = 118 by chains of seven new isotopes at LBL (117). Three new elements and 15 new isotopes beyond Sg within six months, the same number that the GSI craftsmen managed to forge within 15 years. SHEs are en vogue again. However, experimental results can be accepted by the scientific

community only when they are reproduced. We are looking forward to this final quality test in the near future. Until then, my attitude toward the 1999 experiments is skeptical.

In actinide-based reactions aiming at high atomic numbers, the systems $^{18}O/^{249}Cf$, ^{22}Ne on ^{249}Bk, ^{248}Cm, and ^{244}Pu; $^{34}S/^{238}U$, and $^{31}P/^{232}Th$, giving isotopes of elements 104 to 108, are the leading combinations that have been applied with success in 4n and 5n channels. In the FNLR experiments, ^{48}Ca beams bombarded ^{238}U and ^{244}Pu. No intermediate system was investigated between the previously established combinations and the ^{48}Ca-induced reactions, which lead far beyond the limits of the Coulomb falls (see Figure 24). The sole effort with an intermediate system, the $^{34}S/^{244}Pu$ experiment discussed in Section 4.3, was not encouraging. Irradiating actinides produces spontaneously fissioning isotopes. Fission events were selected in the FNLR experiments, and their reconstructed prehistory provided the published sequences. Since these time-reversed correlations end with fission, no isotope will be linked to a known isotope. The isotopes that are produced lie beyond the limits of known isotopes, and there they will stay. To prove where the fission events came from is very difficult. The energy liberated as total kinetic energy (TKE) in fission can be measured for single events. A FLNR paper described how to do this (103). The TKE values of the five fission events selected and assigned to superheavy isotopes give a mean energy of 190 ± 10 MeV (104). For the one chain assigned to $^{289}114$ and proposed to end by spontaneous fission of Hs, the expected TKE value is 220 MeV (73). For the four experimental events assigned to $Z = 112$, it is 235 MeV (103, 104). The measured value of 190 MeV is too low for a SHE. It points to lighter elements between Cm and No. The TKE measurement cannot support an assignment of the observed fission events to a SHE. The sequences were selected by *assuming* that the fission events were produced by fusion, and thus they are assigned to superheavy isotopes by definition. Moreover, preceding α-energies fit theoretical expectations well. In the earlier case of the $^{34}S/^{244}Pu$ experiment (72), the dead end of chain selection by criteria taken from outside the proper experimental data was introduced, and it reappears in the 1999 experiments. I have critiqued these experiments and data analysis elsewhere (81). The importance of the claimed discovery makes extensive documentation or open access to the data base of the experiments essential, and neither is available. Concerns center on use of continuous beams, selection and reconstruction of chains based on fission events, suppression of accidentals, longest possible correlation times, and calculation of random probabilities. However, the most serious objection centers on the courageous jump from $^{267}_{159}Hs$ to $^{283}_{171}112$ and $^{289}_{175}114$ into a region of spherical nuclei far beyond the limits of assured production. The limitation by hindrance in the entrance channel for actinide-based reactions had already become evident in 1995 when ^{267}Hs was produced (101). All experiments since then aiming at elements 110, 112, and 114 show cross sections in the range 0.3–3 pb, which stay constant at this level. To explain this finding, the following arguments were put forward: The 3n channels expected for ^{48}Ca induced reactions give reduced losses in the deexcitation phase of the reaction, compared with 5n channels; and the landing sites are closer to the spherical shells

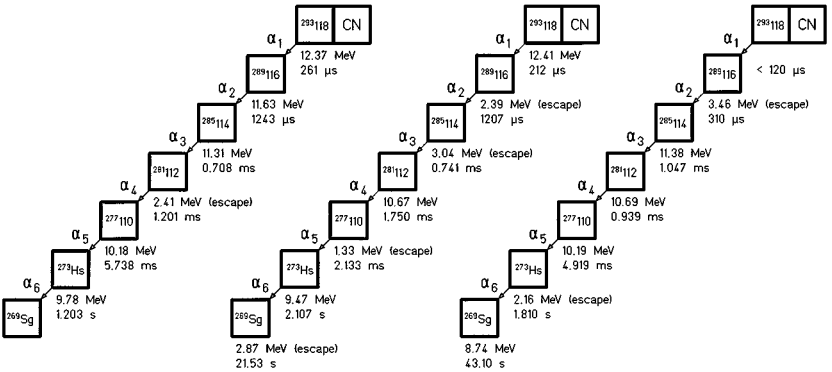

Figure 29 Three sequences observed in the reaction of 449 MeV ^{86}Kr with ^{208}Pb assigned to ^{293}118 (117).

$Z = 114$ and $N = 184$, where larger fission barriers are predicted. However, the gain going from 5n to 3n channels is only an order of magnitude in cross section, the $Z = 114$ shell has disappeared, and $N = 184$ is still nine neutrons away even in the best case. Whether the shell corrections of the fission barriers are increased compared with ^{267}Hs is questionable.

If one takes the argument of low excitation energy seriously, one should use an even higher projectile mass. This was done at GSI in 1977 without success, bombarding ^{238}U with ^{65}Cu projectiles (158). The change of the reaction mechanism in the Coulomb falls is a hard fact, and spherical closed-shell nuclei do not like to be heated much. To ignore these facts and hope to synthesize new elements will require new physics. It will take the community years to confirm or disprove the FNLR experiments showing single short sequences.

The experiment ^{86}Kr on ^{208}Pb at LBL gave three sequences of signals with seven generations, which were attributed to ^{293}118 produced via a 1n channel (see Figure 29). A production cross section of $(2.2\,^{+2.6}_{-0.8})$ pb was published, and α-energies and half-lives were assigned to the $T_z = 57/2$ chain starting with $^{293}_{175}$118 and ending with $^{269}_{163}$Sg , all new nuclides (117). A spontaneous-fission event ending the chain in one of the following two generations is expected but was not reported. This experiment, in jumping from $^{277}_{165}$112 to $^{293}_{175}$118, also goes beyond the limits of production and produces a spherical nucleus close to the ^{292}120 shell closure. The arguments put forward against the FNLR experiment also hold here. The assignment to $Z = 118$ was based on the assumption that a fusion reaction in a 1n channel produced the observed sequence. The decay chain followed predicted α-energies and half-lives. But these are arguments taken from outside the measured data. On the other hand, the higher shell corrections very close to ^{292}120 give larger fission barriers and reduce the losses in the deexcitation phase, as was argued for $N = 184$ in Reference 159. ^{86}Kr is a $N = 50$ nucleus and the closed shell delays the hindrance in the entrance channel, as observed in Reference 152. The macroscopic fusion barrier for the collision system is lower than the inner microscopic barrier

(159a, 160). The system is free to penetrate deeply, and may indeed fall with a highly reduced hindrance in the entrance channel directly, with $\Gamma_n/\Gamma_f \sim 1$, into a safe state behind the fission barrier. This picture is not far from the one proposed in Section 5.3.

Whether new physics can raise the cross section by a factor of 10^3 and guarantee a soft landing on a rock in the Coulomb falls is open to speculation. The numbers in brackets for the ^{86}Kr/^{208}Pb reaction in Table 5 are estimates for reaching the pb range. The LBL experiment was repeated at the same excitation energy at GSI, but no chain was found (161), with an upper limit of 1 pb at a dose slightly higher than that applied at LBL. At LBL a continuous beam was used, at GSI a discontinuous irradiation cycle. Since all half-lives presented in the three sequences are short, between 0.15 μs and 3.0 s, accidental correlations can be excluded. The correlation times manifestly must fulfill the statistics given by an exponential decay, and external disturbances, having a different correlation time distribution from radioactive decay, can easily be eliminated. The reproducibility of the LBL experiment will be resolved very soon, since LBL will repeat the experiment this year.

Whatever the future brings, the three sequences shown in Figure 29 have been observed and must be understood. They are not shown here to announce element 118 but to demonstrate that even highly complex sequences do not necessarily prove a new element. If I should be wrong, I apologize. The glory will be with those who make dreams a reality.

ACKNOWLEDGMENTS

The work presented was done by many people over many years. I have the privilege of knowing most of them at the end of my 25 years' involvement in our common cause. I thank all whose work allowed these pages to be written. In particular, I want to mention longstanding help from discussions on theory with P Moeller, W Noerenberg, A Sobiczewski, and W Swiatecki. For the experiments on SHEs, my special thanks go to G Muenzenberg, S Hofmann, FP Heßberger, and V Ninov, the longstanding members of the SHIP group. The experiments on fusion mechanisms of heavy nuclei would not be what they became without the contributions of KH Schmidt. The figures were edited by E Pfeng and the manuscript received the help of S Luettges, who finally brought this review close to publication.

LITERATURE CITED

1. Becquerel H. *Compt. Rend.* 122:420 (1896)
2. Hofmann S, Münzenberg G. *Rev. Mod. Phys.* 72:In press (2000)
3. Armbruster P. *Annu. Rev. Nucl. Part. Sci.* 35:135 (1985)
4. Oganessian YT, Iljinov AS, Demin AG, Tretyakova SP. *Nucl. Phys.* A239:353 (1975)
5. Münzenberg G, et al. *Z. Phys. A* 300:107 (1981)

6. Münzenberg G, et al. *Z. Phys. A* 309:89 (1982)
7. Münzenberg G, et al. *Z. Phys. A* 315:145 (1984)
8. Münzenberg G, et al. *Z. Phys. A* 317:235 (1984)
9. Hofmann S, et al. *Z. Phys. A* 350:277 (1995)
10. Hofmann S, et al. *Z. Phys. A* 350:281–83 (1995)
11. Hofmann S, et al. *Z. Phys. A* 354:229 (1996)
12. Bohr N, Wheeler JA. *Phys. Rev.* 56:426 (1939)
13. Goeppert-Mayer M. *Phys. Rev.* 74:235 (1948)
14. Haxel O, Jensen HD, Suess H. *Phys. Rev.* 75L:1766 (1949)
15. Swiatecki WJ. *Phys. Rev.* 100:937 (1955)
16. Polikanov S, et al. *Sov. Phys. JETP* 15:1016 (1962)
17. Myers WD, Swiatecki WJ. *Nucl. Phys.* 81:1 (1966)
18. Strutinski V. *Nucl. Phys.* A95:420 (1967)
19. Schmidt K-H, et al. In *Physics and Chemistry of Fission, Jülich, 1979,* 1:409. Vienna: IAEA (1980)
20. Hessberger FP, et al. *Z. Phys. A* 321:317 (1985)
21. Münzenberg G, et al. *Z. Phys. A* 322:277 (1985)
22. Münzenberg G, et al. *Z. Phys. A* 324:489 (1986)
23. Möller P, Nix JR. *At. Data Nucl. Data Tables* 26:165 (1981)
24. Armbruster PJ. *"Enrico Fermi" School, Varenna 1984,* 91:222. Amsterdam: North-Holland (1986)
25. Patyk Z, Sobiczewski A, Armbruster P, Schmidt K-H. *Nucl. Phys.* A491:267 (1989)
26. Möller P, Nix JR. *Proc. Int. Conf. Phys. Chem. Fission, Rochester 1973,* 1:103. Vienna: IAEA (1974)
27. Böning K, Patyk Z, Sobiczewski A, Cwiok S. *Z. Phys. A* 325:479 (1986)
28. Smolanczuk R, Skalski J, Sobiczewski *A. Phys. Rev. C* 52:1871 (1995)
29. Smolanczuk R. *Phys. Rev. C* 56:812 (1997)
30. Möller P, Nix JR. *At. Data Nucl. Data Tables* 59:185 (1995)
31. Vautherin D, Véneroni M, Brink DM. *Phys. Lett.* B33:381 (1970)
32. Quentin P, Flocard H. *Annu. Rev. Nucl. Part. Sci.* 28:523 (1978)
33. Tondeur F. *Z. Phys. A* 297:61 (1980)
34. Dechargé J, Gogny D. *Phys. Rev. C* 21:1568 (1980)
35. Reinhard PG. *Rep. Prog. Phys.* 52:439 (1989)
36. Schmidt K-H, Vermeulen D. In *AMCO-6,* ed. JA Nolen, W Benenson, p. 119. New York: Plenum (1980)
37. Zeldes N, Dumitrescu TS, Köhler HS. *Nucl. Phys.* A399:11 (1983)
38. Skyrme THR. *Nucl. Phys.* 9:635 (1959)
39. Cwiok S, et al. *Nucl. Phys.* A611:211 (1996)
40. Rutz K, et al. *Phys. Rev. C* 56:238 (1997)
41. Bender M, et al. *Phys. Rev. C* 6003:4304 (1999)
42. Ring P. *Prog. Part. Nucl. Phys.* 37:193 (1996)
43. Dürr HP. *Phys. Rev.* 103:469 (1956)
44. Dechargé J, Berger JF, Dietrich K, Weiss MS. *Phys. Lett.* B451:275 (1999)
45. Schädel M. *Radiochim. Acta* 70/71:207 (1995)
46. Folger H. *Nucl. Instrum. Methods A* 438:131 (1999)
47. Gregorich KE, et al. *Radiochim. Acta* 43:223 (1988)
48. Schädel M, et al. *Radiochim. Acta* 48:171 (1989)
49. Gäggeler HW, Jost DT, Kovacs J, Scherer UW. *Radiochim. Acta* 57:93 (1992)
50. Münzenberg G, Faust W, Hofmann S, Armbruster PJ. *Nucl. Instrum. Methods* 161:65 (1979)
51. Yeremin AV, et al. *Nucl. Instrum. Methods* A 274:528 (1989)
52. Lazarev YA, et al. *Proc. Int. School-Semin.*

Heavy Ion Phys., Dubna, 1993, 2:497 (1993), *JINR-Rep. E7-93-274*
53. Ninov V, Gregorich KE, McGrath CA. In *ENAM98, AIP Conf. Proc., Woodbury*, ed. BM Sherrill, DJ Morrisey, CN Davids, 455:704 (1999)
54. Kratz JV. In *Heavy Elements and Related New Phenomena*, ed. PK Gupta, W Greiner, p. 129. Singapore: World Sci. (1999)
55. Ninov V, et al. *Nucl. Instrum. Methods A* 357:486 (1995)
56. Münzenberg G. *Int. J. Mass Spectrosc. Ion Phys.* 14:363 (1974)
57. Ewald H, et al. *Nucl. Instrum. Methods* 139:223 (1976)
58. Faust W, et al. *Nucl. Instrum. Methods* 166:397 (1979)
59. Davids CN, et al. *Nucl. Instrum. Methods B* 70:358 (1992)
60. Saro SR, et al. *Nucl. Instrum. Methods A* 381:520 (1996)
61. Reisdorf W, et al. *Nucl. Phys.* A444:154 (1985)
62. Schmidt K-H, et al. *Nucl. Phys.* A318:253 (1979)
63. Hofmann S, et al. *Z. Phys. A* 291:53 (1979)
64. Cohen BL, Fulmer CB. *Nucl. Phys.* 6:547 (1958)
65. Armbruster PJ. *Nukleonik* 3:183 (1961)
66. Armbruster PJ. *Z. Phys.* 166:341 (1962)
67. Paul M, et al. *Nucl. Instrum. Methods A* 277:418 (1989)
68. Baccho I, et al. *JINR-Rep. P13-4453, Dubna* (1969)
69. Ghiorso A, et al. *Nucl. Instrum. Methods A* 269:192 (1988)
70. Miyatake H, et al. *Nucl. Instrum. Methods B* 26:309 (1987)
71. Leino ME, et al. *Nucl. Instrum. Methods B* 99:653 (1995)
72. Lazarev YA, et al. *Phys. Rev. C* 54:620 (1996)
73. Oganessian YT, et al. *Phys. Rev. Lett.* 83:3154 (1999)
74. Armbruster PJ, et al. *Phys. Rev. Lett.* 54:406 (1985)
75. Gäggeler HW, et al. *Phys. Rev. C* 33:1983 (1986)
76. Agarwal YK, et al. *GSI-Rep., Darmstadt* 1:79 (1984)
77. Töke J, et al. *Nucl. Phys. A* 440:327 (1985)
78. Shen WQ, et al. *Phys. Rev. C* 36:115 (1987)
79. Türler A, et al. *Phys. Rev. C* 46:1364 (1992)
80. Münzenberg G. *Rep. Progr. Phys.* 51:57-104 (1988)
81. Armbruster PJ. *Eur. Phys. J. A* 7:23 (2000)
82. Schmidt K-H, Sahm CC, Pielenz K, Clerc HG. *Z. Phys. A* 316:19 (1984)
83. Ghiorso A, et al. *Phys. Rev. Lett.* 33:1490 (1974)
84. Hoffman DC, et al. *Phys. Rev. C* 31:1763 (1985)
85. Kratz JV, et al. *Phys. Rev. C* 33:504 (1986)
86. Lee DM, et al. *Phys. Rev. C* 25:286 (1982)
87. Buklanov GV, et al. *JINR-Rep. P7-83-91, Dubna* (1983)
88. Kratz JV, et al. *Phys. Rev. C* 45:1064 (1992)
89. Eichler R, et al. *Labor für Radio- und Umweltchemie Annu. Rep.* 1999:3 (2000)
90. Wilk PA, et al. *Labor für Radio- und Umweltchemie Annu. Rep.* 1999:4 (2000)
91. Schädel M, et al. *Nature* 388:55 (1997)
92. Andreyev AN, et al. *Z. Phys A* 345:389 (1993)
93. Andreyev AN, et al. *Z. Phys. A* 344:225 (1992)
94. Druin VA, et al. *At. Energiya* 22:127 (1966)
95. Lazarev YA. In *Extremes of Nuclear Structure*, ed. H Feldmeier, J Knoll, W Nörenberg (1996)
96. Lazarev YA, et al. *Phys. Rev. Lett.* 73:624 (1994)
97. Lane MR, et al. *Phys. Rev. C* 53:2893 (1996)
98. Türler A, et al. *Phys. Rev. C* 57:1648 (1998)
99. Somerville LP, et al. *Phys. Rev. C* 31:1801 (1985)

100. Demin AG, Tretyakova SP, Utyonkov VK, Shirokovsky IVZ. *Z. Phys. A* 315:197 (1984)
101. Lazarev YA, et al. *Phys. Rev. Lett.* 75:1903 (1995)
102. Hofmann S. *GSI-Nachrichten Darmstadt* 02-95:4 (1995)
103. Oganessian YT, et al. *Eur. Phys. J. A* 5:63 (1999)
104. Oganessian YT, et al. *Nature* 400:242 (1999)
104a. Oganessian YT, et al. *Phys. Rev. C* In press (2000)
105. Heßberger FB, et al. *Z. Phys. A* 359:415 (1997)
106. Hessberger FP, et al. *Eur. Phys. J. A.* In press (2000)
107. Hessberger FP, et al. CP425, *Tours Symp. Nucl. Phys. III*, ed. M Arnould, et al. AIP, 1-56396-749:3 (1998)
108. Ghiorso A, et al. *Phys. Rev C* 51:R2293 (1995)
109. Audi G, Wapstra AH. *Nucl. Phys. A* 565:1 (1993)
110. Myers WD, Swiatecki WJ. *Nucl. Phys. A* 601:141 (1996)
111. Bass R. *Phys. Rev. Lett.* 39:265 (1977)
112. Ghiorso A, et al. *Phys. Rev. Lett.* 24:1498 (1970)
113. Gäggeler HW, et al. *Nucl. Phys. A* 502:C561 (1989)
114. Hofmann S, et al. *Z. Phys. A* 358:377 (1997)
115. Bernas M, et al. *Phys. Lett. B* 113:279 (1983)
116. Hofmann S, et al. *GSI-Rep. Darmstadt* 99-1:7 (1999)
117. Ninov V, et al. *Phys. Rev. Lett.* 83:1104 (1999)
118. Reisdorf W. *Z. Phys. A* 300:227 (1981)
119. Reisdorf W, Schädel M. *Z. Phys. A* 343:47 (1992)
120. Schmidt K-H, Morawek W. *Rep. Progr. Phys.* 54:949 (1991)
121. Armbruster PJ. *"Enrico Fermi" School, Varenna, 1987*, 103:282. Amsterdam: North-Holland (1989)
122. Vandenbosch R, Huizenga JR. *Nuclear Fission.* New York: Academic (1973)
123. Andreyev AN, Bogdanov DD, Chepigin VI, Kabachenko AP. In *Heavy-Ion Fusion*, p. 260. Singapore: World Sci. (1994)
124. Ignatyuk AV, et al. *Sov. J. Nucl. Phys.* 21:612 (1975)
125. Junghans A, et al. *Nucl. Phys. A* 629:635 (1998)
126. Sikkeland T, Maly D, Lebeck DF. *Phys. Rev.* 169:1000 (1968)
127. Vermeulen D, et al. *Z. Phys. A* 318:157 (1984)
128. Sahm C-C, et al. *Nucl. Phys. A* 44:316 (1985)
129. Heinz A, Schmidt K-H, Junghans AR, Armbruster PJ. *GSI-Rep. Darmstadt* 99-1:32 (1999); *Spaltwahrscheinlichkeiten exotischer kerne.* Thesis. TU Darmstadt (1998)
130. Ericson T. *Nucl. Phys.* 6:62 (1958)
131. Bjørnholm S, Bohr A, Mottelson BR. *Proc. Int. Conf. Phys. Chem. Fission, Rochester*, 1:367. Vienna: IAEA (1974)
132. Nörenberg W. In *Heavy Ion Fusion*, p. 248. Singapore: World Sci. (1994)
133. Armbruster PJ. *Rep. Prog. Phys.* 62:465 (1999)
134. Swiatecki WJ. *Phys. Scr.* 24:113 (1981)
135. Blocki J, Feldmayer H, Swiatecki WJ. *Nucl. Phys. A* 459:145 (1986)
136. Quint B, et al. *Z. Phys. A* 346:119 (1993)
137. Bass R. *Nucl. Phys. A* 231:141 (1974)
138. Sierk AJ, Nix JR. *Proc. Int. Conf. Phys. Chem. Fission, Rochester*, 2:273. Vienna: IAEA (1974)
139. Davies KTR, Sierk AJ, Nix JR. *Phys. Rev. C* 31:915 (1985)
140. Fröbrich P, Gontchar II. *Phys. Rep.* 292:131 (1998)
141. Aguiar CE, Barbosa VC, Donangelo R. *Nucl. Phys.* A517:205 (1990)
142. Blocki J, Skalski J, Swiatecki WJ. *Nucl. Phys.* A618:1 (1997)
143. Nörenberg W. *Phys. Lett.* B104:107 (1981)

144. Berdichevski D, Lukasiak A, Nörenberg W, Rozmej P. *Nucl. Phys.* A499:609 (1989)
145. Volkov VV. In *Nucleus-Nucleus Collisions II, Visby*, 1:54. Amsterdam: North Holland (1985)
146. Antonenko NV, et al. *Phys. Lett.* B319:425 (1993)
147. Adamian GG, Antonenko NV, Scheid W, Volkov VV. *Nucl. Phys.* A633:409 (1998)
148. Cherepanov EA, Volkov VV. *Int. Conf. Phys. Chem. Transactinide Elements, 1st, Seeheim Contr. O-30* (1999)
149. Wada T, et al. *Nucl. Phys.* A616:C446 (1997)
150. Wada T, et al. *Int. Conf. Phys. Chem. Transactinide Elements, 1st, Seeheim Contr. P-W-33* (1999)
151. Denisov VY, Hofmann S. *Int. Conf. Phys. Chem. Transactinide Elements, 1st, Seeheim Contr. P-W-37* (1999)
152. Oganessian YT, et al. *Annu. Rep. 1995/96 JINR-FLNR Dubna:62 (1997); Etude expérimentale de l'influence de la structure des partenaires dans la fusion de systèmes presque symétriques.* Thesis. Univ. Caen (1998)
153. Keller JG, et al. *Nucl. Phys. A* 452:173 (1986)
154. Möller P, et al. *Z. Phys.* A359:251 (1997)
155. Hilscher D, Rossner H. *Ann. Phys.* 17:471 (1992)
156. Reiter P, et al. *Phys. Rev. Lett.* 82:809 (1999)
157. Leino M, et al. *Eur. Phys. J. A* 6:63 (1999)
158. Münzenberg G, et al. *GSI-Rep. Darmstadt* 1978-J1:75 (1978)
159. Smolanczuk R. *Phys. Rev. C* 59:2634 (1999)
159a. Myers WD, Swiatecki WJ. *Phys. Rev. C* In press (2000)
160. Möller P, Armbruster PJ, Hofmann S, Münzenberg G. In *ENAM98, AIP Conf. Proc., Woodbury*, ed. BM Sherrill, DJ Morrissey, CN Davids, 455:698 (1999)
161. Hofmann S, et al. 698 *GSI-Rep. 2000*-1 *Darmstadt*, 7 (2000)
162. Dressler R, Türler A, Gäggeler HW, Taut S. *Labor für Radio- und Umweltchemie Ann. Rep. 1999*, p. 6 (2000)
163. Gäggeler HW, et al. *Int. Conf. Phys. Chem. Transactinide Elements, 1st, Seeheim Contr. O-34* (1999)
164. LeNaour C, Trubert D, Hussonnois M, Brillard L. *Int. Conf. Phys. Chem. Transactinide Elements, 1st, Seeheim Contr. O-12* (1999)
165. Dressler R, et al. *Phys. Rev. C* 59:3433 (1999)
166. Dressler R, et al. *Labor für Radio- und Umweltchemie Ann. Rep.* 1999:5 (2000)

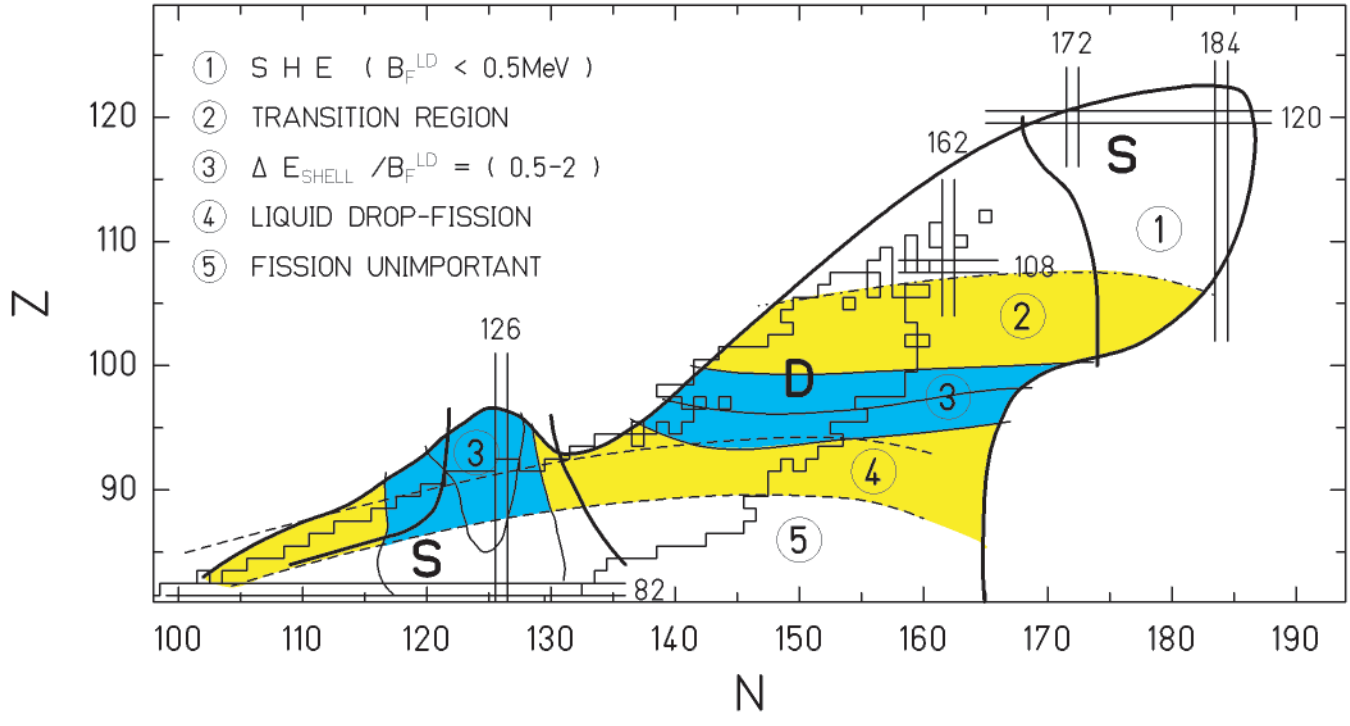

Figure 2 The region of shell-stabilized nuclei may be divided in five subregions defined by the ratio of the height of the shell-correction energies to the macroscopic fission barriers. Regions of spherical (S) and deformed (D) nuclei, shells and subshells between ^{208}Pb and ^{304}120 are indicated.

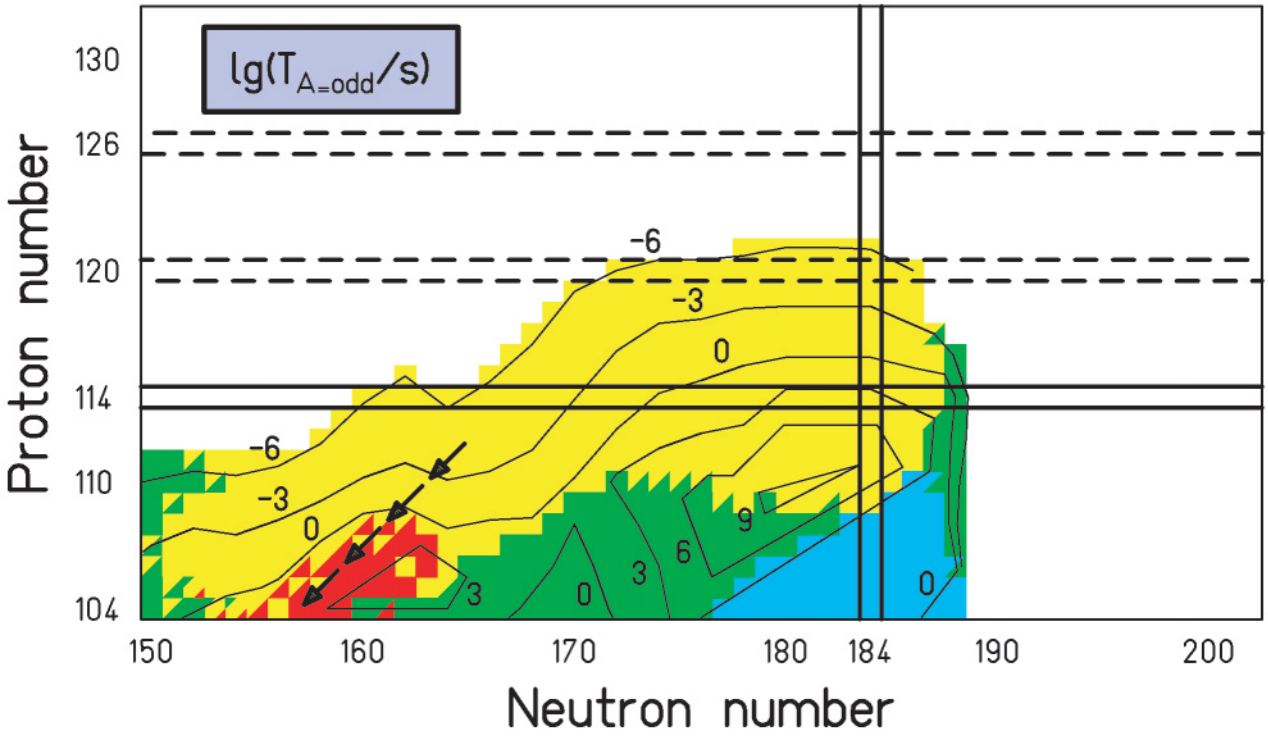

Figure 6 Dominating partial α, β, or fission half-life for odd A-nuclei (28–30). Colors indicate different decay modes, α-decay (yellow), sf-fission (green), β^+-decay (red), and β^--decay (blue). The arrow indicates the decay chain $^{277}112$ (11).

Annual Review of Nuclear and Particle Science
Volume 50, 2000

CONTENTS